PHOTOELECTROCHEMISTRY
OF
GaAs AND Si LIQUID JUNCTIONS

Thesis by
Ming X. Tan

Thesis Advisor
Professor Nathan S. Lewis

In Partial Fulfillment of the Requirements for
the Degree of Doctor of Philosophy

California Institute of Technology
Pasadena, California

1995

(Submitted September 12, 1994)

To My Father and Mother

Acknowledgments

I would like to start by thanking the people who have collaborated with me on the projects presented in this thesis. The GaAs project reported in Chapter 2 was my first research project at Caltech. Amit Kumar, Sharon Lunt, Mike Sailor and Bruce Tufts taught me everything about the experimental techniques and theories involved in the project. Charlotte Newcomb did some of the original GaAs/$Te^{2-/-}$ studies reported in Chapter 2. The real-time photovoltage and quantum-yield measurements presented in Chapter 4 were performed with Chris Kenyon.

I feel lucky to have had the opportunity to work in a very friendly environment during my time at Caltech. First, I would like to thank my advisor, Nate Lewis. I have always felt that I can stop by his office at anytime to discuss scientific problems as well as personal problems, because I know he cares. He not only taught me everything about semiconductor/liquid junctions, and physics of windsurfing, but also the scientific approach to research problems. He pushed me through those days when I was seriously doubting my abilities as a research scientist; he helped me to review all factors regarding the choice between an academic *vs.* industrial career. He fully supported my decision to work in industry and helped me get my "dream job."

Past and present Lewis group members have given me tremendous support in every aspect of my life as a graduate student. Without their help, I would not have survived graduate school. Special thanks to Chris Karp, Janet Kesselman, Colby Stanton, Paul Laibinis, Chris Kenyon, Teri Longin, Gary Shreve, and Ashish Bansal who have helped me with infinite patience to improve my English writing and presentation skills. They have edited every research report, proposal, and paper I have written, and sat through many different versions of my research presentations. I was fortunate to have worked in the lab with Mike Sailor, Bruce Tufts, Sharon Lunt, Chris Wilisch, Paul Laibinis, Chris Kenyon and Chris Karp, with whom I was able to learn experimental techniques and gain scientific insights into the research. Research discussions with them and other Lewis group members, Reggie Penner, Amit Kumar, Gail Ryba, Rik Blumenthal, Iver Lauermann, Xiuling Li, Mike Freund, Ashish Bansal, Chris Claypool, Janet Kesselman, Teri Longin, Sonbinh Nguyen, Kathy Pomykal, Gary Shreve, Marcel Sturzenegger, and Arnel Fajardo, have always been stimulating and helpful. These past and present members of the Lewis group and their families have also introduced me to the many diverse aspects of American culture and strongly influenced my personal life. Our friendships extend outside the Caltech labs, and will last well beyond our times here.

Eight years ago, as a college student in China, it was beyond my wildest dreams to one day have the opportunity to obtain a Ph.D. from one of the finest institutes in the world. I owe everything I have now to my parents, who have worked so hard and sacrificed so much to finally get me and John to this country, and who have supported us throughout our lives. At UC Irvine, John Englund hired me as a stockroom assistant to take care of glassware, even before I learned the English names of beakers and flasks. I had my first "introduction to American culture" from my best friend Tammy. Professor A. J. Shaka introduced me to the world of scientific research, and has encouraged and supported me throughout the years. I wish to thank these people and others for everything they've done for me. Without their help, I would not have come to Caltech.

At Caltech I had the opportunity to meet so many wonderful people, whose friendship, understanding and support have carried me through many tough times. Besides the people mentioned above, I would like to give special thanks to Pat Anderson, Dian Buchness, Hali Forstner, and Christina Dezan.

Finally, I would like to thank Paul Laibinis, Roger Quan, Cathy, Chris, Emily and Karla Wilisch, Maria and Chris Karp for their love and support. I would like to thank LeRoy Whinnery for making this last year of graduate school full of happiness and surprises.

Also, I wish to thank Janet Kesselman, Chris Karp, Chris Kenyon and LeRoy Whinnery for proofreading parts of this thesis.

Thank you, God.

Abstract

A quantitative study has been performed on the stability of GaAs surfaces in a 0.10 M K_2Se-0.01 M K_2Se_2 aqueous solution. In this electrolyte, n-type GaAs electrodes displayed significant photocorrosion in competition with faradaic charge transfer to Se^{2-}. Chemisorption of group VIIIB metal ions onto the GaAs surfaces yielded improved current-voltage behavior of the GaAs photoanodes, and also resulted in a significant reduction in photocorrosion. This behavior implies that the chemisorbed metal ions act to increase the rate of hole transfer to the Se^{2-} species. Related experiments on n-GaAs, p-GaAs, and Sn-doped In_2O_3 electrodes in $Te^{2-/-}$ aqueous solutions have also been performed.

The majority carrier (electrons) transfer rate constant at a highly doped n^+-Si/Co(Cp)$_2$Cl-methanol junction has been measured directly using the chronoamperometry electrochemical technique. The reduction reaction rate of Co(Cp)$_2^+$ was 0.03 cm-s^{-1} at the Si electrode, and was more than 100 times slower than at a hanging mercury electrode. The slower rate was attributed to the smaller optical and static dielectric constants, and the lower density of electrons of the semiconductor. The experimental results were compared to the Marcus theory of charge transfer.

The unique properties of high purity Si/liquid junctions have been investigated under illumination conditions in which the photogenerated carrier concentration exceeds the dopant concentration. Under these high injection conditions, negligible electric fields exist at the semiconductor/liquid interface, and carrier motion is driven by diffusion. Studies of the current-voltage properties of the Si in methanol solutions containing various redox couples suggested that high efficiency photoelectrochemical cells could be established through selective collection of carriers at the semiconductor/liquid junction. The quasi-Fermi levels of electrons and holes were measured directly against the solution potential. Steady-state and transient photovoltage measurements, and theoretical modeling of the carrier transport, generation, and recombination dynamics indicated that the quasi-Fermi levels were flat across the semiconductor sample. The recombination velocities at the Si/liquid junctions have also been measured, and were shown to vary with the solution potential following the Shockley-Read-Hall theory on recombination.

Table of Contents

List of Figures

Chapter 1:

Chapter 2:

Chapter 3:

Chapter 4:

Part I.

Part II

List of Tables

Chapter 2:

Chapter 3:

Chapter 4:

Part I

Part II

Summary

Semiconductor/liquid junction photoelectrochemical cells are a promising method for solar energy conversion. These cells are simple to construct and are effective at converting solar energy into electrical and/or chemical energy, with efficiencies exceeding 15% in state-of-the-art systems. Research presented in this thesis focuses on experimental evaluations of the charge transfer processes at semiconductor/liquid interfaces as a function of semiconductor surface properties and solution chemistry. These fundamental studies are important for the development of stable and high efficiency semiconductor/liquid junction solar cells.

Chapter 1 is a brief introduction to semiconductor/liquid junction photoelectrochemistry. The fundamental processes involved in a solar energy conversion system are addressed. Some basic concepts, such as doping, Fermi-level, depletion, and accumulation, *etc.*, are discussed. In addition, a brief description of the charge transfer processes that occur when a semiconductor is in contact with a solution is presented. Experimental quantities often used to characterize the performance of a semiconductor/liquid junction solar cell are also introduced. The purpose of this chapter is to emphasize the direct correlation between the charge transfer rates of photogenerated carriers at a semiconductor/liquid interface and the energy conversion efficiency of the photoelectrochemical cell.

Chapter 2 presents research on the minority carrier (photogenerated hole) transfer process at an n-GaAs/$Se^{2-/-}$ aqueous solution junction. Under illumination conditions, GaAs can be oxidized in an aqueous solution and subsequently dissolves in the solution. In a diluted $Se^{2-/-}$ aqueous solution, the oxidation reaction of solution Se^{2-} at the semiconductor surface competes with this photocorrosion process. It has been found that chemisorbed group VIII metal ions can modify the GaAs surface and improve the kinetics for the oxidation process. Experiments in this chapter demonstrate that the photocorrosion process can be suppressed as the Se^{2-} oxidation reaction is catalyzed through metal ion chemical modifications of the GaAs electrode. The solar energy conversion efficiency of the photoelectrochemical cell is also improved through this modification. Through these studies of the minority carrier transfer processes, the criteria for constructing high efficiency and stable semiconductor/aqueous solution solar cells are established.

Chapter 3 concentrates on the majority carrier (electrons in an n-doped semiconductor) transfer rate at a semiconductor/liquid junction. The majority carrier transfer process at the semiconductor/liquid interface is unfavorable for the efficiency of the photoelectrochemical cell, and should be minimized. An understanding of the factors that determine this transfer process is important for constructing high efficiency solar cells. This chapter reports the first direct measurement of the electron transfer rate constant at an n-Si/cobaltocenium ($Co(Cp)_2^+$) -methanol junction using the chronoamperometric electrochemical technique. The transfer rate at a mercury electrode was also investigated in the same solution. The rate constant for the reduction of $Co(Cp)_2^+$ at the Si electrode is more than 100 times slower than at the mercury metal electrode. The comparison between these experimental results and theories on the charge transfer processes at semiconductor and metal electrodes has indicated that the intrinsic properties of the semiconductor, such as the static and optical dielectric constant, and the band structure of the semiconductor are responsible for the differences in reaction rates compared to metal electrodes. Experiments in this chapter provide support for further development of theories on majority carrier transfer processes, which are necessary for the rational design of high efficiency semiconductor/liquid junction solar cells.

Chapter 4 explores the charge transfer processes of both the photogenerated electrons and holes under diffusion control. Unlike the conventional semiconductor/liquid junction solar cells that rely on electric field gradients to separate photoexcited carriers, the high purity Si/liquid junctions, reported in this chapter, achieve carrier separation through concentration gradients induced by selective quenching of different types of carriers at opposite sides of the semiconductor. This semiconductor/liquid junction photoelectrochemical cell operates similarly to the photosynthetic system, but >10% energy conversion efficiency and near unity carrier collection yield can be achieved in this cell through the addition of selective chemicals to the solution. This system provides a new alternative for the construction of high efficiency solar cells. The observed junction behavior, as a function of solution redox potential, supports the existing theories on charge transfer at semiconductor/liquid contacts. Our studies provide the first experimental support for an important theoretical construct--the quasi-Fermi level (electrochemical potential of the electrons and holes under non-equilibrium conditions). Quasi-Fermi levels are important for describing the tendency of charge transfer at semiconductor/liquid junctions. The spatial and time dependence of the quasi-Fermi levels in our high purity Si/liquid junctions are demonstrated in this chapter. The experimental validation of the quasi-Fermi level concept is important for a fundamental understanding of the interactions of semiconductor solids and solution.

Chapter 1

Principles of Semiconductor/Liquid Junction Photoelectrochemistry

At present, there are three methods by which light can be converted into industrially useful energy sources. Photosynthesis is nature's method of solar energy conversion, and is ultimately responsible for the chemical fuels that sustain life on this planet. The basic photosynthetic process involves conversion of carbon dioxide and water to sugars and oxygen. In this process, the incident solar radiation provides the energy source, and some of this solar energy is stored in the form of chemical fuels that are produced by the photosynthetic cycle. Typical photosynthetic processes store only 3 to 5% of the total incident power as Gibbs free energy in the fuels of plants during an optimal growing season, yet this level of power storage is sufficient to support life on earth.

Photovoltaic cells are solid state devices that convert solar illumination into electrical energy. Photovoltaic cells have been recognized as a feasible energy conversion technology only within the last 20 years, although devices with efficiencies of 1 to 4% were constructed as early as 1954.[1] A basic photovoltaic cell consists of two different types of solids that are connected at an abrupt, defined junction.[1] This junction provides the cell with the ability to direct electrical current flow in only one direction through the external circuit, and to produce electrical power. In contrast to the process of photosynthesis, photovoltaics cannot directly convert the incident photon energy into chemical fuels, but instead lead only to the production of electricity. Current photovoltaics are quite efficient, and state-of-the-art devices are capable of converting over 25% of the incident solar energy into electrical energy.[2-4] These devices are also extremely durable, and can have lifetimes that exceed 20 years under many types of environmental stresses.[5]

The third type of energy conversion system, which is the topic of this thesis, is a semiconductor/liquid junction photoelectrochemical cell. Photoelectrochemical cells are also relatively recent energy conversion devices. In fact, photoelectrochemical cells with solar energy conversion efficiencies greater than 10% have only been developed within the past 15 years.[6-8] The semiconducting electrode is the key to the operation of a photoelectrochemical cell. The semiconductor is responsible for the absorption of the incident light, while the interface between the semiconductor and the liquid is the key factor in the subsequent chemical steps that lead to energy conversion. Photoelectrochemical cells can be thought of as hybrids between photovoltaics and photosynthesis, in that they can be constructed either to produce electricity or to store chemical fuel, or both. Their solar energy conversion efficiencies are also typically between those of photosynthesis and photovoltaics, with values ranging from less than 1% to as high as 17%.[6]

Photoelectrochemical cells have many advantages over the other types of solar cells.[9-11] They can achieve efficiencies much higher than the photosynthetic systems. The semiconductor/liquid junctions can be formed easily by simple immersion of the semiconductor into a solution, and do not require the complicated fabrication processes used in construction of semiconductor solid junction photovoltaic cells. The semiconductor surface is easily accessible and can be chemically modified. The semiconductor/liquid junction properties can be effected by simply altering the chemicals in the solution. Through chemical control of the solution and the semiconductor surface, some semiconductor/liquid junctions have achieved solar energy conversion efficiencies approaching that of the solid state photovoltaic cells.[12,13]

In almost all potential applications of photoelectrochemical cells, fundamental questions and practical problems still must be addressed before these systems can compete favorably as a practical energy conversion technology. For example, corrosion and passivation processes of the semiconductor electrode often compete with the desired energy conversion reactions.[14-16] These degradation reactions seriously limit the lifetime of most photoelectrochemical devices. In other systems, the recombination of photogenerated carriers at the semiconductor/liquid interface limits the efficiency of the junction.[17,18] The competition between the desired chemical reaction and passivation and recombination processes can be altered, in theory, through chemical control of the semiconductor surface and the solution. A fundamental understanding of the charge transfer processes at the semiconductor/liquid junction is essential for such chemical control.

Fundamental understandings of the solid/liquid interactions are also very important in the development of other technologies. For example, electrochemical etching and corrosion reactions at semiconductor/liquid interfaces are essential processes in integrated circuit technology.[19] Similarly, the expanding field of chemically sensitive semiconductor-based chemical sensors depends on an understanding and control of the properties of the semiconductor/liquid interface.[20,21] One recent application has been the use of large band gap semiconductors as catalysts for a number of useful chemical reactions, for example, the use of suspensions of TiO_2 particles for toxic waste treatment and for novel synthetic oxidations.

In the following sections, some of the fundamental concepts involved in semiconductor/liquid junction photoelectrochemistry are discussed briefly.[22] The purpose of these sections is to introduce the basic operational mechanisms of photoelectrochemical cells and to emphasize the direct correlation between the charge transfer rates at the semiconductor/liquid interface and the performance of the solar cell.

1. Fundamental Processes Involved in a Solar Energy Conversion System:

There are three fundamental processes involved in the successful operation of any solar energy conversion system: excitation of carriers through absorption of light, separation of the photogenerated carriers, and collection of the carriers.

(a). The photogeneration process: To convert solar energy to electrical or chemical fuels, first, the solar cell must be able to absorb sunlight, and generate excited carriers. The minimum energy required for photoexcitation is the energy gap between the ground and excited states of the photo-absorber. In a semiconductor, the ground states and excited states are called the valence band and conduction band respectively (Fig. 1). When photons with energy equal to or greater than the band gap (the energy difference between the top of the valence band and the bottom of the conduction band) are absorbed by the semiconductor, an electron is excited from the valence band into the conduction band, leaving behind a vacancy called a hole.

The semiconductor bandgap is an important parameter to consider when attempting to construct high efficiency solar cells. For example large band gap materials such as TiO_2 will only absorb at short wavelengths, and will not absorb as many photons from sunlight as small band gap semiconductors such as Si. This threshold behavior is one of the main constraints that limits the efficiency of solar energy conversion devices. Since the majority of the solar irradiance is centered in the region between 1 and 3 eV, large band gap semiconductors (*i.e.*, those with $\mathbf{E}_g > 2.2$ eV) will be ineffective at harvesting a substantial fraction of the solar spectrum, and will not provide the most efficient solar energy conversion devices. From this analysis, it would appear that the use of a semiconductor with a small band gap ($\mathbf{E}_g \leq 1$ eV) would be advantageous for solar energy conversion, because such a semiconductor would be able to absorb most of the solar spectrum. Unfortunately, materials with very small band gaps also are not optimal for use in solar energy conversion. In most semiconductors, the absorption of photons with energy $h\nu = \mathbf{E}_g$ leads to an optical transition that produces an electron at the conduction band edge. This excitation energy is then available as the potential energy to drive a chemical reaction. In contrast, absorption of photons with $h\nu > \mathbf{E}_g$ leads to excited states with electron energies greater than the conduction band edge. However, this extra energy is usually wasted, because the highly excited electrons readily thermalize to the energy of the conduction band edge. Thus, regardless of the actual energy of the incident light, a semiconductor with band gap energy $\mathbf{E}_g$ is often only capable of producing excited states with a potential energy $\approx \mathbf{E}_g$ from each absorbed photon. In general, semiconductors with band gap energies that are very small can absorb a large number of photons from the solar spectrum, but will waste a significant amount of that energy as heat, greatly reducing their effectiveness in harvesting the incident solar energy.

The optimal trade-off between effective photon absorption and maximization of the excited state potential energy per absorbed photon can be calculated through a straightforward analysis of the solar spectrum. This analysis leads to the conclusion that materials with band gaps between 1.1 eV and 1.7 eV are the best absorbers for solar energy conversion devices.[7,23-26] Such materials not only can absorb a significant fraction of the solar spectrum, but also can deliver a significant amount of excited state energy from these absorbed photons. It is often thought that in order to drive high energy chemical processes, visible light absorption is the most desirable property of a molecular photocatalyst for solar energy storage. However, an absorption threshold in the near-infrared region is optimal for solar energy conversion applications. Common semiconductor materials with such absorption thresholds include Si, GaAs, InP, $MoSe_2$, and CdTe. Among these materials, the most common semiconductors used in the electronics industry are Si and GaAs. These materials have been the focus of this research.

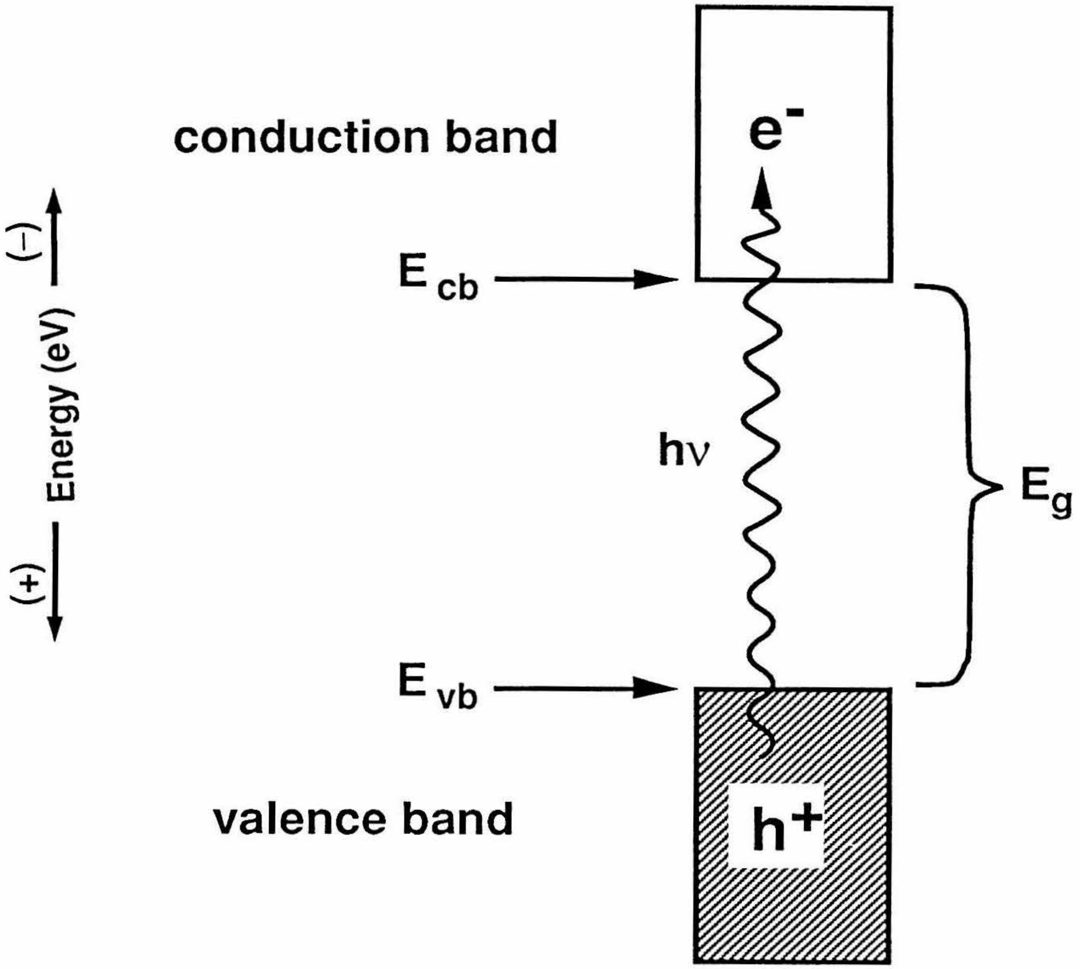

Figure 1. A schematic representation of the orbital band structure of a semiconductor. The shaded area denotes a fully occupied band and the unshaded area denotes an empty band. $\mathbf{E}_{cb}$ and $\mathbf{E}_{vb}$ represent the conduction band edge and the valence band edge, respectively, and $\mathbf{E}_g$ is the band gap. When photons with energy greater than the band gap are absorbed by the semiconductor, electrons (e^-) are excited from the semiconductor valence band into the conduction band. The positive charge (electron vacancy) left in the valence band is called a hole (h^+). It should be noted that the energies of the crystal orbitals are located with respect to the vacuum level as reference. The vacuum level is defined as the energy level of an electron in vacuum, and is taken to be zero eV on the energy scale. Note also that although the physics convention assigns more negative energies to electrons that are more tightly bound relative to vacuum (for example, the energy of a 1s orbital in the H atom is -13.6 eV), the energy scale used by most electrochemists is opposite in sign, with more tightly bound electrons having more positive energies relative to the vacuum level. This assignment on the electrochemical energy scale is based on a "work function" convention, which refers to the energy required to remove an electron from a particular electronic state in the solid. This convention will be used throughout this thesis, and is particularly useful when we relate the energies of bands to those of the solution electrochemical potential scale.

(b). Charge separation process: In any solar energy conversion system, there must be a mechanism to separate the photogenerated electrons and holes, so that they will not recombine and only generate heat. In a typical semiconductor/liquid junction solar cell, this charge separation is established through an electric field gradient at the semiconductor/liquid interface. By a process to be explained later in this chapter, immersion of the semiconductor into a solution produces an electric field at the solid/liquid interface. The charged photogenerated carriers in the semiconductor can sense the electric field present at the solid/liquid interface-being either attracted or repelled by this field-and produce a directional flow of current inside the solid. The energy conversion efficiency of the semiconductor/liquid junction solar cell is directly related to the ability of the electric field to separate the photogenerated charges. Therefore, chemical control over the electric field at a semiconductor/liquid interface is one of the key concerns in the area of semiconductor photoelectrochemistry. An alternative approach in the charge separation process is to use contacts that will selectively remove one type of carrier (similar to the molecular quenching process in the photosynthetic systems), and introduce a diffusion gradient in the solid. This area is the focus of Chapter 4, where a new type of high efficiency solar cell has been developed using diffusion gradients to achieve effective charge separation.

(c). Carrier collection process: The final process in solar energy conversion is the carrier collection process. At a semiconductor/liquid junction, one type of carrier is collected through an external electric wire which passes through an external load (where the electric energy is utilized) and finally reaches the counter metallic electrode in the solution. The other type of carrier reacts with the solution chemical at the semiconductor surface (Fig. 2).

If the reactions at the metallic counter electrode are the reverse of those at the semiconductor electrode, then no net chemical change will take place in the cell. In this mode of operation, the photoinduced current will only result in the production of electrical power in the circuit. For instance, consider the case in which the semiconductor electrode effects the oxidation of water to produce $O_2(g)$. If $O_2(g)$ is simultaneously reduced at the counter electrode, then the only mechanism by which energy can be extracted from this system is by collection of the excess energy from the photogenerated electrons. This can be accomplished by forcing the charges through a resistive load in the external circuit, leading to the net production of electrical energy from the incident light energy. This type of photoelectrochemical cell thus acts similarly to a photovoltaic cell as an energy conversion device. Alternatively, if sufficient energy is available from the electrons, it might be possible to reduce water to $H_2(g)$ at the counter electrode instead of reducing $O_2(g)$. In this system, water is electrolyzed to produce $O_2(g)$ and $H_2(g)$, and fuels will be produced from the incident photon energy. As in the process of photosynthesis, this type of photoelectrochemical cell will have converted the incident solar energy into chemical fuels. If even more energy is available from the electrons, then electrical work through a resistive load and $H_2(g)$ production are possible, and both electricity and chemical fuel would be produced. This latter ability is unique to photoelectrochemical cells.

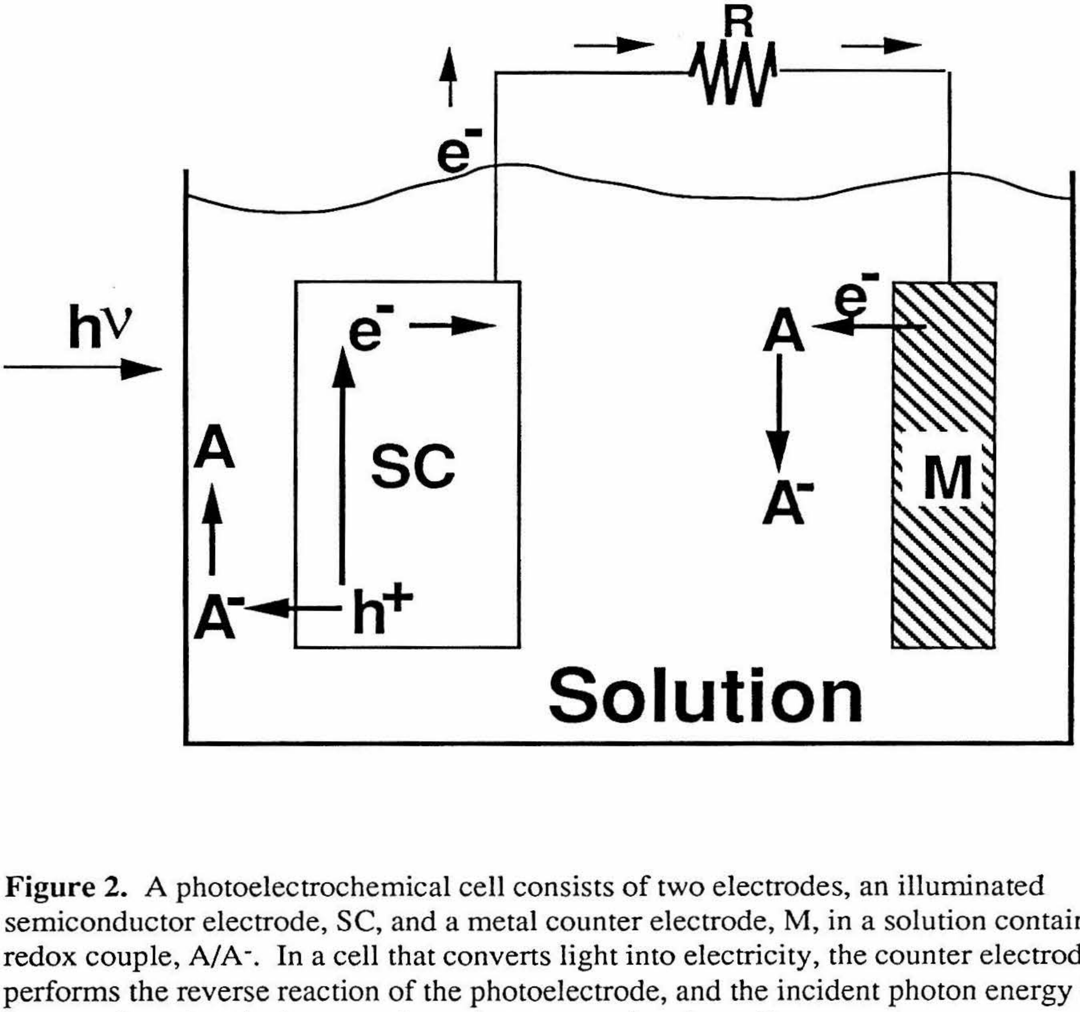

Figure 2. A photoelectrochemical cell consists of two electrodes, an illuminated semiconductor electrode, SC, and a metal counter electrode, M, in a solution containing a redox couple, A/A$^-$. In a cell that converts light into electricity, the counter electrode performs the reverse reaction of the photoelectrode, and the incident photon energy is harvested as electrical energy through an external resistor, R.

2. Charge Separation Through an Electric Field:

We will now examine the charge separation process in more detail, particularly, charge separation through an electric field. First, we must understand the concept of doping, and the definition of the electrochemical potential of the semiconductor.

Because the intrinsic carrier concentrations in semiconductors are so low, even impurity concentrations at the level of 1 part per billion can have a profound effect on the electrical properties of semiconductor samples. To increase the sample conductivity and to control other electronic properties of the semiconductor, low concentrations of specific impurity atoms are often introduced into the crystal lattice. This process is called doping. Dopant atoms can be either donors or acceptors. Donors are readily ionized to produce delocalized electrons in the conduction band and positive charges on the dopant atoms; acceptors become ionized to produce holes in the valence band and negative charges on the dopant site. A material that has been doped with donors is called an n-type semiconductor, while one that has been doped with acceptors is called a p-type semiconductor. These designations can be easily remembered by the sign of the predominant charge carrier. Donors create free electrons, which have a negative charge, so the sample is denoted n-type. Similarly, acceptors create holes, which have a positive charge, so the sample is denoted p-type. The predominant charge carrier is called the majority carrier, so electrons are the majority carriers in an n-type sample and holes are called minority carriers. Similarly, in a p-type semiconductor, holes are the majority carriers and electrons are the minority carriers. Since all the studies mentioned in this thesis involve n-type semiconductors, we will only discuss the n-semiconductor/liquid junction properties in the rest of this chapter.

The doping process changes the distribution of the carriers in the semiconductor energy bands, and moves the Fermi level of the semiconductor. The Fermi level of a semiconductor is the electrochemical potential of the material. As formally defined in statistical mechanics, the Fermi level is the energy level where the probability of finding an electron is 1/2.[26] In an intrinsic semiconductor crystal at absolute zero, the Fermi level would be located at the middle of the band gap. At absolute zero the states in the valence band would be totally occupied. Similarly, at 0 K, the states in the conduction band would be completely empty. The probability of finding an electron therefore would go from 1.0 in the valence band to 0 in the conduction band, and would reach a value of 1/2 at mid-gap (even though there are no actual electronic states at this energy). For a doped semiconductor, the Fermi level position will be shifted from mid-gap, because the doping process will vary the tendency of the solid to either gain or lose electrons. When donors are added to an intrinsic semiconductor, the solid phase will be more likely to lose electrons. The Fermi level of an n-type semiconductor will thus move closer to the conduction band of the semiconductor. The Fermi level position relative to the conduction band edge energy can usually be calculated from Boltzmann statistics, and is determined by the number of electrons in the conduction band, which is a function of the electron donor impurity ions introduced into the n-semiconductor. It is important to realize that the doping process controls the Fermi level position (electrochemical potential) of the semiconductor.

When an n-semiconductor is in contact with a solution, if the electrochemical potential of the semiconductor is above the electrochemical potential of the solution, electrons will flow from the semiconductor into the solution. This transfer of electrons across the solid/liquid junction disrupts the original charge neutrality of the semiconductor and solution. An excess of positive charges is produced in the semiconductor, and an excess of negative charges exists in the solution (Fig. 3). This charging process will continue until the initial difference in electrochemical potentials is neutralized. At this point, the junction will have reached charge transfer equilibrium.

For a doped semiconductor, charge transfer equilibration removes carriers from the sites that are most easily ionized. Thus, if possible, charge is removed from the dopant atoms, as opposed to being removed from atoms of the semiconductor material. For example, for phosphorus doped n-type Si, charge transfer equilibration would be accomplished by the transfer of the fifth valence electron on the phosphorus dopant atoms, as opposed to the transfer of electrons arising from the ionization of the Si lattice atoms. In order to reach charge transfer equilibrium, a certain number of charges must be pulled out of the semiconductor phase. The number of charges that need to be transferred is generally far larger than the number of dopant atoms that are present in one atomic layer of the solid. Thus, the positively charged region extends into the semiconductor. This layer is called the depletion region.

After equilibrium is reached, electric fields and electric potential gradients are present in both the solid and liquid phases, because neither phase is electrically neutral. If the initial electrochemical potential difference between the semiconductor and the solution is large (Fig. 3c), more electrons will transfer from the semiconductor to the solution to establish equilibrium between the two phases. A stronger electric field will establish at the semiconductor/liquid interface. Therefore, one can increase the electric field strength at an n-semiconductor/liquid junction by using solutions with positive redox potentials (moving the electrochemical potential of the solution closer to the valence band of the semiconductor) and/or by increasing the dopant level in the semiconductor (moving the Fermi level of the solid closer to the conduction band of the semiconductor).

Strong electric fields are more effective in separating the photogenerated carriers than weak fields. Under illumination conditions, electrons and holes are generated in the semiconductor bulk and the depletion region. The electric field at the interface will attract positively charged holes toward the semiconductor surface, and repel negatively charged electrons toward the semiconductor bulk (Fig. 3b and d). The holes can then transfer across the semiconductor/liquid interface and oxidize the solution, while electrons can be collected at the back of the sample. When the electric field is weak, some of the electrons can be thermally excited to overcome this field, and also react with the solution at the semiconductor surface. The net number of electrons one can collect in the back of the semiconductor is then reduced, and lower efficiency is expected for the semiconductor/liquid junction. When the electric field is strong, less electrons have the thermal energy available to overcome this field; therefore, higher efficiency is expected.

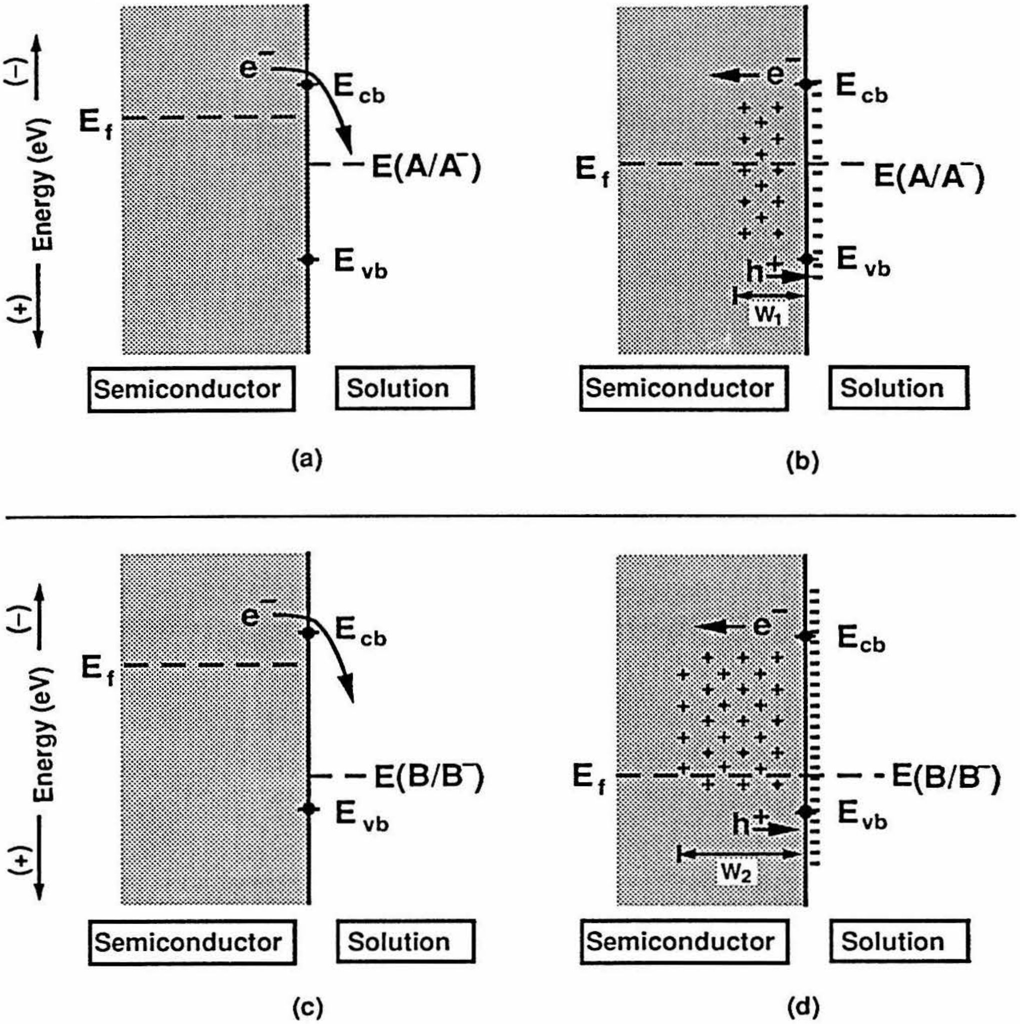

Figure 3. Schematic representations of charge transfer equilibration processes at semiconductor/liquid junctions. (a) Before equilibrium is established, the entire semiconductor is neutral. (b) At equilibrium, a positively charged region (depletion region) of width W_1 is present in the semiconductor. (c) Similar to (a), except that the redox couple (B/B^-) in the solution has a more oxidizing redox potential than A/A^-. (d) Similar to (b), but the depletion region extends deeper into the semiconductor ($W_2 > W_1$), because the number of charges that must cross the semiconductor/liquid interface is greater. In both (b) and (d), the positions of the conduction and valence band edges are unchanged by the charge equilibration processes. When a positive charge (hole) is near the semiconductor/liquid interface, the negative charges on the solution side will attract the charge toward the semiconductor surface. Similarly, when a negative charge is in the depletion region, it will experience the repulsion of all of the negative charges in the liquid phase, while being screened by only a portion of the positive charges in the semiconductor phase. The electric field separates carriers through this mechanism.

We have described above the case when the semiconductor is in depletion. It is also possible, however, that the initial electrochemical potential of the solution will be higher than the Fermi level of the semiconductor (Fig. 4). During the approach to equilibrium, charge will then tend to flow into the semiconductor from the solution phase. However, when electrons from the solution phase are transferred into the semiconductor, these electrons are not confined to dopant atom sites. Instead, the majority carriers (electrons) exist as delocalized charges in the conduction band. The spatial region in the semiconductor where the negative charges accumulate is called the accumulation region. Because these excess majority carriers need not reside on dopant atoms, but can also reside on lattice atoms of the semiconductor, the charge density that can be supported in accumulation is not limited by the dopant density. Instead, it is more closely approximated by the atom density in the crystal lattice. The thickness of an accumulation region is therefore far smaller than that of a depletion region, at least for the same material and same amount of charge transferred across the interface. The width of an accumulation layer is typically less than 100 Å,[27] while the width of a depletion region is usually on the order of micrometers.

Experimentally, the thin width of an accumulation layer implies that charge separation will not be effective for such semiconductor/liquid interfaces. Both electrons and holes can tunnel through the thin electric potential barrier in the accumulation region, so the charge separating ability of the electric field is greatly reduced relative to that in depletion. Additionally, the spatial extent of the electric field gradient in accumulation is reduced relative to the field width in depletion. Only charge carriers created very near to the semiconductor/liquid interface will sense the excess charges in the liquid phase and will be separated by the field when accumulation conditions are established. Semiconductor/liquid interfaces in accumulation are useful for investigating the electrostatics of junction formation, as will be discussed in Chapter 3, but are not useful in the formation of efficient solar energy conversion devices.

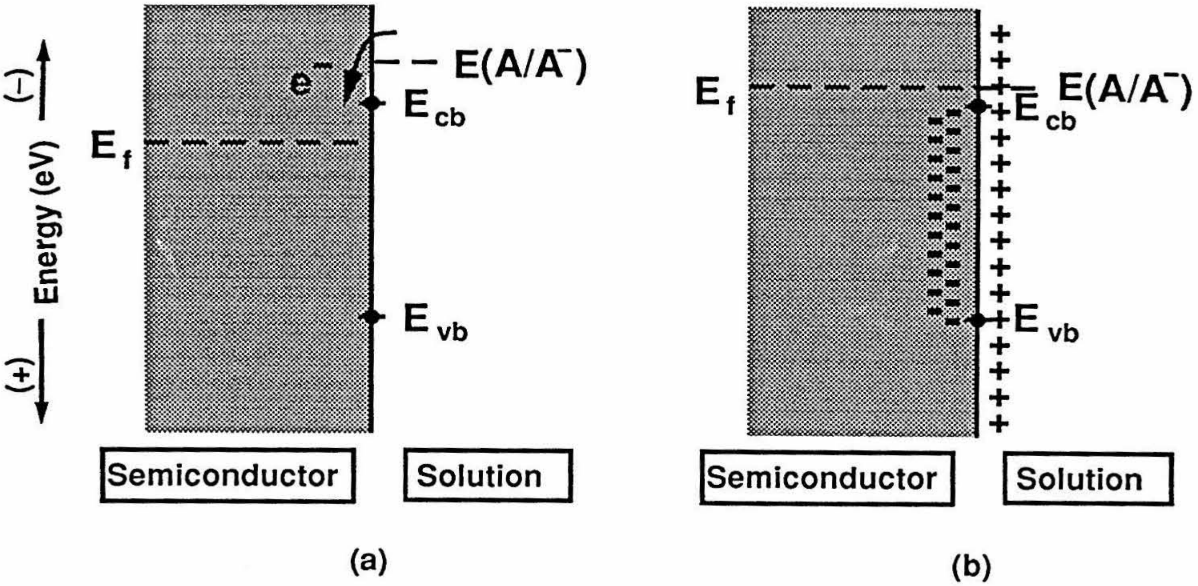

Figure 4. A schematic representation of a semiconductor/liquid junction in accumulation. (a) Before charge equilibration occurs, the electrochemical potential of the semiconductor ($\mathbf{E_f}$) is more positive than the solution electrochemical potential ($E(A/A^-)$), and electrons will flow from the solution into the semiconductor. (b) After charge equilibration has occurred, an accumulation layer containing negative charges is formed in the semiconductor. The negative charges reside near the semiconductor/liquid interface, and the width of the accumulation region is small.

3. The Experimental Quantities Often Used for Semiconductor/Liquid Junction Solar Cells:

In general, there are three quantities that characterize the performance of a photoelectrochemical energy conversion device. These quantities are directly related to the solar energy conversion efficiency of the semiconductor/liquid junction, and provide quick and easy laboratory evaluation of the solar cell performance.

The current through the external circuit represents one such parameter, since no energy can be extracted if no net current is present in the external circuit. The current is generally measured when negligible work is demanded through the measuring device, *i.e.*, when a simple low resistance ammeter is connected between the two electrodes in the cell. This current is called the short-circuit current (I_{sc}) because if measured correctly, it is the current that would flow when a direct short circuit is present between the two electrodes. The short-circuit current reflects the maximum number of carriers one can collect from a semiconductor/liquid junction. When the carrier separation process is efficient, negligible electrons and holes recombine at the semiconductor/liquid interface, and the short-circuit current is the number of photogenerated carriers minus the few carriers that recombine in the semiconductor bulk crystal. Semiconductor/liquid junction systems that collect nearly 100% of the photogenerated carriers have been developed.[28,29] As expected, such systems have very high solar energy conversion efficiencies.

The second parameter of interest is the voltage developed by the photoelectrochemical cell. This voltage is measured at open circuit, with a voltmeter of extremely high resistance, so that negligible current can flow through the cell. The open-circuit voltage (V_{oc}) is a measure of the maximum Gibbs free energy that can be obtained from the cell. Under open-circuit conditions, carriers are not collected in the back of the semiconductor electrode, and electrons and holes recombine at the semiconductor/liquid junction. If this recombination process is slow, *i.e.*, charge separation is effective and electron transfer at the interface is energetically unfavorable, the built-in free-energy through the absorption of light is high, and high V_{oc} values can be measured.

The third parameter characterizes the rate at which the current approaches its limiting short-circuit value, and is called the fill factor (f). This parameter allows the calculation of the maximum power (P_{out}) that can be produced by a given photoelectrochemical cell, $P_{out}=V_{oc}I_{sc}f$. Thus, the solar energy conversion efficiency, which is the ratio of the maximum energy output and the total solar energy input, can be calculated from the V_{oc}, I_{sc} and f measured under a fixed solar irradiation level.

The challenge in this area is to understand how to optimize simultaneously the open-circuit voltage, the short-circuit current, and the fill factor of a given photoelectrochemical cell. Taken together, these three quantities are the key variables that are measured in, and are the focus of, experimental investigations in photoelectrochemistry.

References:

(1) Chapin, D. M.; Fuller, C. S.; Pearson, G. L. *J. Appl. Phys.* **1954**, *25*, 676.

(2) Cuevas, A.; Sinton, R. A.; Midkiff, N. E.; Swanson, R. M. *IEEE Trans. Elect. Devices* **1990**, 6.

(3) Gruenbaum, P. E.; Gan, J. Y.; Swanson, R. M. *Appl. Phys. Lett.* **1991**, *58*, 945.

(4) Li, J. M.; Chong, M.; Zhu, J. C.; Li, Y. J.; Xu, J. D.; Wang, P. D.; Shang, Z. Q.; Yang, Z. K.; Zhu, R. H.; Others *Appl. Phys. Lett.* **1992**, *60*, 2240.

(5) Fahrenbruch, A. L.; Bube, R. H. *Fundamentals of Solar Cells: Photovoltaic Solar Energy Conversion*; Academic: New York, 1983.

(6) Finklea, H. O. *Semiconductor Electrodes*; Elsevier: New York, 1988; Vol. 55.

(7) Heller, A. *Acc. Chem. Res.* **1981**, *14*, 154.

(8) Parkinson, B. *Acc. Chem. Res.* **1984**, *17*, 431.

(9) Wrighton, M. S. *Acc. Chem. Res.* **1979**, *12*, 303.

(10) Fox, M. A. In *Topics in Current Chemistry*; E. Steckhan, Ed.; Springer Verlag: New York, 1987; Vol. 142; pp 72.

(11) Koval, C. A.; Howard, J. N. *Chem. Rev.* **1992**, *92*, 411.

(12) Rosenbluth, M. L.; Lieber, C. M.; Lewis, N. S. *Appl. Phys. Lett.* **1984**, *45*, 423.

(13) Gibbons, J. F.; Cogan, G. W.; Gronet, C. M.; Lewis, N. S. *Appl. Phys. Lett.* **1984**, *45*, 1095.

(14) Gerischer, H.; Gobrecht, J. *Ber. Bunsenges. Phys. Chem.* **1976**, *80*, 327.

(15) Fujishima, A.; Honda, K. *Bull. Chem. Soc. Jpn.* **1971**, *44*, 1148.

(16) Gerischer, H. *Ber. Bunsen-Ges. Phys. Chem.* **1965**, *69*, 578.

(17) Legg, K. D.; Ellis, A. B.; Bolts, J. M.; Wrighton, M. S. *Proc. Natl. Acad. Sci.* **1977**, *74*, 4116.

(18) Bolts, J. M.; Wrighton, M. S. *J. Am. Chem. Soc.* **1978**, *100*, 5257.

(19) Kohl, P. A.; Ostermayer, F. W. *Ann. Rev. Mat. Sci.* **1989**, *19*, 379.

(20) Hafeman, D. G.; Parce, J. W.; McConnell, H. M. *Science* **1988**, *240*, 1182.

(21) de Rooij, N. F.; van de Vlekkert, H. H. In *Chemical Sensor Technology*; N. Yamazoe, Ed.; Kodansha, Ltd.: Tokyo, 1991; Vol. 3; pp 213.

(22) Tan, M. X.; Laibinis, P. E.; Nguyen, S. T.; Kesselman, J. M.; Stanton, C. E.; Lewis, N. S. *Prog. Inorg. Chem.* **1994**, *41*, 21.

(23) Henry, C. H. *J. Appl. Phys.* **1980**, *51*, 4494.

(24) Shockley, W.; Queisser, H. J. *J. Appl. Phys.* **1961**, *32*, 510.

(25) Pierret, R. F. *Semiconductor Fundamentals;* 2nd ed.; Addison-Wesley Publishing Company: Reading, MA, 1988; Vol. 1.

(26) Sze, S. M. *The Physics of Semiconductor Devices;* 2nd ed.; Wiley: New York, 1981.

(27) Morrison, S. R. *Electrochemistry at Semiconductor and Oxidized Metal Electrodes*; Plenum: New York, 1980.

(28) Tufts, B. J.; Abrahams, I. L.; Casagrande, L. G.; Lewis, N. S. *J. Phys. Chem.* **1989**, *93*, 3260.

(29) Rosenbluth, M. L.; Lewis, N. S. *J. Am. Chem. Soc.* **1986**, *108*, 4689.

Chapter 2

Chemical Modification of n-GaAs Photoanodes with Group VIIIB Metal Ions

Abstract: A quantitative study has been performed on the stability of GaAs surfaces to photoanodic corrosion in contact with the 1.0 M KOH(aq)-0.10 M K_2Se(aq)-0.01 M K_2Se_2(aq) electrolyte. In this electrolyte, chemically etched n-type GaAs electrodes displayed significant photocorrosion in competition with faradaic charge transfer to Se^{2-}(aq). Chemisorption of group VIIIB metal ions, including complexes of Co(III), Os(III), and Ru(III), onto the etched GaAs surfaces yielded improved current-voltage behavior of the GaAs photoanodes, and also resulted in a significant reduction in photocorrosion. This behavior implies that the chemisorbed metal ions act to increase the rate of hole transfer to the Se^{2-} donor species, as opposed to the passivation of nonradiative surface recombination. Related experiments on n-GaAs photoanodes in contact with the 1.0 M KOH(aq)-0.3 M Te^{2-}(aq)-0.01 M Te_2^{2-}(aq) electrolyte have also been performed. The current-voltage properties of n-GaAs, p-GaAs, and Sn-doped In_2O_3 electrodes have been investigated in this electrolyte, and these measurements have been used to elucidate common mechanistic features of charge transfer reactions for the Se^{2-}(aq) and Te^{2-}(aq) redox systems.

I. INTRODUCTION

Chemisorption of organic, inorganic, and organometallic reagents onto semiconductor surfaces is a common strategy for manipulating the electrical properties of semiconductor/liquid interfaces. The broad goal of these surface modifications is to improve the current-voltage characteristics of the semiconductor/liquid junctions, and thereby to increase the energy conversion efficiency of these photoelectrochemical cells.[1-5] This strategy has now been used successfully for Si,[6] GaAs,[7] InP,[8] CdSe,[9,10] CdS,[11] CdTe,[12] $CuInS_2$,[13] WSe_2,[14] $PdPS_2$,[15] FeS_2,[16] and other semiconductor photoelectrodes. Recent work in our group has addressed some of the mechanistic issues that pertain to the photoelectrochemistry of III-V semiconductor/liquid interfaces.[17-19] Specifically, n-GaAs photoanodes that have been modified by chemisorption of group VIIIB transition metal ions exhibit improved current-voltage (I-V) properties in contact with an aqueous 1.0 M KOH-0.8 M Se^{2-}-0.1 M Se_2^{2-} electrolyte.[18] The dominant mechanism of this I-V improvement has been proposed to involve either chemical passivation of nonradiative surface recombination sites[1,20] or electrocatalytic acceleration of the minority carrier charge transfer rate into the $Se^{-/2-}(aq)$ redox system.[18,21] Although some experimental evidence supports both points of view, the two mechanisms do predict different I-V behavior under certain experimental conditions. This chapter describes the results of several experiments designed to test these predictions and to distinguish between these two kinetic pathways.

When an n-GaAs/liquid junction is under illumination, the photogenerated electrons and holes are separated by the electric field at the interface. The minority carriers (holes) are swept toward the semiconductor/liquid interface, and can either participate in the faradaic oxidation process (k_p) in the solution, or recombine with the electrons ($k_{p,surf}$) at the interface (Fig. 1a). This recombination process decreases the carrier collection efficiency of the semiconductor/liquid junction, which is proportional to $k_p/(k_p+k_{p,surf})$. In 1978, Heller *et al.* discovered that Ru(III) chemisorbed on GaAs electrodes results in improved fill factors and higher open-circuit voltages (V_{oc}), *i.e.*, the solar energy conversion efficiency at n-GaAs/1M $Se^{-/2-}$/1M KOH junctions is improved.[7] They attributed the improvements in the current-voltage characteristics of the GaAs electrodes to the reduction of nonradiative surface recombination sites (reduction in $k_{p,\,surf}$).

The Heller theory has suggested that chemisorbed metal ions interact with the surface states of GaAs, and split the original surface states into higher and lower energy levels as shown in Fig. 1b. At each of the resulting energy levels, recombination of electrons and holes is less probable than at the original surface-state energy levels, and the reduction in k_s results in an increased carrier collection efficiency. Therefore, the energy conversion efficiency of the semiconductor/liquid junction solar cell is increased.[20] An alternative theory proposed by Allongue *et al.* suggests that the chemisorbed metals catalyze the kinetics of the hole transfer processes, and this increase in k_p leads to a higher conversion efficiency (Fig. 1c).[21]

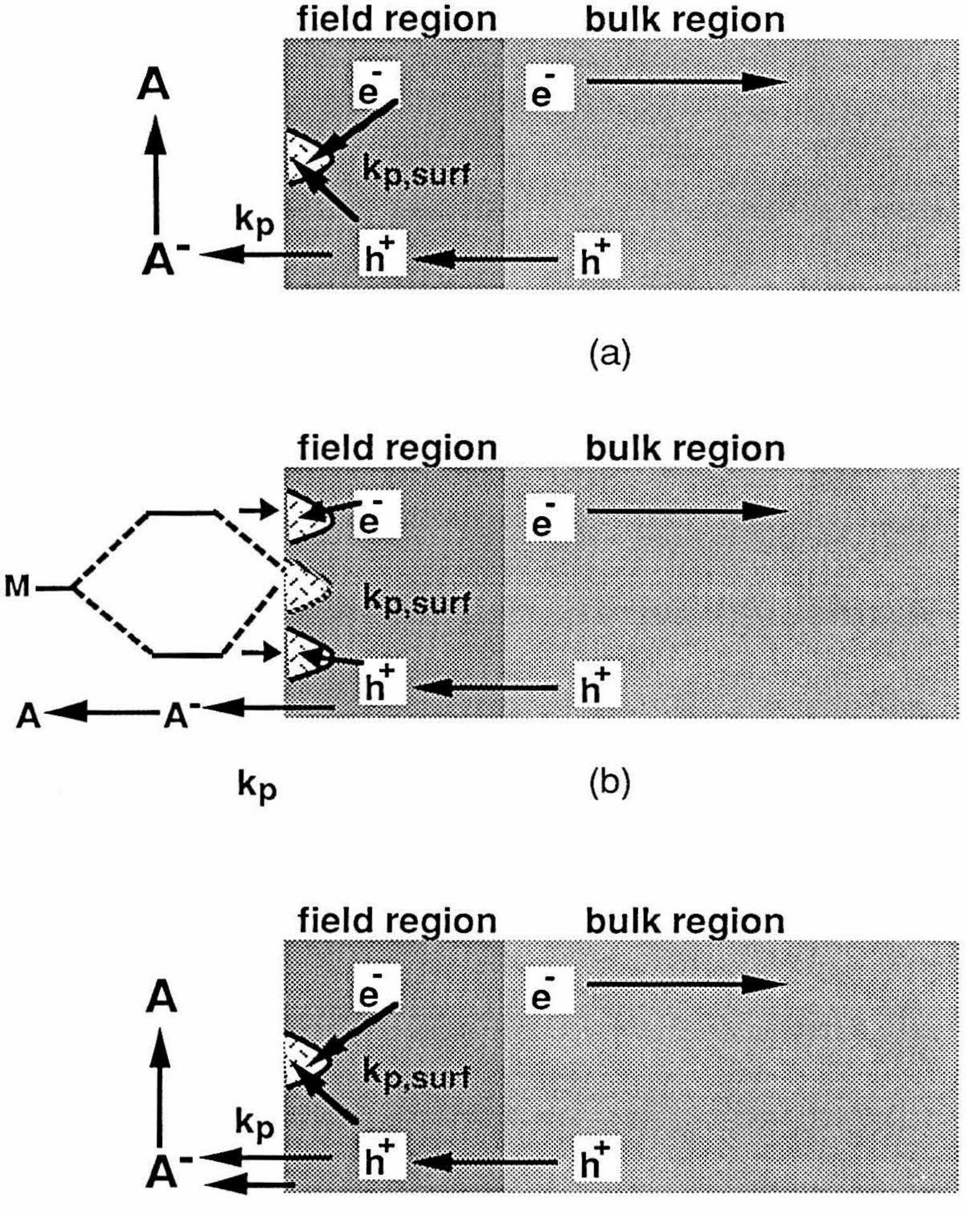

Figure 1. Kinetic pathways for minority carriers (holes) at an n-type semiconductor/liquid interface. Collection of photocurrent by the faradaic electron donor (species A^-) proceeds with a rate constant k_p. k_p has units of cm-s^{-1}, *i.e.*, units of a hole capture velocity, and the resulting hole flux is calculated by multiplying the hole concentration at the semiconductor surface by the hole capture velocity. The hole recombination rate (with a majority carrier) is represented by the rate constant $k_{p.surf}$, *i.e.*, the surface recombination velocity.

We have used quantitative measurements of the kinetic competition between photocorrosion reactions and regenerative redox reactions to evaluate the mechanism of GaAs I-V improvement. At solar light intensities, etched (100)-oriented n-GaAs surfaces are not stable to photocorrosion processes in 1.0 M KOH(aq). A 6-electron decomposition reaction proceeds with 100% faradaic current efficiency to yield soluble Ga(III) and As(III) ions.[22] Earlier measurements of corrosion efficiencies have shown that n-GaAs photoanodes can be stabilized via kinetic competition from suitable redox donors.[23] However, only specific donors, at very high concentrations, can effectively compete with the light-induced corrosion process. For example, stabilization of n-GaAs in 1.0 M KOH(aq) requires high concentrations (≥0.5 M) of Se^{2-}(aq) ions[24] or moderate concentrations (≥0.1 M) of Te^{2-}(aq) ions.[25] At lower concentrations of these ions, photocorrosion partially competes with the desired faradaic charge transfer reaction. We describe below how the presence of the corrosion process can be used for evaluating the mechanism of I-V improvement after surface modification.

In addition to the mechanisms depicted in Fig. 1, in a diluted $Se^{-/2-}$ solution the minority carriers can also participate in a faradaic corrosion reaction (with a hole capture rate k_{corr}) (Fig. 2). The improved I-V properties obtained after chemisorption of metal ions imply a significant decrease in the quantity $\{k_{p,surf}/(k_p+k_{corr})\}$. However, additional information is required to distinguish between an increase in the interfacial faradaic charge transfer velocities (k_p+k_{corr}) and a decrease in the surface recombination velocity, $k_{p,surf}$.

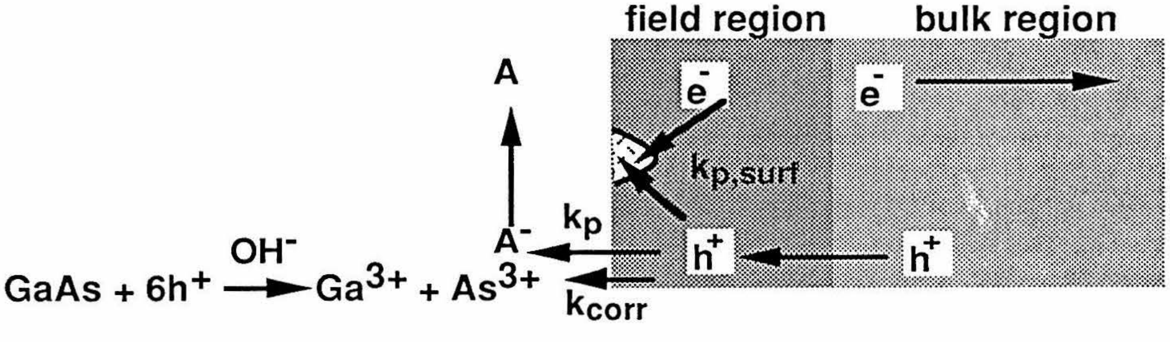

Figure 2. Kinetic pathways for minority carriers (holes) at an n-type semiconductor/liquid interface in a dilute Se^{2-} aqueous solution. An additional kinetic pathway is for the hole to react with the GaAs, with a rate constant (capture velocity) of k_{corr}.

This information can be obtained from a comparison of the corrosion efficiencies before and after the metal ion chemisorption process. Under illumination, stability to photoanodic corrosion is determined by kinetic competition between k_p and k_{corr}, *i.e.*, the ratio k_{corr}/k_p determines the faradaic efficiency for photocorrosion. The documented instability of n-GaAs electrodes with $[Se^{2-}(aq)]<0.5$ M implies that, in dilute $Se^{2-}(aq)$ electrolytes, the rate for photocorrosion competes favorably with the rate for photogenerated hole capture. Thus, if a surface chemical modification process increases the hole capture rate constant, improved photoanode stability would be expected in these electrolytes, due to a decreased value of k_{corr}/k_p.

In contrast, if the chemical modification step primarily effects a reduction in the surface nonradiative recombination rate constant ($k_{p,surf}$), the chemical properties of the remaining minority carriers would not be affected significantly. This prediction is equivalent to the statement that a change in $k_{p,surf}$ should have little or no effect on the ratio (k_{corr}/k_p) at a given photocurrent density. This implies that there should be little or no change in the stability properties of the GaAs anode at a given light intensity and $Se^{-/2-}(aq)$ concentration. Clearly, the two proposed mechanisms of I-V improvement predict qualitatively different photoelectrode stability behavior after chemisorption of metal ions onto the GaAs surface. In this work, we have tested these predictions by performing quantitative stability measurements for etched and metal-ion-treated n-GaAs anodes in 1.0 M KOH(aq)-0.10 M K_2Se(aq)-0.01 M K_2Se_2(aq) solutions.

A related set of kinetic experiments involves the use of a redox system that is not based on KOH-$Se^{-/2-}(aq)$ but is closely related to it. Previous qualitative measurements on n-GaAs photoanodes in contact with the 5 M KOH(aq)-0.10 M $Te^{2-}(aq)$ electrolyte show improved photoanode stability relative to the behavior in contact with the 5 M KOH(aq)-0.10 M $Se^{2-}(aq)$ electrolyte.[25] Given the common corrosion pathway that must be present in both aqueous basic electrolytes, this result implies that the interfacial hole transfer rate in 0.1 M $Te^{2-}(aq)$ is faster than that in 0.1 M $Se^{2-}(aq)$, *i.e.*, $k_{p,Te^{2-}}>k_{p,Se^{2-}}$ at identical illumination intensities for the two junctions. Within the framework of Fig. 2, and with the hypothesis that improvements in I-V properties of etched n-GaAs surfaces in contact with KOH-$X^{-/2-}(aq)$ (X=Se, Te) electrolytes are related primarily to increases in the faradaic charge transfer rate,[18] the stability trends discussed above imply that the I-V properties of etched n-GaAs surfaces in KOH-$Te^{-/2-}(aq)$ should be superior to those in KOH-$Se^{-/2-}(aq)$. Unfortunately, no reliable data are presently available in the literature that would allow a direct comparison between the I-V properties of n-GaAs/KOH-$Se^{-/2-}(aq)$ and n-

GaAs/KOH-$Te^{-/2-}$(aq) junctions under similar conditions of electrode material, redox composition, light intensity, and other pertinent experimental variables. We have therefore collected such data in conjunction with this work.

The kinetic framework of Fig. 2 also allows formulation of another prediction for the I-V behavior of n-GaAs in KOH-$X^{-/2-}$(aq) (X=Se, Te). For similar open-circuit voltages, the observation that $k_{p,\ Te^{2-}} > k_{p,Se^{2-}}$ for the etched GaAs surface predicts that the effects of metal ion chemisorption will be smaller in contact with the KOH-$Te^{-/2-}$(aq) electrolyte than in contact with the KOH-$Se^{-/2-}$(aq) electrolyte. We have investigated these trends in n-GaAs I-V behavior as a part of our experimental study. Experiments with p-GaAs and Sn-doped In_2O_3 electrode surfaces have also proven to be useful in the mechanistic study of metal ion chemisorption at the n-GaAs/KOH-$Se^{-/2-}$(aq) interface,[17-19] so analogous data has been collected for the KOH-$Te^{-/2-}$(aq) system. We have used these results, in conjunction with the other experiments outlined above, to ascertain the common mechanistic pathways for hole transfer at n-GaAs electrodes in contact with $Se^{-/2-}$(aq) and $Te^{-/2-}$(aq) electrolytes.

II. EXPERIMENTAL

The n-GaAs samples used in this work were single crystals obtained from two separate sources. (100)-oriented, n-type, Si-doped GaAs, with a donor density (N_d) of $0.9\text{-}1.9\times10^{17}$ cm^{-3}, a sample thickness of 400-500 μm, and an etch pit density of 8700-7800 cm^{-2}, was purchased from Laser Diode Co. The other sample, purchased from Crystal Specialties Inc., was (100)-oriented n-GaAs with a Si doping level of $1\text{-}2\times10^{17}$ cm^{-3}, an etch pit density <3000 cm^{-2}, and a thickness of 640 μm. The crystals were scribed into rectangular pieces of typical edge dimension 4-6 mm to be used as electrodes. The p-GaAs samples were (100) oriented, Zn-doped epilayers (10 μm thick) with an acceptor density of 2×10^{17} cm^{-3}. Sn-doped In_2O_3 electrodes (10% Sn) were thin films (1.2×10^3 Å) deposited onto glass slides.

Specific procedures used for mounting electrode samples, modifying electrodes, and electrochemical experiments followed the procedures described previously.[18,26] The aqueous 1.0 M KOH-0.10 M Se^{2-} -0.01 M Se_2^{-2} electrolyte was obtained from dilution (with 1.0 M KOH(aq)) of a 1.0 M KOH-0.8 M Se^{2-}(aq) electrolyte that had been prepared as described by Tufts *et al.*[18] $Te^{-/2-}$(aq) solutions were prepared by reduction of a tellurium (Te) cathode in a two compartment electrochemical cell that was continuously purged with N_2(g). A rod of Te metal was the working electrode, carbon cloth was the counter electrode, 1.0 M KOH(aq) was the electrolyte, and the two compartments were separated by a Nafion cation exchange membrane. Current was passed until the desired amount of Te cathodically dissolved into the electrolyte solution; further reduction at a Pt electrode was then used to adjust the relative concentrations of the Te^-(aq) and Te^{2-}(aq) redox states. The final concentration of total dissolved Te was determined by exposing a 10 ml aliquot of the KOH-$Te^{-/2-}$(aq) solution to ambient air; this oxidized the dissolved Te anions to Te metal, which was then weighed on an analytical balance. Typical solution compositions were 1.0 M KOH(aq)-(0.33±0.03) M Te^{2-}(aq)-0.01 M Te_2^{2-}(aq). For brevity, these solutions have been referred to below as 1.0 M KOH(aq)-0.3 M Te^{2-}(aq)-0.01 M Te_2^{2-}(aq) solutions.

A single compartment cell containing the Pt reference and auxiliary electrodes together with 5-15 ml of electrolyte was used for electrochemical experiments. As in previous work with KOH-$Se^{-/2-}$(aq) solutions,[18] extreme care was taken to avoid contamination of the electrolyte with transition metal ions. Solutions of 0.010 M $RuCl_3$ (pH=2.0), 0.010 M $OsCl_3$ (pH=2.0), 0.010 M K_2OsCl_6 (pH=2.0), or 0.010 M $Co(NH_3)_6Cl_3$ (pH=12.0) were used as the sources for chemisorbed metal ions. Each electrochemical cell was only used for one type of metal ion, and separate electrode sets were used for each electrochemical cell. When the I-V curves of etched n-GaAs electrodes in contact with KOH-$Se^{-/2-}$(aq) deviated significantly from the behavior reported by Tufts *et al.*,[18] the electrolyte solutions were discarded and the electrochemical cells were thoroughly cleaned before use in any subsequent experiments.

Stability runs were conducted under potentiostatic control of the GaAs photoelectrode. The reduction potentials of typical aqueous electrolytes were as follows: 1.0 M KOH-0.8 M Se^{2-}-0.1 M Se_2^{2-}, E_{cell}= -0.99 V; 1.0 M KOH-0.10 M Se^{2-}-0.01 M Se_2^{2-}, E_{cell}= -0.96 V, with potentials quoted with respect to a saturated calomel electrode (SCE). In a stability run, the illuminated n-GaAs electrode was cycled (at 50 mV-s^{-1}) between -0.800 V and 0.000 V *vs.* the KOH-$Se^{-/2-}$(aq) potential until a stable I-V curve was obtained; the working electrode potential was then held at short-circuit with respect to the solution potential, and the desired amount of charge was passed. A tungsten-halogen ELH-type bulb[18] provided the electrode illumination, with the light intensity adjusted to maintain short-circuit photocurrent densities of 18-22 mA-cm^{-2} during the corrosion studies.

In some stability experiments, only the central portion of the electrode area was exposed to illumination. To limit the illuminated area, the electrochemical cell was covered by black electrical tape until only a small rectangle remained unmasked. The pinhole typically had an area of 7 mm^2. The position of the unmasked region was carefully adjusted so that the illumination struck the center of the electrode surface.

GaAs electrodes were etched following the recommendations of Stocker and Aspnes.[27] Samples were etched sequentially in 0.05% Br_2-CH_3OH and 1.0 M KOH(aq) solutions, with each etch being 10 sec in duration. Before further use of the GaAs, this etching procedure was performed three times on each sample. After the final KOH etch, the sample was rinsed with deionized water and then dried under a stream of N_2(g). This etch leaves a surface with minimal oxides and elemental As,[27,28] and was used in this study unless otherwise noted.

Soluble Ga and As ions produced by photocorrosion of the GaAs crystal were detected using direct current plasma (DCP) atomic emission spectral analysis. For calibration purposes, Ga and As atomic absorption standard solutions (Aldrich Chemical Co.) were diluted in 1.0 M KOH(aq)-0.10 M Se^{2-}(aq)-0.01 M Se_2^{2-}(aq) solutions to produce a series of Ga or As concentrations between 1.1×10^{-5} and 8.6×10^{-4} M. For corrosion studies, after a controlled amount of current had been passed, the entire 1.0 M KOH(aq)-0.10 M Se^{2-}(aq)-0.01 M Se_2^{2-}(aq) electrolyte, of a typical volume of 5-15 ml, was removed from the electrolysis cell. Before analysis, a stream of O_2(g) was passed through both the calibration and unknown solutions in order to oxidize any Se^-(aq) or Se^{2-}(aq) to Se metal. The Se precipitate was then removed by filtration, and the resulting air-stable solutions were subjected to DCP analysis. Both the Ga and As DCP signals displayed excellent linearity as a function of the Ga or As solution concentrations; the DCP calibration curves obtained from these standard solutions were then used to determine the Ga and As concentrations in all other solutions of interest. When GaAs electrodes provided the source of the Ga and As, photocorrosion percentages were obtained by assuming a stoichiometry of 6 electron equivalents per equivalent of dissolved As or Ga.[22]

III. RESULTS

1. I-V Behavior of n-GaAs Photoanodes in Contact with Aqueous 1.0 M KOH-0.10 M Se^{2-}-0.01 M Se_2^{2-} Solutions:

Figure 3a displays a typical current-voltage curve observed for n-GaAs anodes in 1.0 M KOH(aq)-0.10 M Se^{2-}(aq)-0.01 M Se_2^{2-}(aq). The I-V curve displays a low fill factor, substantial hysteresis, and a pronounced inflection point. All of these features are in accord with the I-V properties reported previously for n-GaAs anodes in contact with the more concentrated 1.0M KOH(aq)-0.8 M Se^{2-}(aq)-0.1 M Se_2^{2-}(aq) electrolyte.[17-20] However, the I-V properties in the more dilute 1.0 M KOH(aq)-0.10 M Se^{2-}(aq)-0.01 M Se_2^{2-}(aq) medium represent a combination of Se^{2-}(aq) oxidation and photoanodic dissolution processes. The I-V properties in this dilute electrolyte also vary somewhat with time, with the behavior after passage of 82 C-cm^{-2} of anodic charge displayed as the dashed line in Fig. 3a. The data in Fig. 3a serve as the baseline for evaluation of the effects of metal ion chemisorption.

Figures 3b-d display the typical I-V characteristics for n-GaAs anodes after exposure to solutions of group VIIIB transition metal ions. Chemisorption of these metal ions has been shown previously to yield improved n-GaAs I-V properties in aqueous 1.0 M KOH-0.8 M Se^{2-}-0.1 M Se_2^{2-} solutions,[17-20] and similar behavior was observed in the more dilute 1.0 M KOH-0.10 M Se^{2-}-0.01 M Se_2^{2-} aqueous solution. The I-V properties for metal-ion treated GaAs samples exhibits less hysteresis, improved fill factors, and improved stability relative to the behavior of etched GaAs photoanodes. As displayed in Figs. 3b-d, only small changes in the I-V properties are observed after passage of >80 C-cm^{-2} of anodic charge, and the I-V curves after such sustained cell operation are still far superior to those obtained with etched GaAs surfaces.

Of note is that the electrolyte solutions used in these experiments contained no deliberately added metal ions; furthermore, thorough etching of the electrode always restored the I-V curve of Fig. 3a regardless of the previous history of the GaAs surface. The persistent improvement of the I-V properties for such large amounts of anodic charge, even though the initial coverage of chemisorbed metal ions were in the range 10^{14}-10^{16} atoms-cm^{-2} (0.1-10 monolayers),[29] strongly suggests that photocorrosion processes have been reduced substantially in the dilute 1.0 M KOH(aq)-0.10 M Se^{2-}(aq)-0.01 M Se_2^{2-}(aq) electrolyte.

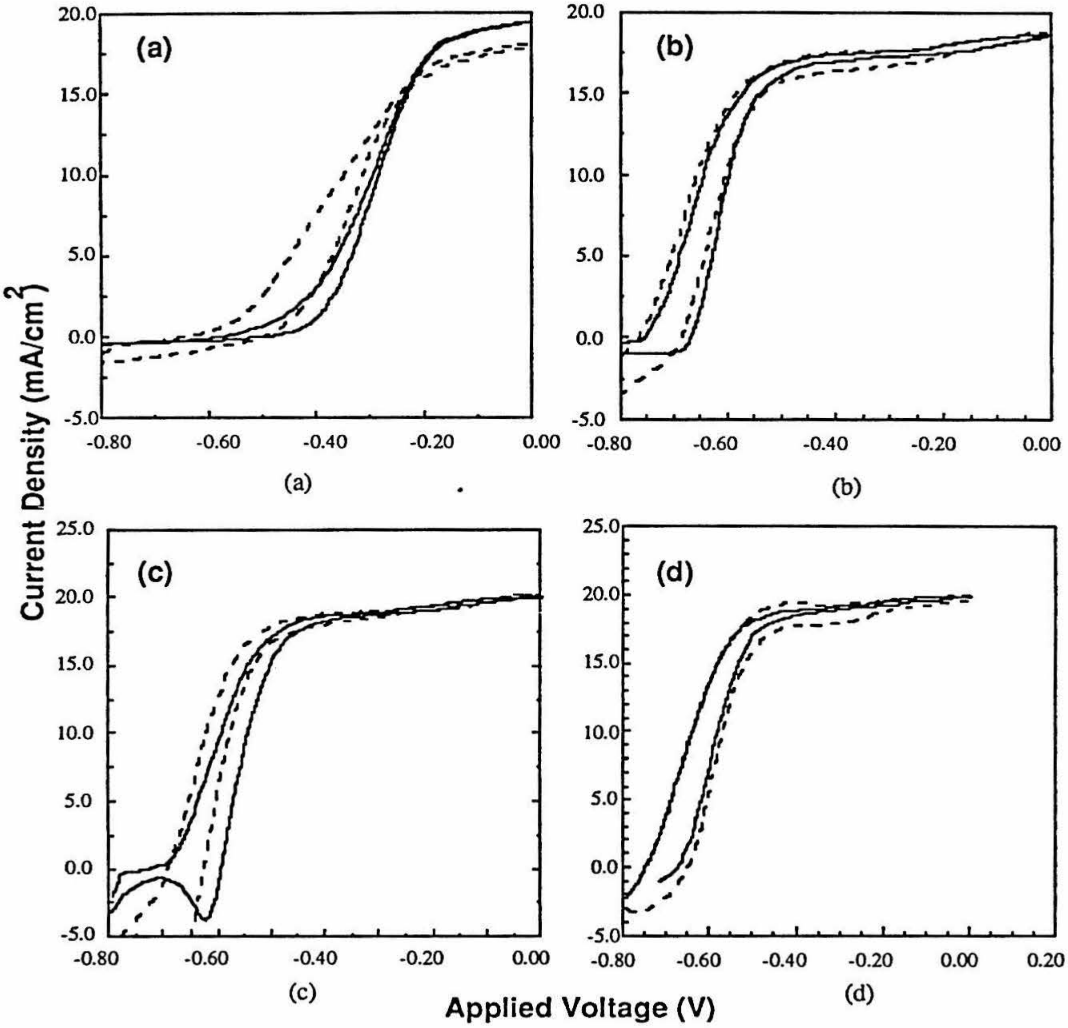

Figure 3. Photocurrent-voltage behavior (at a 50 mV-s^{-1} scan rate) of n-GaAs(100) anodes in aqueous 1.0 M KOH-0.10 M Se^{2-}-0.01 M Se$_2^{2-}$. (a) Etched surface; (b) Ru(III) treated surface; (c) Co(III) treated surface; (d) Os(III) treated surface. In each panel, the solid line (——) depicts the I-V properties of the electrode after passage of <8 C-cm^{-2} of anodic charge. The dashed line (- - - -) depicts the I-V properties after passage of >80 C-cm^{-2} of anodic charge through the electrode. The I-V properties in Figs. 3a-d were collected under experimental conditions described in entries A-D of Table I.

The net faradaic efficiency for photocorrosion was found to be a function of the ratio of the illuminated area to the total exposed area of the GaAs electrode. Figure 4 displays the I-V behavior of GaAs samples that were only illuminated in the central portion of the exposed electrode area. The general I-V behavior of these samples was in accord with those described above (Fig. 3a-d), except that no significant degradation in I-V properties was evident during sustained photoelectrochemical operation in 1.0 M KOH(aq)-0.10 M Se^{2-}(aq)-0.01 M Se_2^{2-}(aq).

The somewhat lower open-circuit voltages displayed in Fig. 4a-d are expected because, although the photocurrent density in the illuminated area was held constant for all samples in Figs. 3 and 4, the total illuminated area was lower for the partially masked GaAs specimens of Fig. 4. This condition results in a larger ratio of dark recombination current to total photocurrent for the partially illuminated samples, which is expected to produce a lower open-circuit voltage.[30-32] However, these smaller voltage values do not, in themselves, indicate any change in the intrinsic photovoltage behavior of the central portion of the solid/liquid junction relative to that observed when the entire GaAs surface is illuminated.

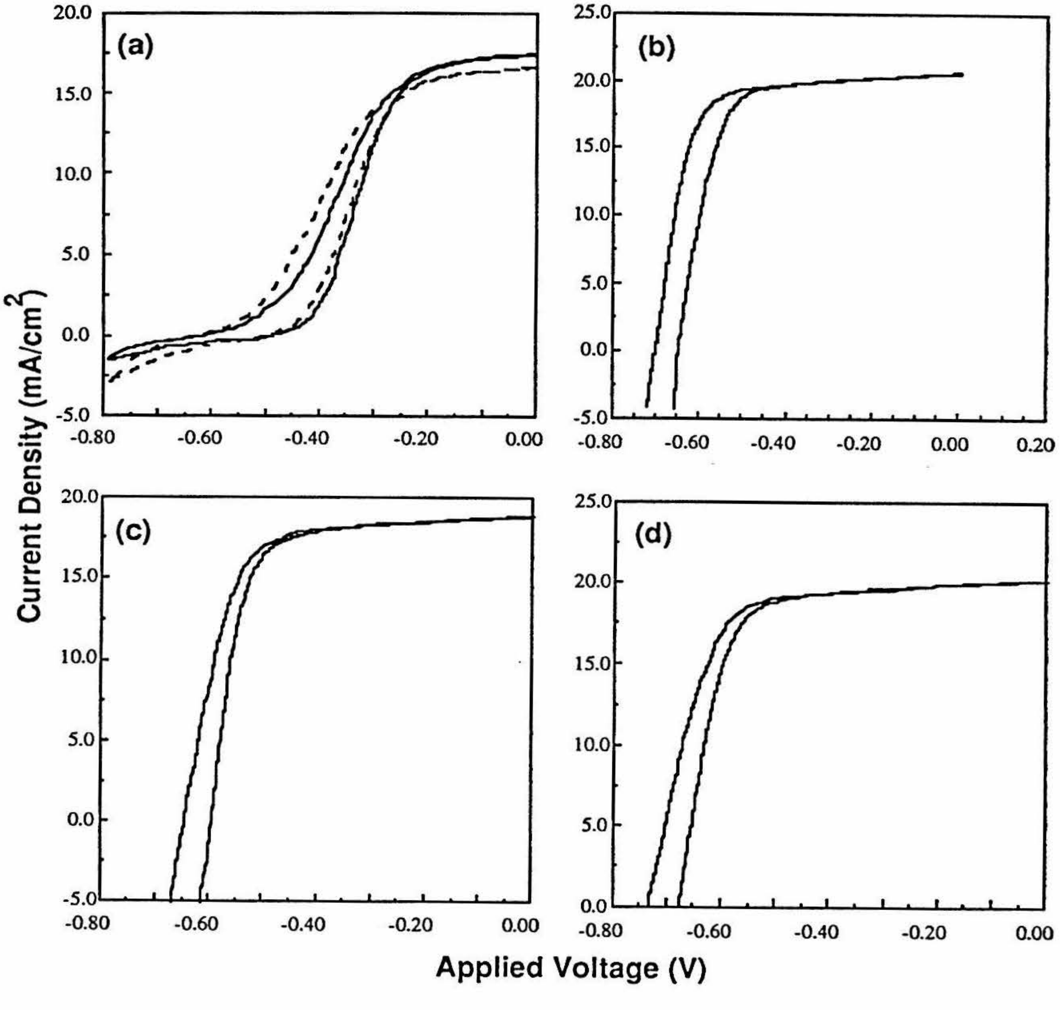

Figure 4. Photocurrent-voltage behavior of n-GaAs(100) anodes in aqueous 1.0 M KOH-0.10 M Se^{2-}-0.01 M Se_2^{2-}. For these data, only the central portion of the electrode was illuminated; the current densities on the ordinate refer only to the illuminated portion of the electrode surface. (a) Etched GaAs surface; the dashed line (----) depicts the I-V properties after passage of >500 C-cm^{-2} of anodic charge through the electrode. (b) $RuCl_3$ treated surface; (c) $[Co(NH_3)_6]Cl_3$ treated surface; (d) K_2OsCl_6 treated surface. Note the lack of time dependence of the I-V properties in panels b-d, in contrast to the behavior of the fully illuminated electrode surfaces of Figs. 4b-d. The I-V properties in Figs. 4a-d were collected under experimental conditions described in entries E-H of Table I.

2. *Stability of n-GaAs Photoanodes in Aqueous 1.0 M KOH-0.10 M* Se^{2-}*-0.01 M* Se_2^{2-} *Solutions:*

Although the I-V behavior qualitatively indicates that metal ion chemisorption reduces the rate of GaAs photocorrosion, quantitative information on the GaAs dissolution rates requires a direct determination of the photocorrosion products released into the solution. DCP atomic emission spectrum analysis was found to be an extremely sensitive method for the quantitative detection of dissolved Ga and As, and this technique was used to obtain the results described below.

Table I summarizes measurements of the dissolved Ga and As found by the DCP analysis. Measurements were performed on a variety of GaAs crystals of different exposed areas, and the ratio of the illuminated area to the total area exposed to solution was also varied. Although n-GaAs anodes that had been exposed to the various transition metal ions showed a significant reduction in photocorrosion efficiency relative to the etched GaAs/1.0 M KOH(aq)-0.1 M Se^{2-}(aq)-0.01 M Se_2^{2-}(aq) junction, substantial amounts of dissolved Ga and As were still observed in the electrolyte solution (Table I). This occurred despite the persistence of the improved I-V properties shown in Fig. 3b-d.

To address this apparent contradiction, another series of corrosion measurements was performed on nominally identical GaAs samples, but only the central portion of the electrode surface was exposed to illumination during the photoelectrolysis. The data for this set of experiments yields a somewhat lower photocorrosion efficiency for the etched GaAs surfaces (Table I). The important result is that, in this masked configuration, no dissolved Ga or As was detected by DCP for the various metal-ion-treated GaAs electrodes. This seems to indicate that the illuminated edge regions of GaAs electrode surfaces have higher photocorrosion rates than the central portion of the electrode, and that the dissolved Ga and As, detected from uniformly illuminated GaAs samples exposed to metal ion solutions, originate from enhanced reactivity in the edge regions near the electrode/epoxy boundaries. The data of Table I imply that elimination of this experimental complication is required to obtain true photocorrosion efficiencies for the various n-GaAs/KOH-$Se^{-/2-}$(aq) interfaces.

Photocorrosion of the illuminated portion of etched GaAs samples is readily confirmed by visual inspection of the electrode, because a distinct topographic depression in the surface, due to sustained GaAs dissolution, can be observed in regions where the electrode had been illuminated. In contrast, such features are not evident after etching and exposure of the GaAs to the various group VIIIB metal ions. An example of this situation is presented in the optical photographs of Fig. 5. These photographs are representative of etched GaAs *vs*. etched and K_2OsCl_6 treated (0.010 M K_2OsCl_6, pH = 2.0) n-GaAs samples that had been exposed to 1.0 M KOH(aq)-0.10 M Se^{2-}(aq)-0.01 M Se_2^{2-}(aq) under otherwise identical experimental conditions. These visual observations confirm the DCP results obtained with these photoanodes, and underscore the role of edge regions in dominating the corrosion reactions of metal-ion-treated GaAs samples.

Table I. GaAs photocorrosion in 1.0 M KOH(aq)-0.10 M Se^{2-}(aq)-0.01 M Se_2^{2-}(aq) electrolyte measured by direct current plasma atomic emission spectral analysis.

Experiment	Sample	Total Dimension[a] [mm x mm]	Illuminated Dimension[a] [mm x mm]	Coulombs Passed (C)[b]	(C-cm^{-2})	Ga or As[c] Detected(μmol)	Corrosion%[d]
A	0.05% Br_2/CH_3OH	3.3 x 6.1	3.3 x 6.1	15.97	79.3	1.97 ± 0.20	6.4 - 7.9
	etched GaAs	3.4 x 5.0	3.4 x 5.0	15.97	93.9	2.29 ± 0.23	7.4 - 9.2
		2.5 x 6.0	2.5 x 6.0	15.97	106.5	2.30 ± 0.23	7.5 - 9.2[e]
							Average: 7.9
B	GaAs 60s in	3.1 x 5.1	3.1 x 5.1	15.93	99.6	0.61 ± 0.06	2.0 - 2.5
	0.01 M $RuCl_3$	3.4 x 5.1	3.4 x 5.1	16.07	94.5	0.82 ± 0.08	2.6 - 3.2[e]
	(pH = 2.0)						Average: 2.6
C	GaAs 60s in 0.01M	3.0 x 5.7	3.0 x 5.7	16.40	96.5	0.50 ± 0.05	1.6 - 2.0
	$[Co(NH_3)_6]Cl_3$	3.1 x 6.1	3.1 x 6.1	15.94	83.9	0.71 ± 0.07	2.3 - 2.9
	(pH = 12.0)	3.1 x 5.4	3.1 x 5.4	16.11	94.8	0.78 ± 0.08	2.5 - 3.1[e]
							Average: 2.4
D	GaAs 60s in	2.6 x 6.2	2.6 x 6.2	15.90	99.4	0.71 ± 0.07	2.3 - 2.9
	0.01 M $OsCl_3$	3.0 x 5.7	3.0 x 5.7	16.04	100.3	0.58 ± 0.06	1.9 - 2.3
	(pH = 2.0)	3.0 x 5.7	3.0 x 5.7	15.05	88.5	0.63 ± 0.06	2.2 - 2.7
							Average: 2.4
E	0.05% Br_2/CH_3OH	4.0 x 11.8	1.0 x 5.8	30.15	502.5	1.44 ± 0.14	2.5 - 3.1
	etched GaAs	3.0 x 9.5	1.1 x 7.9	57.89	643.2	3.12 ± 0.31	2.8 - 3.4
							Average: 3.0
F	GaAs 60s in 0.01 M $RuCl_3$ (pH = 2.0)	5.0 x 8.0	1.3 x 6.5	42.27	469.7	<0.15[f]	<0.1%[g]
G	GaAs 60s in 0.01M	5.3 x 13.0	2.2 x 8.7	60.97	338.7	<0.15[f]	<0.1%[g]
	$Co(NH_3)_6Cl_3$ (pH = 12.0)	5.0 x 8.5	2.0 x 5.0	61.44	614.4	<0.16[f]	<0.1%[g]
H	GaAs 60s in 0.01 M K_2OsCl_6 (pH = 2.0)	3.5 x 8.0	0.9 x 4.6	33.57	839.3	<0.15[f]	<0.1%[g]
I	0.05% Br_2/CH_3OH etched GaAs	3.0 x 6.0	dark[h]	0	0	<0.05[f]	------
J	0.05% Br_2/CH_3OH etched GaAs	3.0 x 6.0	3.0 x 6.0	0	0[i]	<0.05[f]	------

(a) In all experiments, the electrode was maintained under potentiostatic control at the solution potential of the 1.0 M KOH(aq)-0.10 M Se^{2-}(aq)-0.01 M Se_2^{2-}(aq) electrolyte; the light intensity was adjusted to obtain short-circuit photocurrent densities of 18-22 mA-cm^{-2}. Electrode areas were accurately determined from photographs of the electrode surface; the approximate dimensions of the total exposed electrode area and of the illuminated electrode area are also listed. (b) Total anodic charge passed through each GaAs electrode, as measured with a PAR Model 179 digital coulometer. (c) Since the Ga and As concentrations detected by DCP were in a 1:1 ratio, only one element's concentration is reported in the Table. A conservative value of 10% relative error in the Ga or As concentration was used in the error analysis. (d) corrosion %= [(moles of Ga or As detected) x (Faraday's constant) x (6 electrons/equivalent Ga or As) x (100)] / (total coulombs passed). (e) This GaAs sample had an etch pit density <3000 cm^{-2}, while all other samples had etch pit densities of 8000 cm^{-2}. No significant differences in photocorrosion efficiency were observed between these two types of specimens. (f) The concentration of Ga or As was below the DCP detection limit ($1x10^{-5}$ M); the upper limit on the moles of Ga or As in the electrolyte is quoted in the entry. (g) Since the concentrations of Ga and As were below the detection limit of DCP analysis, only upper limits for corrosion percentages have been listed. (h) The electrode was held at -100 mV *vs.* the solution cell potential in the dark for >2 hours. (i) The electrode was left at open-circuit under illumination for >1.5 hours.

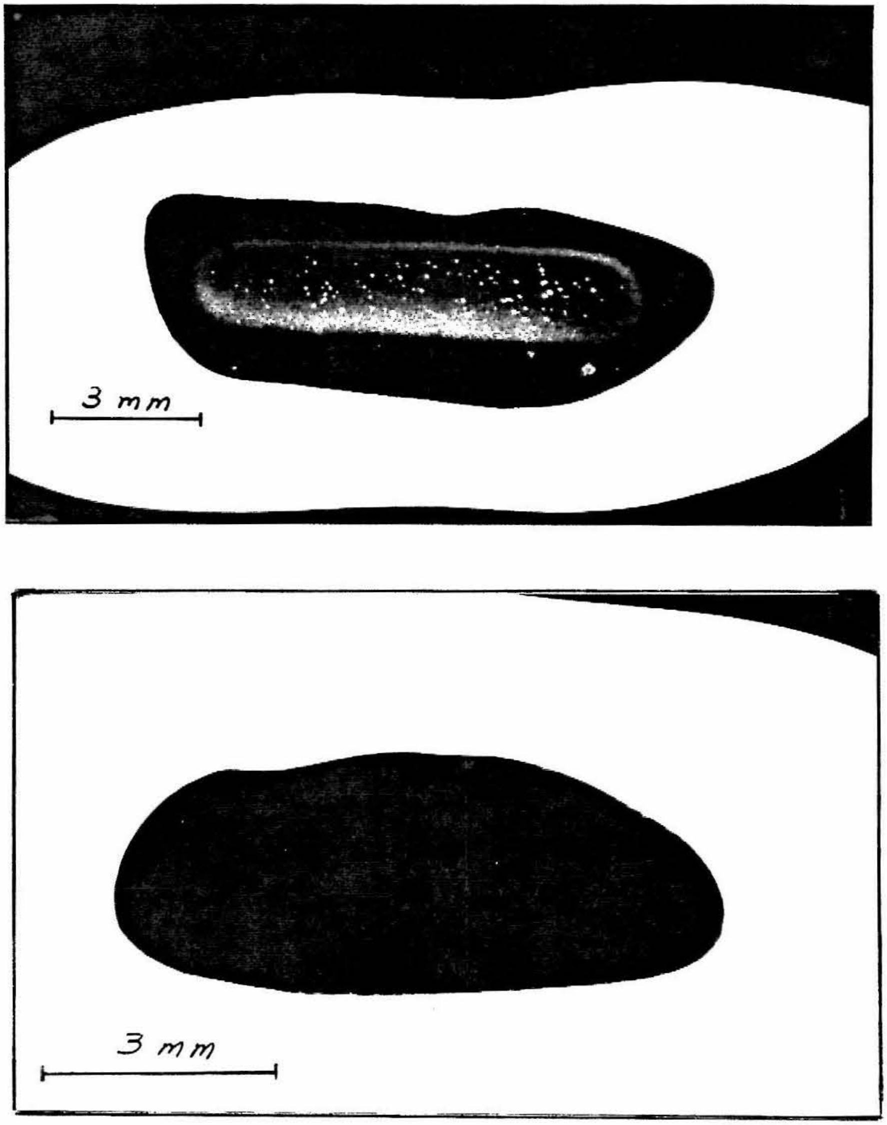

Figure 5. Optical photographs of two n-GaAs anodes that had been immersed into the 1.0 M KOH-0.10 M Se^{2-}-0.01 M Se_2^{2-}(aq) electrolyte. The electrode in the top picture was etched before use, and was subjected to passage of 643 C-cm^{-2} of anodic charge under the experimental conditions of entry E in Table I; the electrode in the bottom picture was etched and exposed to 0.010 M K_2OsCl_6(aq) at pH=2.0 before contact with the $Se^{-/2-}$ electrolyte, and was subjected to passage of 839 C-cm^{-2} of anodic charge, as described in entry H of Table I. The suppression of corrosion by Os chemisorption is obvious from the photograph.

3. *I-V Data for n-GaAs Anodes in Aqueous 1.0 M KOH-0.3 M Te^{2-} Solutions:*

Figure 6 displays the I-V behavior of n-GaAs samples in aqueous 1.0 M KOH-0.3 M Te^{2-}-0.01 M Te$_2^{2-}$. These data were collected under conditions that allowed direct comparison with earlier measurements on n-GaAs/1.0 M KOH(aq)-0.8 M Se^{2-}(aq)-0.1 M Se$_2^{2-}$(aq) interfaces.[18] At all photocurrent densities, the fill factors for the n-GaAs/1.0 M KOH-0.3 M Te^{2-}-0.01 M Te$_2^{2-}$ (aq) junctions are superior to those for the n-GaAs/1.0 M KOH(aq)-0.8 M Se^{2-}(aq)-0.1 M Se$_2^{2-}$ system. At light intensities sufficient to provide photocurrent densities of 20 mA-cm^{-2}, V_{oc} values are similar for the two different electrolytes. The n-GaAs/Te$^{-/2-}$(aq) junction data of Fig. 6 are generally in agreement with expectations based on the lower light intensity measurements of Burk *et al.* in contact with aqueous 7.5 M KOH-0.2 M Te^{2-}, <0.006 M Te$_2^{2-}$ solutions,[33] but indicate substantially higher V_{oc} values and fill factors than reported by Ellis *et al.* for n-GaAs samples in contact with aqueous 5.0 M NaOH-0.1 M Te^{2-} solutions.[25]

Figure 7 displays the I-V properties of the n-GaAs/1.0 M KOH(aq)-0.3 M Te^{2-}(aq)-0.01 M Te$_2^{2-}$(aq) interface after the n-GaAs anode had been exposed to solutions of the various group VIIIB transition metal ions. To facilitate direct comparison of the fill factor and V_{oc} values for the different electrolyte systems of interest, the data in this figure were collected at comparable short-circuit photocurrent densities. It is apparent that metal ions that have been reported previously to improve the fill factor at the n-GaAs/KOH-Se$^{-/2-}$(aq) interface[7,17-19,34] also have a beneficial effect at the n-GaAs/KOH-Te$^{-/2-}$(aq) junction. However, the relative magnitude of the fill factor improvements are distinctly higher in contact with the Se$^{-/2-}$(aq) electrolyte, as evidenced by the data of Figure 7 and by the quantitative data presented in Table II for the n-GaAs/KOH-Se$^{-/2-}$(aq)[17-19] and n-GaAs/KOH-Te$^{-/2-}$(aq) I-V properties.

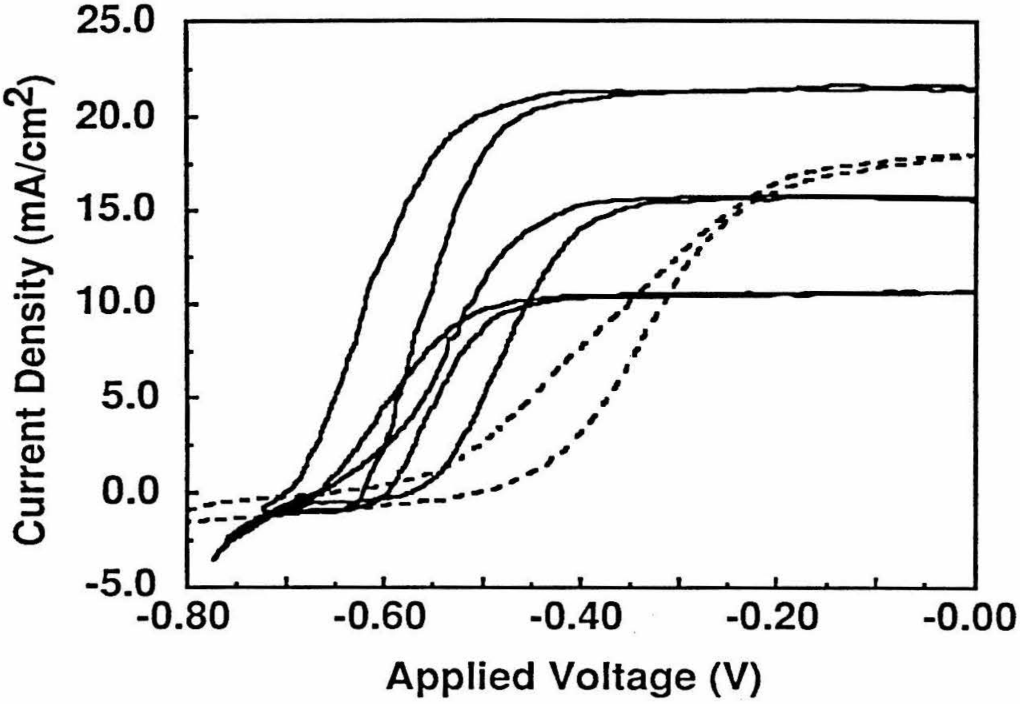

Figure 6. Photocurrent-voltage behavior of n-GaAs(100) anodes in aqueous 1.0 M KOH-0.3 M K_2Te-0.01 M K_2Te_2. The light intensity was adjusted to obtain the desired photocurrent density in each case. For comparison, the dashed line indicates the I-V behavior of n-GaAs in aqueous 1.0 M KOH-0.8 M K_2Se-0.1 M K_2Se_2.[18]

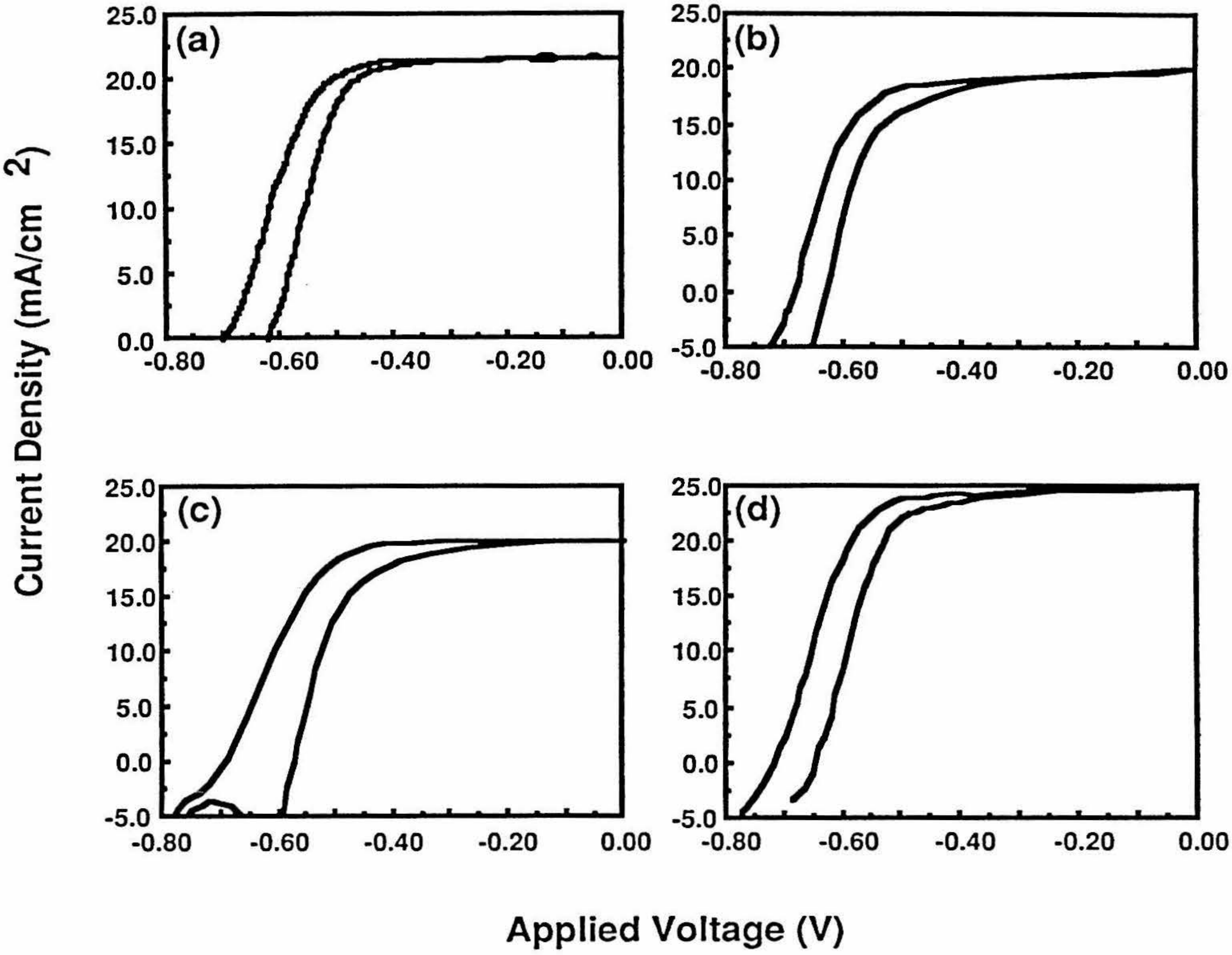

Figure 7. Photocurrent-voltage behavior of n-GaAs(100) anodes in contact with aqueous 1.0 M KOH-0.3 M K_2Te-0.01 M K_2Te_2. (a) Etched GaAs surface; (b) Ru(III) treated surface; (c) $[Co(NH_3)_6]^{3+}$ treated surface; (d) Os(III) treated surface.

Table II. Comparison of I-V characteristics of GaAs in contact with 1.0 M KOH-0.8 M Se^{2-}-0.1 M $Se_2{}^{2-}$, 1.0 M KOH-0.1 M Se^{2-}-0.01 M $Se_2{}^{2-}$, and 1.0 M KOH 0.3 M Te^{2-}-0.01 M $Te_2{}^{2-}$ electrolytes.

Electrolytes	Sample	$J_{sc}{}^a$ mA-cm^{-2}	$V_{oc}{}^b$ mV	$V_{max}{}^c$ mV	$J_{max}{}^d$ mA-cm^{-2}	FF^e	ff$_{rel}{}^f$
0.8 M Se^{2-} [g]	4:1:1 H_2SO_4:H_2O_2:H_2O etched	20.0	660	306	17.2	0.40	0.54
	60s in 0.01 M $OsCl_3$(pH=2.0)	20.0	819	627	18.4	0.70	0.95
	60s in 0.01 M $Co(NH_3)_6Cl_3$ (pH=12.0)	20.0	752	611	18.3	0.74	1.00
	60s in 0.01 M $RuCl_3$(pH=2.0)	20.0	743	559	18.5	0.70	0.95
0.1 M Se^{2-} [h]	0.05% Br_2/CH_3OH etched	20	635	273	17.0	0.37	0.50
	60s in 0.01 M $OsCl_3$(pH=2.0)	21	753	545	17.8	0.62	0.84
	60s in 0.01 M $Co(NH_3)_6Cl_3$ (pH=12.0)	21	688	523	17.5	0.64	0.86
	60s in 0.01 M $RuCl_3$(pH=2.0)	21	706	544	17.3	0.64	0.86
0.3 M Te^{2-} [i]	0.05% Br_2/CH_3OH etched	21	608	430	18.8	0.62	0.84
	60s in 0.01 M $OsCl_3$(pH=2.0)	25	691	522	22.33	0.67	0.91
	60s in 0.01 M $Co(NH_3)_6Cl_3$ (pH=12.0)	20	623	465	17.9	0.67	0.91
	60s in 0.01 M $RuCl_3$(pH=2.0)	20	659	518	17.9	0.70	0.95

(a) Short-circuit current density, ± 1 mA-cm^{-2}. (b) Open-circuit voltage, ± 40 mV unless otherwise specified. (c) Photovoltage developed at the maximum power point, ± 40 mV unless otherwise specified. (d) Photocurrent density at the maximum power point, ± 0.5 mA-cm^{-2}. (e) fill factor: FF = $(V_{max}J_{max})/(V_{oc}J_{sc})$, ± 0.08. (f) Fill factor relative to absolute fill factor of GaAs($Co(NH_3)_6Cl_3$ treated) in 0.8 M Se^{2-} electrolytes. ff_{rel} = FF/0.74. (g) Aqueous 1.0 M KOH - 0.8 M K_2Se - 0.1 M K_2Se_2 electrolytes. Data are from Table V ref.18. (h) Aqueous 1.0 M KOH - 0.10 M K_2Se - 0.01 M K_2Se_2 electrolytes. (i) Aqueous 1.0 M KOH - 0.3 M K_2Te - 0.01 M K_2Te_2 electrolytes.

4. I-V Data of p-GaAs and In_2O_3 in Aqueous 1.0 M KOH-0.3 M Te^{2-} Solutions:

Figures 8-10 show I-V data for p-GaAs anodes and for Sn-doped In_2O_3 electrodes in 1.0 M KOH(aq)-0.3 M Te^{2-}(aq)-0.01 M Te_2^{2-}(aq) solutions. The general behavior of metal ion chemisorption on these surfaces is in accord with prior observations for these samples in 1.0 M KOH(aq)-0.8 M Se^{2-}(aq)-0.1 M Se_2^{2-}(aq) solutions.[17-19] Relative to the etched surfaces, poorer rectification properties are observed for metal-ion-treated p-GaAs electrodes, and higher cathodic and anodic currents were observed for metal-ion-treated Sn-doped In_2O_3 surfaces. The general behavior of these surfaces is consistent with an electrocatalytic effect of the various metal ions on the oxidation of Te^{2-}(aq); additionally, the improved properties of the etched electrode surfaces themselves suggest that the uncatalyzed oxidation of Te^{2-}(aq) is more facile than the uncatalyzed oxidation of Se^{2-} (aq) at Sn-doped In_2O_3 surfaces. A more complete, quantitative, analysis of this I-V data was not performed, because the complicated speciation of the basic chalcogenide solutions[35,36] precludes a straightforward interpretation of the exchange current densities and reaction orders of these systems. However, this analysis was not needed to support any of the mechanistic conclusions obtained from the I-V data or corrosion data on the GaAs/$X^{-/2-}$(aq) (X=Se, Te) interfaces.

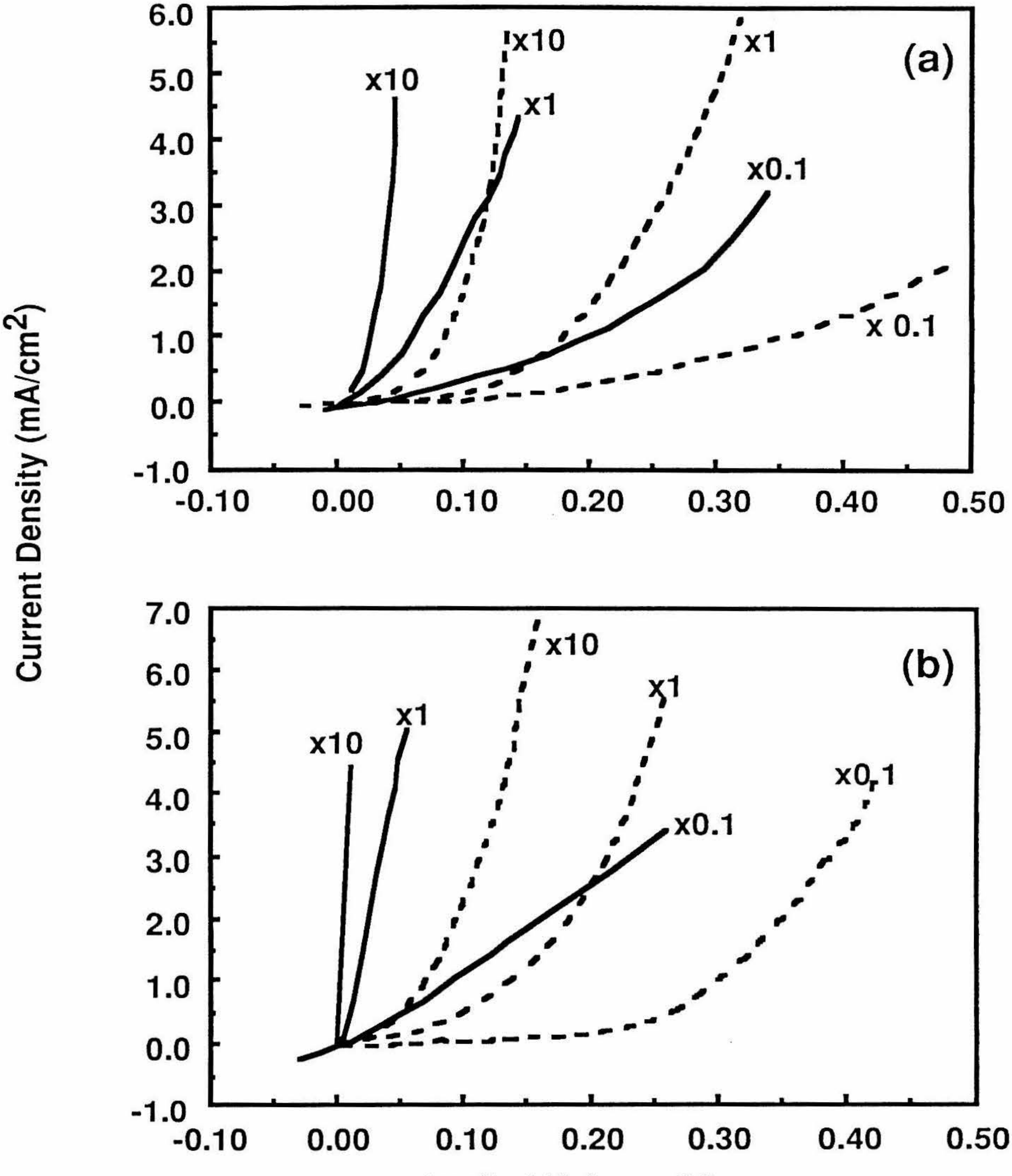

Figure 8. Photocurrent-voltage behavior of p-GaAs and Sn-doped In_2O_3 electrode surfaces in aqueous 1.0 M KOH-0.3 M K_2Te-0.01 M K_2Te_2. Dashed lines are for etched surfaces, while solid lines indicate responses obtained after etching and exposure to 0.010 M aqueous $RuCl_3 \cdot 3H_2O$ (pH = 2.0). (a) Dark current-voltage properties of p-GaAs(100) cathodes. (b) I-V behavior of 10% Sn-doped In_2O_3 electrodes.

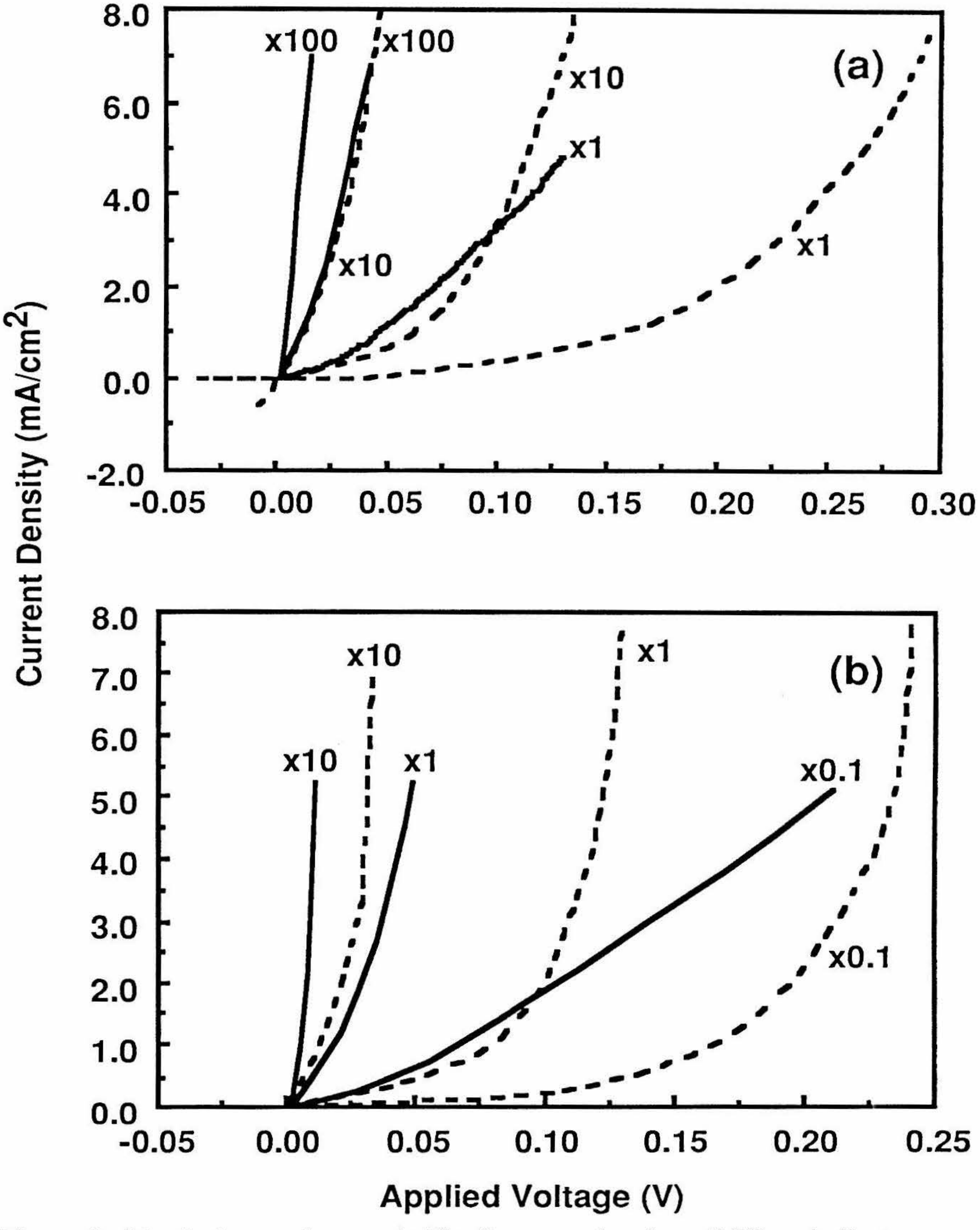

Figure 9. Identical procedures as in Fig. 8, except that the solid lines indicate responses obtained after etching and exposure of the electrodes to aqueous 0.010 M [Co(NH$_3$)$_6$]Cl$_3$ (pH = 12). (a) Dark current-voltage properties of p-GaAs(100) cathodes. (b) I-V behavior of 10% Sn-doped In$_2$O$_3$ electrodes.

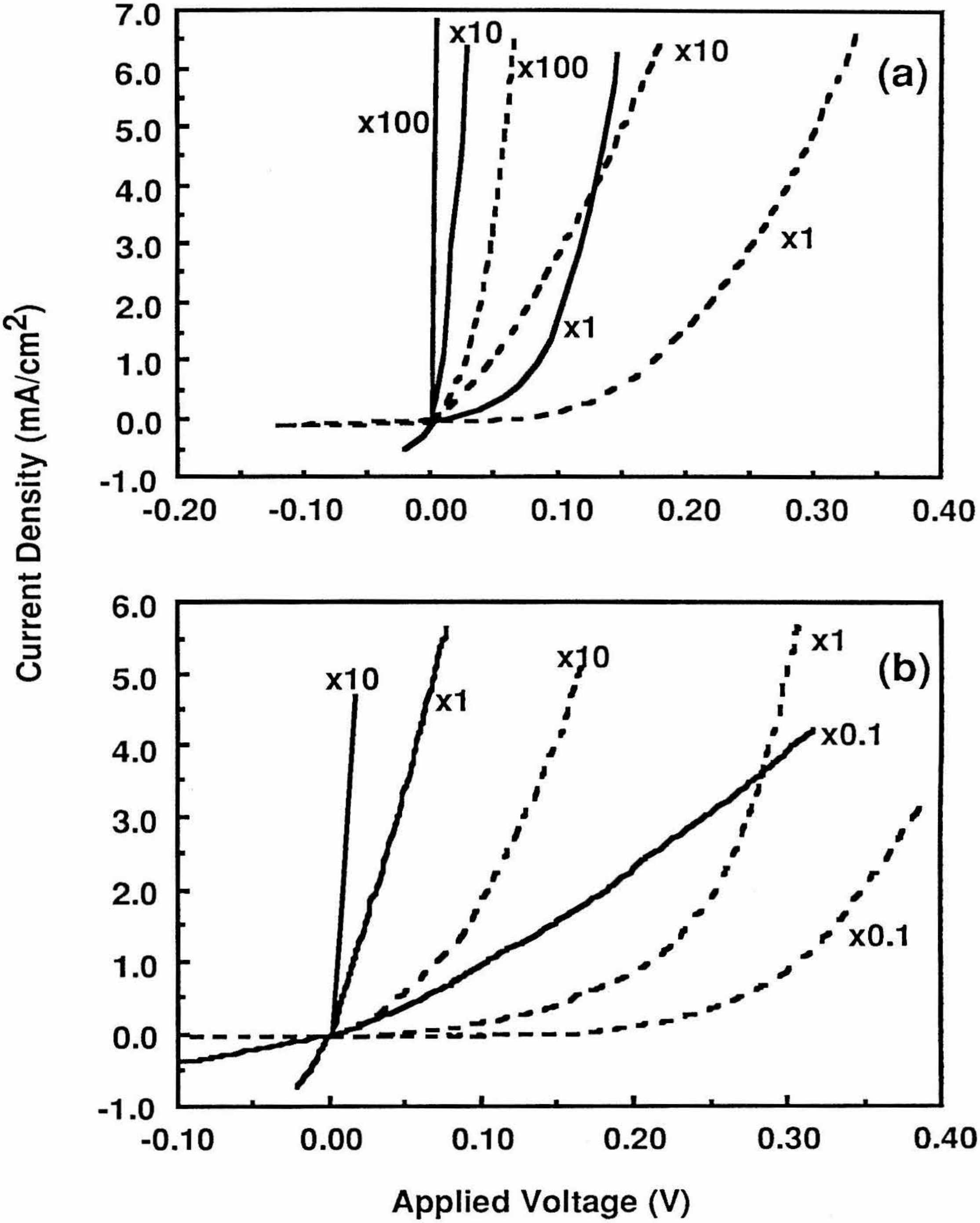

Figure 10. Identical procedures as in Fig. 8, except that the solid lines indicate responses obtained after etching and exposure of the electrodes to aqueous 0.010 M $OsCl_3 \cdot 3H_2O$ (pH = 2.0). (a) Dark current-voltage properties of p-GaAs(100) cathodes. (b) I-V behavior of 10% Sn-doped In_2O_3 electrodes.

IV. DISCUSSION

The suppression of photoanodic corrosion by chemisorption of various transition metal ions (Table I, Fig. 5) suggests that the primary role of metal-ion treatment on n-GaAs photoanodes is to increase the rate of hole transfer to the Se^{2-}(aq) donor ions.[17-19] The improvement in n-GaAs I-V properties in contact with 1.0 M KOH(aq)-0.10 M Se^{2-}(aq)-0.01 M Se_2^{2-}(aq) (Figs. 3 and 4) indicates that the ratio $(k_p+k_{corr})/(k_p+k_{corr}+k_{p,surf})$ has increased after metal ion chemisorption. The improved GaAs photoanodic stability (Table I) indicates that the ratio $k_{corr}/(k_p+k_{corr})$ has simultaneously decreased in contact with this same electrolyte. These combined observations clearly demonstrate that an increase in the minority carrier charge transfer rate (k_p) is the only mechanism advanced to date that is consistent with the available data.

The increase in k_p is consistent with all of the other electrochemical data collected to date on the behavior of GaAs/KOH-$Se^{-/2-}$ (aq) interfaces.[17-19] Furthermore, the trends in GaAs chemistry for the 1.0 M KOH(aq)-0.10 M K_2Se(aq)-0.01 M K_2Se_2(aq) and 1.0 M KOH(aq)-0.3 M K_2Te(aq)-0.01 M K_2Te_2(aq) electrolytes are similar to those found previously for the more concentrated 1.0 M KOH(aq)-0.8 M K_2Se(aq)-0.1 M K_2Se_2(aq) electrolyte.[17-21] These earlier experiments indicates that the best electrocatalyst is obtained from chemisorption of Os (as either $OsCl_3 \cdot 3H_2O$ or K_2OsCl_6) onto GaAs surfaces,[17] and the present data for n-GaAs surfaces in contact with more dilute $Se^{-/2-}$(aq) electrolytes and in contact with KOH-$Te^{-/2-}$(aq) electrolytes are consistent with this conclusion. Additionally, the hypothesis that metal-ion chemisorption acts primarily to increase k_p in these electrolytes is consistent with the lack of metal-ion-chemisorption effects on the I-V behavior of the n-GaAs/CH_3CN-ferrocene$^{+/0}$ contact,[18,37,38] because etched n-GaAs is expected to have a high k_p value in this electrolyte without the presence of any chemisorbed metal ions.

Several aspects of the photoanodic corrosion measurements are of particular interest. First, the electrocatalytic nature of the chemisorbed metal ions leads to photoanode stability in electrolytes where corrosion would otherwise occur readily; thus, the discovery of electrocatalysts for Se^{2-} oxidation also simultaneously enables the rational design of stable photoelectrochemical cells in dilute basic chalcogenide media. The application of these electrocatalysts should not be restricted *a priori* to the n-GaAs photoanode system, and it is expected that many other electrode surfaces could be modified to achieve similar stability and efficiency increases in contact with aqueous chalcogenide electrolytes.

Another interesting feature of the photocorrosion data is the pronounced effect of the electrode edge regions in the formation of dissolved Ga and As ions. The nonuniform electric fields at the edge of the crystal, a propensity to form defects and etch pits at the electrode/epoxy seals, inefficient mass transport, and possible reductions in the coverage and stability of chemisorbed metal ions in the edge areas, presumably all contribute to the enhanced corrosion rates in the edge areas of the GaAs sample. The beneficial metal-ion-induced I-V properties, and beneficial anode stabilization effects, are expected to be very sensitive to any stimulus that would act to initiate local corrosion, because the chemisorbed metal ion coverage is only in the sub-monolayer to 10 monolayer range.[29] When the thin layer of GaAs containing the metal ion is removed, the corrosion properties of the surface are expected to revert to those of the etched electrode in the dilute electrolyte medium, and the local electrode I-V performance should also revert to that of the etched surface. All of these predictions are in accord with the observations made in this work.

With respect to the generality of this observation, an increased corrosion rate has been observed previously at step sites of van der Waals surfaces relative to corrosion rates at defect free regions of such crystals.[39] However, we are not aware of prior experimental observations of differential corrosion effects that are initiated in the edge regions of homogeneous photoelectrode crystals. The observation of this effect implies that care must be taken in interpreting corrosion measurements on very small semiconductor samples, and suggests that some electrode surfaces may possibly be less susceptible to photocorrosion than is indicated by measurements in the literature.

The behavior of the p-GaAs and Sn-doped In_2O_3 electrodes in the KOH-$Te^{-/2-}$(aq) electrolyte is also consistent with an electrocatalytic role for metal ion chemisorption on GaAs surfaces. A reduction in surface recombination rates should result in better rectification properties at p-type GaAs surfaces, but higher currents at a given applied voltage, and poorer rectification properties, were observed in earlier studies of metal ion chemisorption on p-GaAs in contact with the KOH-$Se^{-/2-}$(aq).[17,18] Similar trends are apparent in the data reported herein for the KOH-$Te^{-/2-}$(aq) medium, and argue for the presence of an electrocatalytic effect. Additional evidence for an electrocatalytic effect of metal ion chemisorption is provided by the increased currents observed at Sn-doped In_2O_3 electrodes in contact with KOH-$Se^{-/2-}$(aq) and KOH-$Te^{-/2-}$(aq) electrolytes.

The increased stability to photocorrosion of n-GaAs in contact with basic 0.1 M $Te^{-/2-}$(aq) relative to that in contact with 0.1 M $Se^{-/2-}$(aq) implies that etched GaAs surfaces have a larger rate of hole transfer to the $Te^{-/2-}$(aq) redox couple than to the $Se^{-/2-}$(aq) redox couple. Taken together with the photocorrosion data of Table I, it is extremely difficult to construct a consistent explanation for the metal ion chemisorption effects based on a mechanism involving primarily the passivation of surface recombination (reduction in $k_{p,surf}$).

V. CONCLUSION

The studies of the photoelectrochemical behavior and the stability of GaAs in contact with KOH-$Se^{-/2-}$(aq) demonstrate the electrocatalytic effects of chemisorbed metal ions to the minority carrier transfer rate (k_p). Steady state I-V experiments with n and p-GaAs, n^+-GaAs, and Sn-doped In_2O_3 in KOH-$Te^{-/2-}$(aq) solutions also provide additional supports for this mechanism. The fundamental understandings of the effects of chemically modification to the semiconductor photo-electrodes are important in the rational design of high efficiency and stable semiconductor/liquid junction aqueous solar cells.

References:

(1) Heller, A. *Acc. Chem. Res.* **1981**, *14*, 154.

(2) Wrighton, M. S. *Acc. Chem. Res.* **1979**, *12*, 303.

(3) Rajeshwar, K. *J. Appl. Electrochem.* **1985**, *15*, 1.

(4) Parkinson, B. *Acc. Chem. Res.* **1984**, *17*, 431.

(5) Lewis, N. S. *Acc. Chem. Res.* **1990**, *23*, 176.

(6) Bolts, J. M.; Bocarsly, A. B.; Palazzotto, M. C.; Walton, E. G.; Lewis, N. S.; Wrighton, M. S. *J. Am. Chem. Soc.* **1979**, *101*, 1378.

(7) Heller, A.; Parkinson, B. A.; Miller, B. *Appl. Phys. Lett.* **1984**, *45*, 423.

(8) Heller, A.; Leamy, H. J.; Miller, B.; Johnson, W. D., Jr. *J. Phys. Chem.* **1983**, *87*, 3239.

(9) Keung, L. K.; Meyer, G. J.; Lisensky, G. C.; Ellis, A. B. *J. Phys. Chem.* **1990**, *94*, 1214.

(10) Rubin, H.-D.; Humphrey, B. D.; Bocarsly, A. B. *Nature* **1984**, *308*, 339.

(11) Natan, M. J.; Thackeray, J. W.; Wrighton, M. S. *J. Phys. Chem.* **1986**, *90*, 4089.

(12) Mandel, K. C.; Basu, S.; Bose, D. N. *J. Phys. Chem.* **1987**, *91*, 4011.

(13) Lewerenz, H. J.; Goslowsky, H. *J. Appl. Phys.* **1988**, *63*, 2420.

(14) Hodes, G. *Appl. Phys. Lett.* **1989**, *54*, 2085.

(15) Folmer, J. C. W.; Turner, J. A.; Parkinson, B. A. *Inorg. Chem.* **1985**, *24*, 4028.

(16) Schubert, B.; Tributsch, H. *Inorg. Chem.* **1990**, *29*, 5041.

(17) Tufts, B. J.; Abrahams, I. L.; Santangelo, P. G.; Ryba, G. N.; Casagrande, L. G.; Lewis, N. S. *Nature* **1987**, *326*, 861.

(18) Tufts, B. J.; Abrahams, I. L.; Casagrande, L. G.; Lewis, N. S. *J. Phys. Chem.* **1989**, *93*, 3260.

(19) Abrahams, I. L.; Casagrande, L. G.; Rosenblum, M. D.; Rosenbluth, M. L.; Santangelo, P. G.; Tufts, B. J.; Lewis, N. S. *New J. Chem.* **1987**, *11*, 157.

(20) Heller, A. *ACS Symp. Ser.* **1981**, *146*, 57.

(21) Allongue, P.; Cachet, H. *J. Electrochem. Soc.* **1984**, *131*, 2861.

(22) Gerischer, H. *Ber. Bunsen-Ges. Phys. Chem.* **1965**, *69*, 578.

(23) Finklea, H. O. *Semiconductor Electrodes*; Elsevier: New York, 1988; Vol. 55.

(24) Chang, K. C.; Heller, A.; Schwartz, B.; Menezes, S.; Miller, B. *Science* **1977**, *196*, 1097.

(25) Ellis, A. B.; Bolts, J. M.; Kaiser, S. W.; Wrighton, M. S. *J. Am. Chem. Soc.* **1977**, *99*, 2848.

(26) Rosenbluth, M. L.; Lewis, N. S. *J. Am. Chem. Soc.* **1986**, *108*, 4689.

(27) Stocker, H. J.; Aspnes, D. E. *Appl. Phys. Lett.* **1983**, *42*, 85.

(28) Tufts, B. J.; Casagrande, L. G.; Lewis, N. S.; Grunthaner, F. J. *Appl. Phys. Lett.* **1990**, *57*, 2262.

(29) Tufts, B. J.; Abrahams, I. L.; Caley, C. E.; Lunt, S. R.; Miskelly, G. M.; Sailor, M. J.; Santangelo, P. G.; Lewis, N. S.; Roe, A. L.; Hodgson, K. O. *J. Am. Chem. Soc.* **1990**, *112*, 5123.

(30) Lewis, N. S.; Dominguez, R.; Gronet, C. M.; Lieber, C. M.; Rosenblum, M. D.; Cogan, G. W.; Gibbons, J. F.; Moddel, G. R. In *The Electrochemical Society*; Pennington, NJ, 1984; pp 460.

(31) Fahrenbruch, A. L.; Bube, R. H. *Fundamentals of Solar Cells: Photovoltaic Solar Energy Conversion*; Academic: New York, 1983.

(32) Koval, C. A.; Segar, P. R. *J. Am. Chem. Soc.* **1989**, *111*, 2004.

(33) Burk, Jr., A. A.; Johnson, P. B.; Hobson, W. S.; Ellis, A. B. *J. Appl. Phys.* **1986**, *59*, 1621.

(34) Parkinson, B. A.; Heller, A.; Miller, B. *J. Electrochem. Soc.* **1979**, *126*, 954.

(35) Lessner, P.; Winnick, J.; McLarnon, F. R.; Cairns, E. J. *J. Electrochem. Soc.* **1986**, *133*, 2517.

(36) Lessner, P.; McLarnon, F. R.; Winnick, J.; Cairns, E. J. *J. Electrochem. Soc.* **1987**, *134*, 2669.

(37) Rosenbluth, M. L.; Casagrande, L. G.; Tufts, B. J.; Lewis, N. S. In *Conference Record of the 18th IEEE Photovoltaic Specialists Conference*; IEEE: Las Vegas, 1985; pp 1405.

(38) Bansal, A.; Tan, M. X.; Tufts, B. J.; Lewis, N. S. *J. Phys. Chem.* **1993**, *97*, 7309.

(39) Gerischer, H. In *ACS Symp. Ser.*; 1981; pp 1.

Chapter 3

Direct Electrochemical Measurements of Heterogeneous Electron Transfer Rates at Si/Liquid Interfaces

Abstract: The majority carrier (electrons) transfer rate constant at a highly doped n^+-Si/$Co(Cp)_2Cl$-methanol junction has been measured directly using the chronoamperometry electrochemical technique. The reduction reaction rate of $Co(Cp)_2^+$ is 0.03 $cm\text{-}s^{-1}$ at the Si electrode, and is more than 100 times slower than at a hanging mercury electrode surface. The slower rate of reaction is attributed to the small optical and static dielectric constants, and the low density of electrons at the semiconductor electrode. The experimental results are compared to the Marcus theory of heterogeneous charge transfer processes.

I. INTRODUCTION

As discussed in Chapter 1, one of the criteria for a high efficiency semiconductor/liquid junction solar cell is that the majority carrier transfer rate remains sluggish at the semiconductor/liquid interface, so that the photo-generated minority carriers can react efficiently with the solution electron donor species, with minimum recombination at the interface. In this chapter, the effect of various factors such as the semiconductor dielectric constant, semiconductor band structure, and the density of electron filled and empty states at the semiconductor/liquid interface on the majority carrier transfer process are examined. Our direct measurement of the charge transfer rate constant at a semiconductor electrode provides opportunities to construct theoretical models for the charge transfer processes at a semiconductor/liquid junction,[1] which are important for the rational design of high efficiency, high stability semiconductor/liquid junction solar cells.

The majority carrier transfer rate can be separated into three terms: the majority carrier concentration, the solution acceptor concentration, and the charge transfer rate constant. For an n-type semiconductor with electrons as the majority carriers, the electron transfer rate at the semiconductor/liquid junction, dA/dt, can be expressed as:[1]

$$\frac{dA}{dt} = -k_{et}[n_s][A] \qquad (1)$$

where $[n_s]$ is the electron concentration per cm^3 at the semiconductor/liquid interface; k_{et} is the electron transfer rate constant at the interface with units of cm^4-s^{-1} and [A] is the number of electron acceptor species in the solution per cm^3 volume. dA/dt has units of $cm^{-2}s^{-1}$, and represents the flux of A molecules reacting per centimeter squared surface area of the electrode per second.

The value of $[n_s]$ is determined by the dopant concentration in the semiconductor, and the electric field gradient at the semiconductor/liquid interface. For a typical n-semiconductor/liquid junction solar cell, a surface electric potential of 0.5 V can reduce n_s to approximately 10^{-9}th the dopant concentration.[2] Therefore, the electron transfer rate can be minimized by establishing a strong electric field at the semiconductor/liquid interface, which reduces the value of n_s and therefore dA/dt. It is also important to control the rate constant, k_{et}, at the semiconductor surface. However, the effects of various factors (especially the semiconductor intrinsic properties) on the value of k_{et} remain unclear. To investigate this charge transfer rate constant, we have compared the transfer process at a semiconductor electrode with the process at a metal electrode.

In the field of metal electrode electrochemistry, theories and experiments have suggested that the heterogeneous reaction rate of solution redox species at a metal electrode follows the Marcus theory of charge transfer. The metal phase is equivalent to an ideal contacting phase with an infinitely high concentration of electrons and empty electronic states for donating and accepting electrons from the solution, and with an infinitely high dielectric constant, which enables the metal to respond quickly to changes in the net electric charge in the solution phase resulting from the electron transfer process.[3-5] These conditions can not be satisfied at a semiconductor electrode. The unique band structure of a semiconductor results in a lower density of empty and filled energy states compared to the density of states in a metal, thus reducing the probability of charge transfer from the electrode to the solution. The charge transfer rate at a semiconductor electrode should therefore be slower than at a metal electrode.[6] Marcus theory also suggests that the activation energies for the charge transfer process are different at metal and semiconductor electrodes due to differences in the dielectric constants of the two electrodes.[7] Smith *et al.* have suggested that such differences in the dielectric constants can result in a charge transfer rate that is two orders of magnitude lower at a semiconductor electrode than at a metal electrode.[8] To understand how these various factors control the charge transfer rate at a semiconductor/liquid interface, a direct comparison of the charge transfer rate constant at a semiconductor and a metal electrode is necessary. However, due to various experimental difficulties, there have been very few direct measurements of electron transfer rates at semiconductor/liquid interfaces.[1]

It should be noted that the electron transfer rate constants measured at a metal electrode can not be compared directly to the value of k_{et} for a semiconductor. At a metal electrode,

$$\frac{dA}{dt} = -k_m[A] \tag{2}$$

where k_m is the heterogeneous rate constant at the metal and has units of cm-s^{-1}. The concentration of electrons at a metal electrode surface is greater than 10^{22} cm^{-3} and usually remains a constant during the electrochemical experiments; it does not appear in the rate expression for a metal electrode (Eq. 2), and is incorporated into k_m. Therefore, we must compare k_m to the product of k_{et} and $[n_s]$ at a semiconductor electrode, k_{sc}. The rate constant, k_{sc}, is the heterogeneous reaction rate constant of a solution redox couple at a semiconductor electrode, and has units of cm-s^{-1}.

In this chapter, the electron transfer processes at a highly doped n$^+$-Si electrode and at a hanging mercury electrode (HME), in a methanol (CH_3OH) solution of $Co(Cp)_2Cl$, are measured using the chronoamperometric (CA) technique. We have chosen highly doped Si materials to minimize the resistance of the electrode. Because the formal redox potential ($E^{o'}$) of $Co(Cp)_2$ is very close to the conduction band edge of the Si, the n$^+$-Si/liquid junction is in accumulation, and has a high density of empty and filled energy states at the semiconductor surface, similar to the metal case.[9] If the differences in the dielectric constants can indeed result in a charge transfer rate that is two orders of magnitude smaller at a semiconductor electrode compared to at a metal electrode as predicted by Smith *et al.*, k_{sc} should be at least 100 times smaller than k_m. Because it is likely that the electron density at the semiconductor surface in accumulation (>10^{19} cm^{-3} dopant density) is still lower than the density at a metal surface (>10^{22} cm^{-3}), the value of k_{sc} should then be even smaller than the value predicted from the dielectric constant calculations.

II. EXPERIMENTAL

The highly doped (100) oriented, front surface polished n$^+$-Si single crystal was donated by Puresil. The dopant concentration of the sample was 9×10^{18} cm^{-3} and the sample thickness was approximately 500 μm. The electrodes were prepared using the methods described by Gronet *et al.*[10] Prior to each electrochemical experiment, the Si electrode was etched in 48% HF solution (Mallinckrodt) for 15-20s, then rinsed with methanol.

The hanging mercury electrode was a micrometer-type HME (Metrohm 290). Triple distilled mercury (Bethlehem Apparatus Co.) was used as received. The area of the Hg drop used in the experiments was 0.022 ± 0.002 cm^2.

The electrochemical cell contained 3 electrodes. An HME or a Si electrode was used as the working electrode. A reference electrode containing an Ag wire in saturated LiCl-CH_3OH solution was separated from the cell electrolyte by a Vycor-frit. The potential of the reference electrode was checked against a saturated calomel electrode (SCE) before and after each experiment, and the changes in potential were within 1 mV. A Pt gauze electrode (2 cm x 1 cm) was used as the counter electrode. To minimize cell RC problems, the relative positions of the three electrodes were arranged as shown in Fig. 1. All electrochemical experiments were performed in a sealed Plexiglas anaerobic chamber ("Fish Tank"), with a constant flow of N_2 through the box.

An EG&G Princeton Applied Research (PAR) model 273 potentiostat was used for the electrochemical experiments reported here. The rise time of the potential step function was less than 50 µs at 1 mA full scale. Headstart Creative Electrochemistry Software 1.3 (EG&G) was used to collect the current decay profile in a time frame of 0 to 1s with 1.5 ms resolution. Data was analyzed using the Genplot application PC-software.

Cobaltocenium hexafluorophosphate was purchased from Aldrich, and was converted to the Cl^- salt by ion-exchange chromatography with DEAE-Sephadex A-50 resin.[11] LiCl was dried by heating to approximately 250 °C overnight under vacuum. $Co(Cp)_2Cl$ and LiCl were stored under N_2 in a glove box. Methanol was distilled from Mg powder, and stored over 3-Å sieves under N_2.

The concentration of the $Co(Cp)_2Cl$-LiCl-CH_3OH solution was calculated from the UV-Vis absorption peak at 404 nm against standard acetonitrile solutions of $Co(Cp)_2PF_6$ in air. This method assumed that the absorption coefficient of $Co(Cp)_2Cl$ in CH_3OH solution was the same as the coefficient of $Co(Cp)_2PF_6$ in acetonitrile solution, and might introduce a systematic error in the calculation for $Co(Cp)_2^+$ concentrations. However, this error would only contribute to a constant deviation in the diffusion coefficient reported here from the actual diffusion coefficient of $Co(Cp)_2^+$, but would not alter other values obtained in our electrochemical experiments because of the method of analysis.

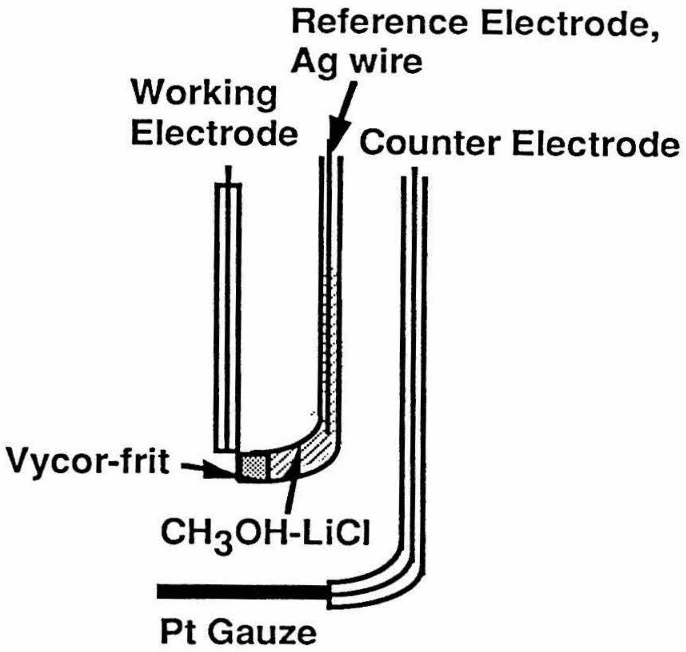

Figure 1. A schematic representation of the relative positions of the three electrodes in the electrochemical cell.

III. RESULTS

1. Cyclic Voltammetric Measurements at HME and Si Electrodes:

The cyclic voltammetry (CV) results of the HME and the Si electrode in $Co(Cp)_2^+$-CH_3OH solutions are displayed in Fig. 2a and 3a. The shape of the CVs obtained at both electrodes are similar, and their cathodic peak currents display a linear relationship with the square root of the scan rate, $v^{1/2}$ (Fig. 2b and 3b). These results demonstrate that the highly doped Si electrode does not display rectifying behavior in the $Co(Cp)_2^+$ solution, and the common electrochemical techniques used for metal electrodes are applicable to our semiconductor electrode/liquid junction.

The peak cathodic current (i) is proportional to the square-root of the scan rate (v). When the reaction rate at an electrode surface is fast (reversible), the diffusion process determines the shape of the CV curves. At 25 °C, assuming a one electron reaction, we can express i as:[12]

$$i = 2.69\times10^5\, A C_o^* \sqrt{D_o v} \qquad (3)$$

where A is the area of the electrode (cm^2), C_o^* and D_o are the bulk concentration (mol-cm^{-3}) and the diffusion coefficient (cm^2-s^{-1}) of electron acceptors in the solution, respectively. When the reaction rate is slow (quasi-reversible), the shape of the CV is determined by the kinetics of the reaction and the diffusion process, and the peak current is smaller than the purely diffusion controlled current.

$$i = 2.69 x 10^5 A C_o^* \sqrt{D_o v \delta} \tag{4}$$

where δ is a unitless parameter ($\delta<1$) that is related to the charge transfer rate constant, the transfer coefficient for the forward and reverse electron transfer reaction, the diffusion constants of the electron acceptors and donors, and the scan rate, v.[12] Therefore, the reduction peak current should not increase linearly with $v^{1/2}$. The linear dependence of the cathodic current on $v^{1/2}$ observed (Fig. 2b and 3b) suggests that the reaction rate is fast at both electrodes. However, as shown in Table I, the value of the cathodic peak current per unit area and unit $Co(Cp)_2^+$ concentration, i^*, at the Si surface is only similar to the i^* at the HME at scan rates below 400 mV-s^{-1}, but at higher scan rates, the value of i^* at Si exceeds the value at HME. This observation seems to indicate that the charge transfer rate at an HME is slow (quasi-reversible) compared to a Si electrode, and the peak current at an HME is limited by the kinetics of the reaction at higher scan rates. However, the current observed in CV experiments is usually a combination of the faradaic current and the capacitive charging current (i_c), which increases linearly with the scan rate and distorts the CV results at high scan rates. Our observation can also be due to the higher charging currents at the Si electrode compared to at the HME. From the analysis of the measurements of i^* alone, we can not determine the difference in the charge transfer rate constants at the two electrodes.

The potential difference between the cathodic and anodic peak potentials, ΔE_p, should be 59 mV at 25 °C for a one electron reversible reaction, and should increase when the reaction becomes kinetically limited. Both the ΔE_p values measured at the Si and HME electrodes (Table I) are greater than this value due to cell resistance losses. However, at the HME electrode, the peak to peak separation is 70 ± 2 mV at $v \leq 500$ mV-s^{-1} independent of the scan rate, while ΔE_p at a Si electrode exceeds 72 mV at $v \geq 200$ mV and increases with the scan rate. This result seems to suggest that the charge transfer rate at HME is faster than at Si. However, we can not extrapolate the values of charge transfer rate constants from these CV studies due to cell capacitance and resistance interferences.

Overall, the CV curves obtained at the HME and Si electrode closely resemble the shape of the CV predicted for reversible reactions. The diffusion coefficient (D_o) can be calculated from Eq. 3 at each individual scan rate, or from the slope of the cathodic peak current *vs.* $v^{1/2}$ plot. The average D_o value of 6.5 ± 1.5 cm^2-s^{-1} obtained from these CV curves (Fig. 2b, 3b and Table I) will be compared to the D_o calculated from the CA experiments later. The formal potential for the reduction/oxidation of $Co(Cp)_2^{+/0}$ ($E^{o'}$) can also be obtained from the CV curves, $E^{o'} = E_{1/2} - (RT/F)\ln\xi$, where $E_{1/2}$ is half wave potential and $\xi=(D_o/D_r)^{1/2}$, D_r is the diffusion coefficient of $Co(Cp)_2$. By assuming $D_r=D_o$, $E^{o'} \approx E_{1/2}$, therefore, $E^{o'}$ is -844 ± 3 mV *vs.* the Ag/LiCl-CH_3OH reference (Table I), which is -948 mV *vs.* the SCE.

Table I. The CV results obtained at HME and Si electrodes in a 5.4 mM $Co(Cp)_2Cl$-1.0M LiCl-CH_3OH solution at various scan rates.

	Scan Rate (mV-s^{-1})	i^{*a} (Acm-mol^{-1})	$\Delta E_p{}^b$ (mV)	$D_o{}^c$ (cm^2-s^{-1})	$E_{1/2}{}^d$ (mV)
HME	50	169	68	$8x10^{-6}$	-842
	200	324	70	$7x10^{-6}$	-843
	400	444	68	$7x10^{-6}$	-844
	500	480	72	$7x10^{-6}$	-846
	600	531	76	$6x10^{-6}$	-844
	1000	629	86	$6x10^{-6}$	-847
	1500	798	90	$6x10^{-6}$	-847
Si	50	157	68	$7x10^{-6}$	-842
	100	222	70	$7x10^{-6}$	-841
	200	321	72	$7x10^{-6}$	-842
	300	393	76	$7x10^{-6}$	-840
	400	443	80	$7x10^{-6}$	-842
	500	492	86	$7x10^{-6}$	-845
	600	551	92	$7x10^{-6}$	-844
	800	601	98	$6x10^{-6}$	-845
	1000	659	104	$6x10^{-6}$	-846

(a) The cathodic peak current ($Co(Cp)_2^+ + e^- = Co(Cp)_2$) normalized to per unit area (cm^2) and per unit concentration (mol-cm^{-3}). (b) The potential difference between the cathodic peak and the anodic peak. (c) The diffusion coefficient was calculated from i^* using Eq. 3. (d) The $E_{1/2}$ value reported here was measured against an Ag/LiCl-CH_3OH reference electrode, which is about -104 mV from the SCE.

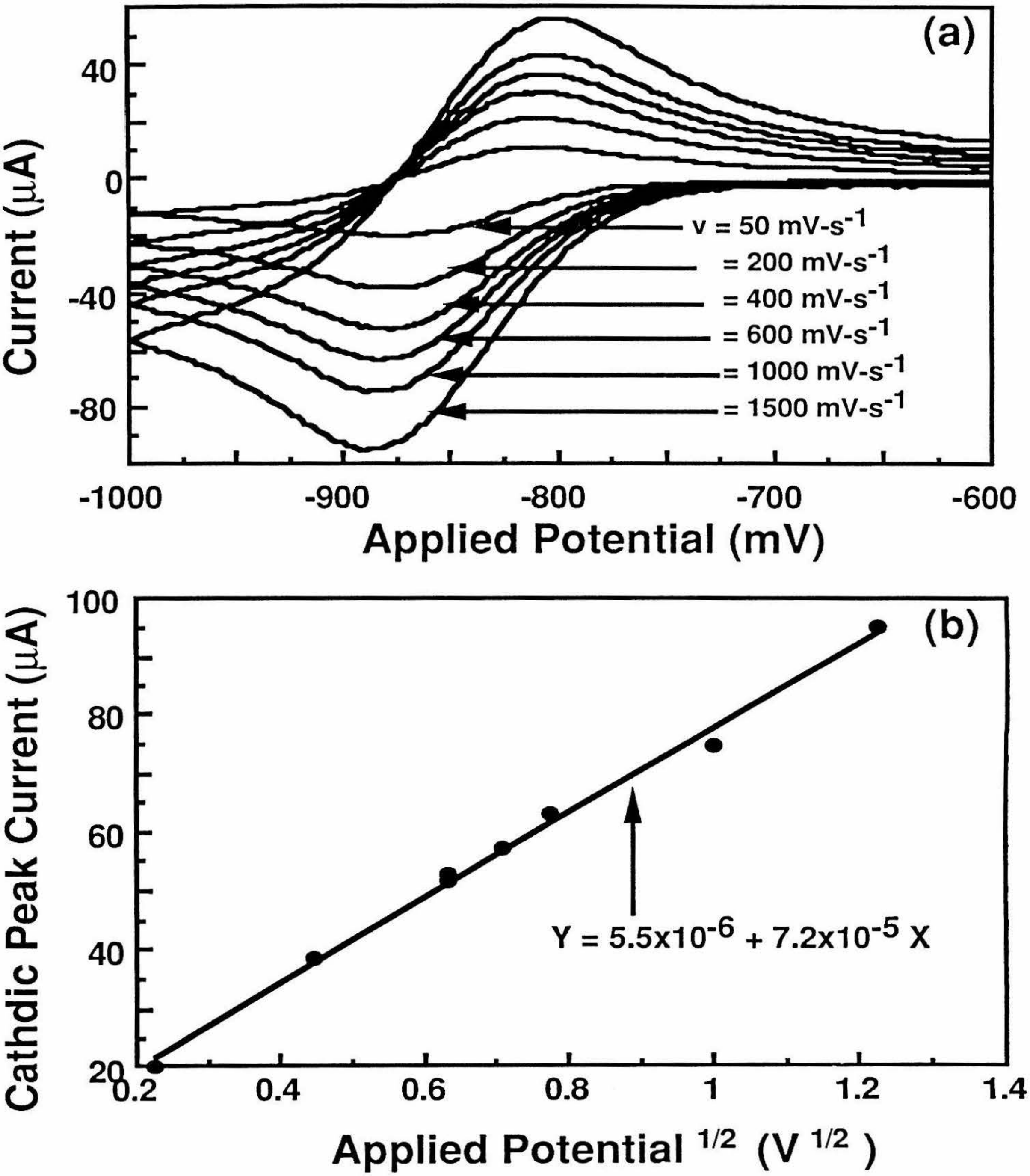

Figure 2. (a) CV results of the HME (0.022 cm^2 area) in a 5.4 mM Co(Cp)$_2$Cl-1.0 M LiCl-CH$_3$OH solution at various scan rates (v). The Ag/LiCl-CH$_3$OH reference electrode potential was -104 mV *vs.* SCE. (b) The linear relationship between the cathodic peak current and v$^{1/2}$. The slope of the linear plot, 7.2x10^{-5} A-V$^{1/2}$, corresponds to a diffusion coefficient (D$_o$) of 5.1x10^{-6} cm^2-s^{-1} (Eq. 3).

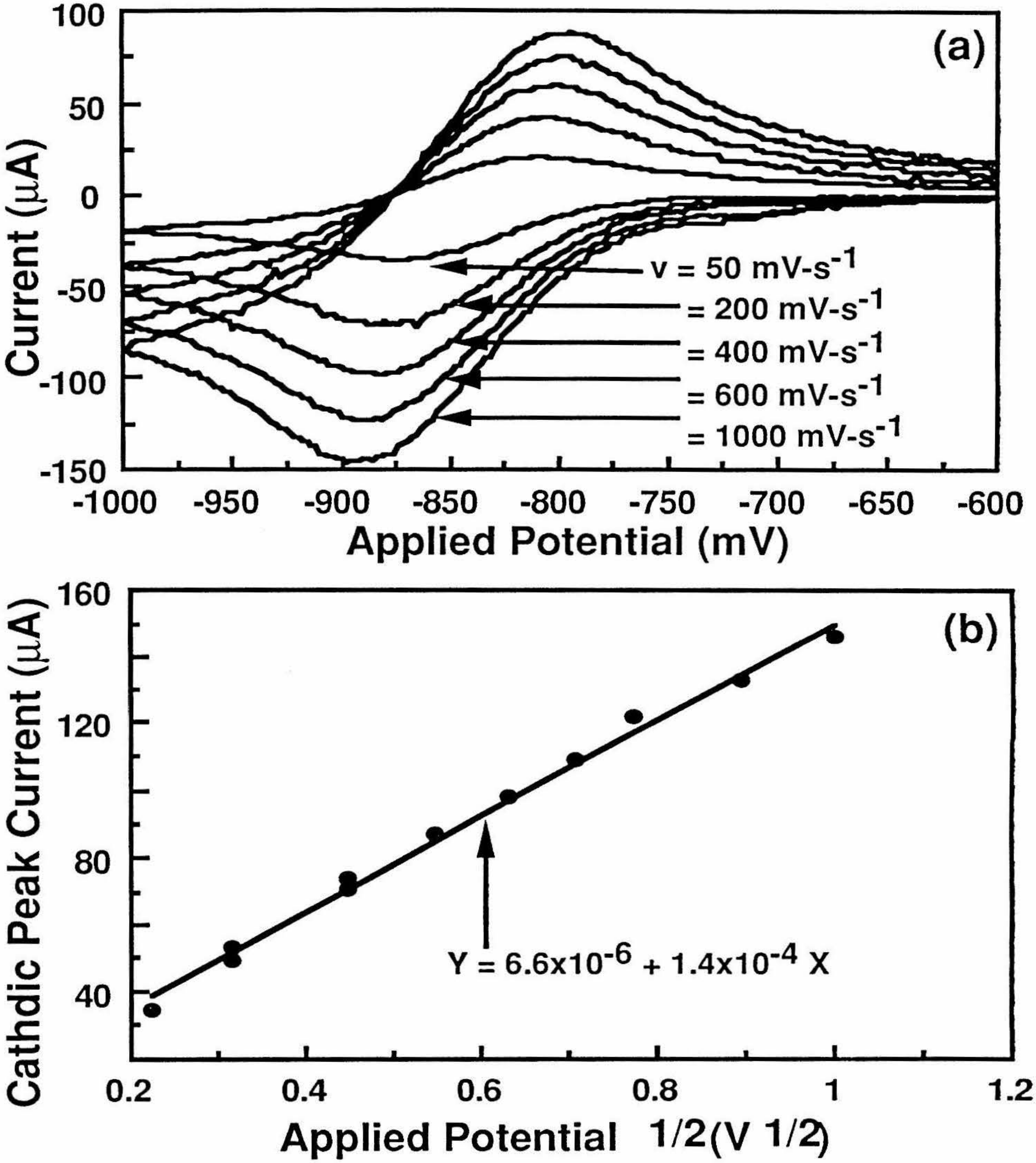

Figure 3. (a) CV results of the Si electrode (0.041 cm^2 area) in a 5.4 mM $Co(Cp)_2Cl$-1.0M LiCl-CH_3OH solution at various scan rates (v). The Ag/LiCl-CH_3OH reference electrode potential was -104 mV *vs.* SCE. (b) The linear relationship between the cathodic peak current and $v^{1/2}$. The slope of the linear plot, $1.4x10^{-4}$ A-$V^{1/2}$, corresponds to a diffusion coefficient (D_o) of $5.5x10^{-6}$ cm^2-s^{-1} (Eq. 3).

2. Chronoamperometric Experiments at the HME:

The CA experiments involve applying a potential step function at the working electrode (E_{rest} to E_{react}), and monitoring the reaction current decay response in real time in a quiescent solution. The potential, E_{rest}, is usually a potential at which no current flows, and the rise-time for the potential step (E_{rest} to E_{react}) is limited by the potentiostat, which is <50 μs for the PAR 273 instrument used in our experiments. E_{react} is a potential where the oxidation or reduction reaction occurs at the electrode.

As shown in Fig. 4a, when the potential of the HME is stepped from -400 mV *vs.* the solution reference electrode to -875 mV, the reduction of $Co(Cp)_2^+$ to $Co(Cp)_2$ results in cathodic current at the HME. If the heterogeneous reaction rate is fast at the Hg surface, the cathodic current will be determined by the flux of $Co(Cp)_2^+$ diffusing toward the electrode due to the concentration gradient between the electrode surface and the bulk of the solution. Assuming a linear diffusion process,[13] the current *vs.* time (t) relationship for the one electron reduction process of $Co(Cp)_2^+$ is:[12]

$$i(t) = \frac{FAD_o^{1/2}C_o^*}{\pi^{1/2}t^{1/2}(1+\xi\theta)} \tag{5}$$

where F is the Faraday constant, and $\theta = \exp[(E_{\text{react}}-E^{0'})F/RT]$. A plot of i(t) *vs.* $t^{-1/2}$ should yield a straight line, with a slope proportional to the area of the electrode, the square-root of the diffusion coefficient, and the $Co(Cp)_2^+$ concentration in the solution. As shown in Fig. 4b, this linear relationship is satisfied at the HME. The diffusion coefficient calculated from the slope of the i(t) *vs.* $t^{-1/2}$ plot at potential steps from -800 mV to 1V *vs.* the solution reference (-892 to 1092 mV *vs.* the SCE) varies from 5.4×10^{-6} to 7.8×10^{-6} $cm^2\text{-}s^{-1}$ (at $E^{o'} = -948$ mV *vs.* the SCE), which is similar to the diffusion coefficient calculated from the CV experiments. These results suggest that the heterogeneous reaction rate constant at HME is reversible when the CA or CV electrochemical techniques are used, *i.e.*, the rate constant is greater than 0.1 $cm\text{-}s^{-1}$.[12] Our results agree with prior electrochemical studies of $Co(Cp)_2$ redox reactions at metal electrodes using AC impedance methods, or at ultra-micro Pt electrodes, which have suggested a reaction rate constant between 6 and 200 $cm\text{-}s^{-1}$.[14-16]

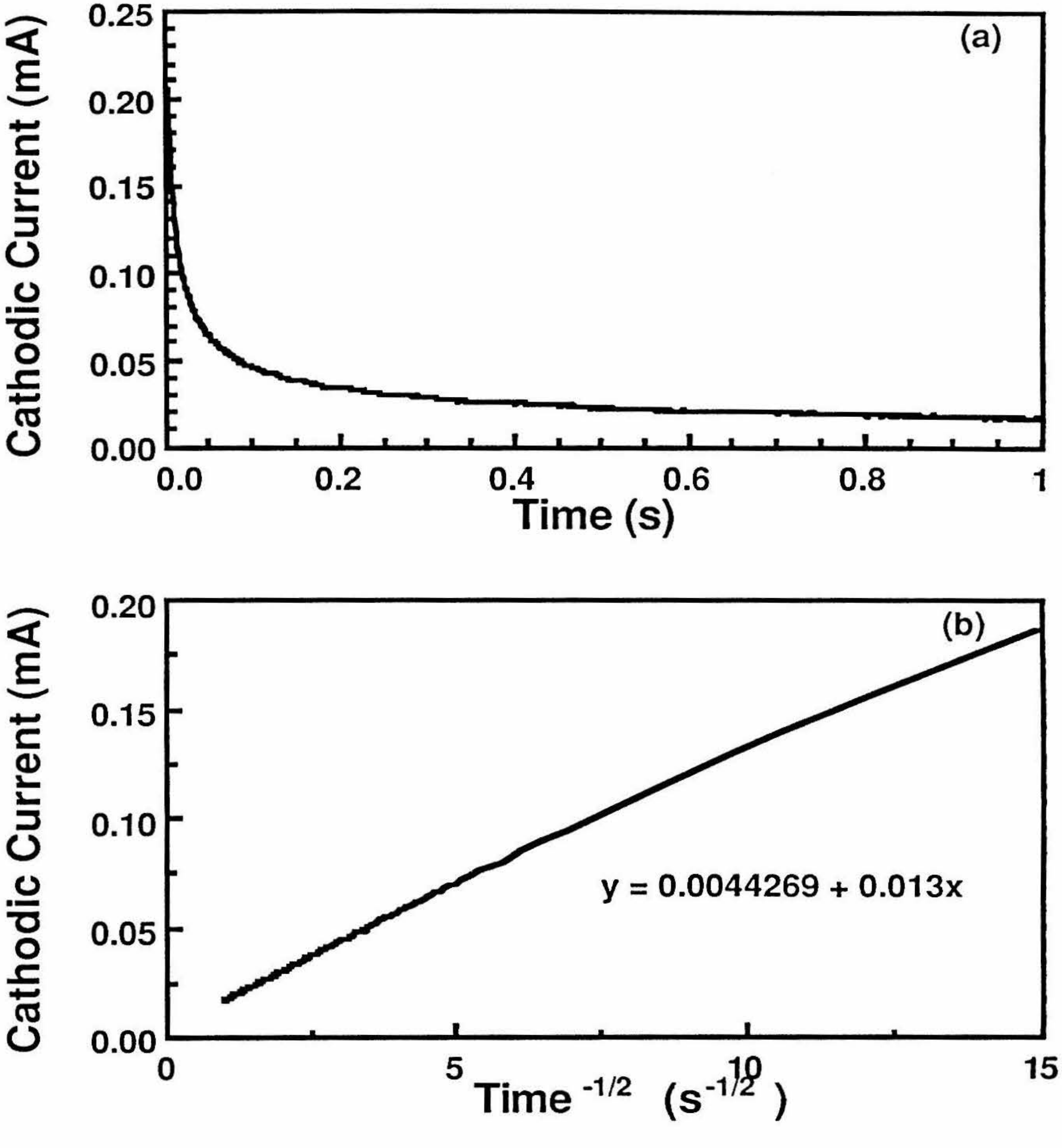

Figure 4. The CA results at an HME in a 5.4 mM $Co(Cp)_2Cl$-1.0M $LiCl-CH_3OH$ solution. The Ag/$LiCl-CH_3OH$ reference electrode was -104 mV vs. the SCE. (a) The cathodic current response *vs*. time, as a potential of -875 mV was applied to the electrode. (b) The linear relationship between i(t) and $t^{-1/2}$. The slope of the line, 0.013 mA-$s^{-1/2}$, corresponds to a diffusion coefficient of $6.8x10^{-6}$ cm^2-s^{-1}.

3. *Chronoamperometric Experiments at the Si Electrodes:*

When the reaction rate constant is slow, the current, i(t), will be limited by both the kinetics of the reaction and the diffusion process:[12]

$$i(t) = FAk_f C_o^* \exp(H^2 t)\mathrm{erfc}(Ht^{1/2}) \tag{6}$$

H is defined as

$$H = \frac{k_f}{D_o^{1/2}} + \frac{k_b}{D_r^{1/2}} \tag{7}$$

k_f and k_b are the heterogeneous rate constants for the reduction and oxidation reactions, respectively, $k_f = k^o \exp[(E_{react}-E^{0'})\alpha F/RT]$ and $k_b = k^o \exp[-(E_{react}-E^{0'})(1-\alpha)F/RT]$, where α is the transfer coefficient and k^o is the standard heterogeneous rate constant at HME ($k^o = k_m$, or k_{sc} in this chapter).

Figure 5 demonstrates the typical CA response of a highly doped Si electrode in a $Co(Cp)_2^+$-CH_3OH solution. As shown in Fig. 5a, the plot of i *vs.* $1/t^{1/2}$ does not follow a straight line, indicating a quasi-reversible charge transfer rate at the Si surface. One can use the method of integration to extrapolate the value of k^o from the current decay results. Upon integration of the current from time 0 to t (Eq. 6), the amount of charge passed at the electrode as a function of time, Q(t), can be expressed as:

$$Q(t) = \frac{FAk_f C_o^*}{H^2}\left[\exp(H^2 t)\mathrm{erfc}(Ht^{1/2}) + \frac{2Ht^{1/2}}{\pi^{1/2}} - 1\right] \tag{7}$$

When $Ht^{1/2}>5$, the first term in the brackets is negligible compared to the others, and Eq. 7 simplifies to

$$Q(t) = FAk_f C_o^* \left(\frac{2t^{1/2}}{H\pi^{1/2}} - \frac{1}{H^2}\right) \tag{8}$$

A plot of this faradaic charge *vs.* $t^{1/2}$ yields a straight line with a positive intercept (t_i) on the $t^{1/2}$ axis, which can be related to H by $\pi^{1/2}/2t_i^{1/2}$, and the slope of this line can be used to obtain k_f. Figure 5c demonstrates this linear relationship between Q(t) and $t^{1/2}$. Table II lists the k_f values calculated from such plots at various step potential values.

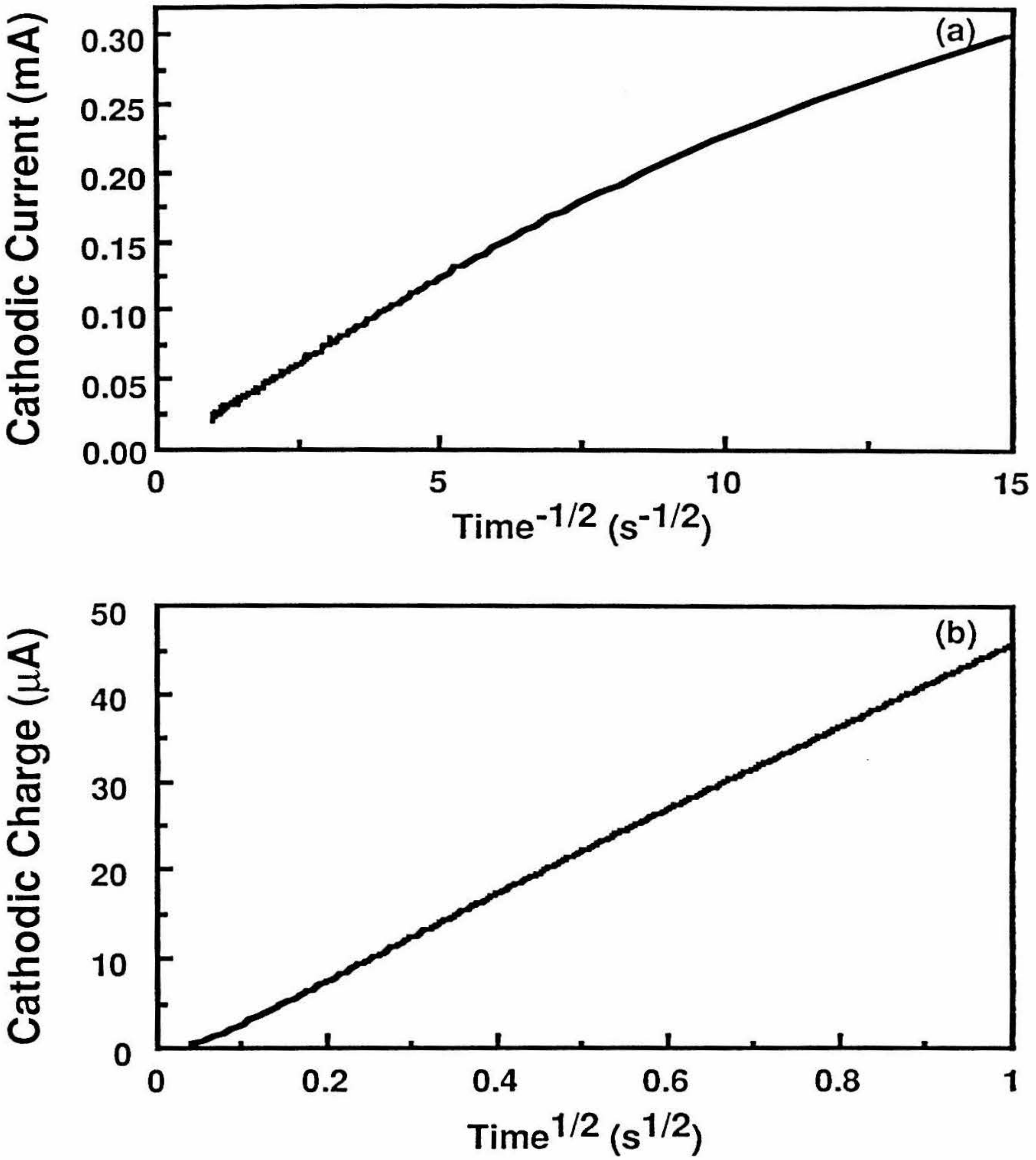

Figure 5. The CA results at a Si electrode (area, A=0.41 cm^2) in a 4.4 mM $Co(Cp)_2Cl$-1.0M $LiCl$-CH_3OH solution as a -875 mV potential was applied to the electrode. The Ag/LiCl-CH_3OH reference electrode was -106 mV *vs*. SCE. The current (or charge) used was the actual current (or charge) minus the current (or charge) collected at the same potential step without the presence of $Co(Cp)_2Cl$. (a) The nonlinear relationship between i(t) and $t^{-1/2}$. (b) The linear relationship between Q(t) and $t^{1/2}$. The results of the linear fit are presented in Table II.

Table II. The H and k_f values obtained from the slope and intercept of the integrated Q *vs.* $t^{1/2}$ plots at various potential steps for Si electrodes in a 4.4 mM $Co(Cp)_2Cl$-1.0M $LiCl-CH_3OH$ solution.

	E_{react} (mV)[c]	Slope of Q *vs.* $t^{1/2}$ ($\mu C\text{-}s^{-1/2}$)	t_i (s)[d]	H ($s^{-1/2}$)	k_f ($cm\text{-}s^{-1}$)	E_{react}-$E^{0'}$ (mV)[e]
Si[a]	-775	4.3	0.59	36.46	0.008	-67
	-800	9.9	0.54	38.22	0.019	-42
	-825	23.0	3.66	14.64	0.017	-17
	-850	36.2	2.42	18.02	0.033	8
	-875	47.9	1.29	24.66	0.060	33
	-900	53.7	0.22	60.41	0.165	58
	-950	56.6[f]	- - -	- - -	- - -	108
	-975	56.5[f]	- - -	- - -	- - -	133
	-1000	56.0[f]	- - -	- - -	- - -	158
Si[b]	-775	13.8	9.86	8.92	0.003	-67
	-800	27.4	5.27	12.20	0.007	-42
	-825	51.9	5.42	12.04	0.013	-17
	-850	83.7	5.21	12.28	0.021	8
	-875	113.0	3.72	14.53	0.034	33
	-900	127.0	1.27	24.84	0.066	58
	-925	132.0	0.17	68.39	0.188	83
	-950	133.0[f]	- - -	- - -	- - -	108

(a) The area of the Si electrode is 0.041 cm^2. (b) The area of the Si electrode is 0.100 cm^{-2}. (c) The potential was measured against an $Ag/LiCl-CH_3OH$ reference electrode, which was -106 mV *vs.* SCE. (d) The value of t_i was calculated from the intercept and the slope of the Q *vs.* $t^{1/2}$ plot. (e)The value of $E^{o'}$ was chosen as the $E_{1/2}$ value obtained from the CV results of -948 mV *vs.* the SCE (Table I). (f) The slope of the plot is independent of the potential at potentials ≥ 108 mV negative of the formal potential of the reaction, and the intercept is positive, *i.e.*, $t_i<0$; therefore, the cathodic reaction is limited by the diffusion process (k_f is greater than 0.1 $cm\text{-}s^{-1}$). The diffusion coefficient can be calculated from the slope of the Q *vs.* $t^{1/2}$ plot using Eq. 9, resulting in $D_o = 8 \pm 2$ $cm^2\text{-}s^{-1}$, which agrees with the D_o obtained at an HME using the CA and CV techniques.

We can then plot $\ln(k_f)$ *vs.* $E_{\mathrm{react}}-E^{o'}$ and obtain the value of k^o and α from the intercept and the slope of the line respectively (the intercept should be $\ln(k^o)$ and the slope is $\alpha F/RT$). As shown in Fig. 6, the average rate constant k_{sc} (k^o) is approximately 0.03 ± 0.01 cm-s^{-1}. Compared to the CA and CV results obtained at the HME and prior studies of $Co(Cp)_2^+$ reduction at metal electrodes,[15,16] the reaction rate constant at Si is more than 100 times slower than at Hg. This result agrees qualitatively with the predictions of the charge transfer theory, and we will discuss in detail the physical significance of this result in the discussion section.

In electrochemistry, the method of measuring the total amount of charge passed at an electrode *vs.* time is called chronocoulometry. Because of the instrumental limitations imposed by the PAR 273 potentiostat, we can not perform this measurement of Q(t) directly. Instead, we have integrated the data collected from the CA experiments to obtain Q(t). Therefore, it should be noted that the rate constant results obtained from the Q *vs.* $t^{1/2}$ plots in this study are not directly from the analysis of chronocoulometric responses of the electrode, but merely a mathematical method used in CA data analysis. In this case, a zero offset in the current output from the potentiostat could introduce an error in Q(t), and therefore, in the calculated value of k_f and H. To examine this factor, we have calculated the value of the diffusion coefficient, D_o, from the slope of Q *vs.* $t^{1/2}$ plots at higher potential steps, where the reaction appears to be reversible (Table II). In this case the Q(t) response should follow the integrated diffusion controlled i(t) response, namely Eq. 5:

$$Q(t) = \frac{2FAD_o^{1/2}C_o^{*}t^{1/2}}{\pi^{1/2}(1+\xi\theta)} \tag{9}$$

A plot of Q *vs.* $t^{1/2}$ should give a line with a slope that is proportional to the square-root of D_o. As shown in Table II, the value of D_o is the same (within error range) as the D_o obtained from the CV experiments on both the Si and HME, and the D_o obtained from CA experiments on the HME. Therefore, we can conclude that such an error is negligible in our integration process.

We have chosen to analyze the integrated Q(t) responses over the directly measured i(t) results because of the complicated fitting procedures required in the i *vs.* t analysis. Although Eq. 6 can be simplified at very short time scales by expanding the product of the exponential term and the error function,[12] data analysis are required in the first 50 μs for a k^o value on the order of 0.01 cm-s^{-1}, at a potential step of 25 mV past the formal potential. Instrumental limitations preclude accurate measurements on this time scale. One can also choose to fit the i(t) function directly. However, the fitting routine must include a complicated linear expansion term to satisfy over a wide range of x ($x=Ht^{1/2}$), which requires large computing capabilities. The method of fitting for the integrated Q(t) function at longer times is much simpler compared to the fitting for the i(t) function.

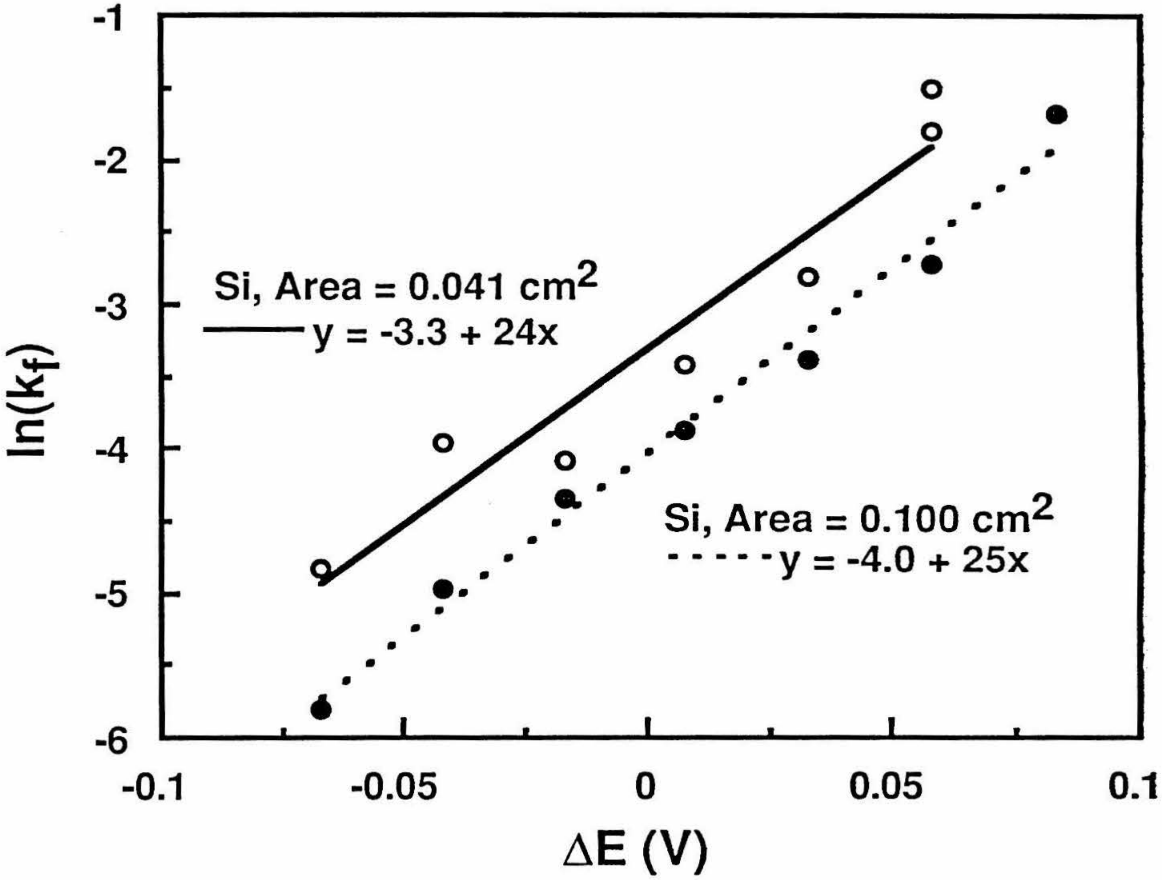

Figure 6. The linear plot of $\ln(k_f)$ *vs.* $E_{react}-E^{o'}$ using data listed in Table II. Because $k_f = k^o \exp[(E_{react}-E^{0'})\alpha F/RT]$, we have $\ln(k_f) = \ln(k^o) + \alpha F/RT(E_{react}-E^{o'})$, assuming a one electron reaction. The k^o value is 0.04 and 0.02 $cm\text{-}s^{-1}$ at the two Si electrodes, and the calculated transfer coefficient for the $Co(Cp)_2^+$ to $Co(Cp)_2$ reaction is approximately 0.6 at 25°C.

IV. DISCUSSION

Marcus has derived an expression for the heterogeneous electron transfer rate constant at a metal electrode as:[4,17]

$$k_m = \kappa Z \exp(-\lambda / 4kT) \tag{11}$$

where k is the Boltzmann constant, k_m is the standard heterogeneous rate constant at a metal, and is independent of any applied potential at the electrode, and κ is the transition probability. For a reaction in which there is substantial electronic coupling between the reactants (an adiabatic reaction), κ is 1. Z is the attempt frequency for the reaction and is approximated as the gas phase collision frequency (10^5 cm-s^{-1}) at a metal electrode. λ is the activation energy (reorganization energy) for the reaction.

$$\lambda = \lambda_i + \lambda_o \tag{12}$$

λ_i accounts for the vibrational reorganization of reactants and products, and λ_o accounts for the outer shell solvent reorganization during the reaction. For the reaction of $Co(Cp)_2^+$, studies of the homogeneous self exchange reaction rate have suggested that the electron transfer reaction occurs without perturbing significantly the structure of the molecule. Therefore, the λ_i term is relatively small and the solvent reorganization energy, λ_o, dominates the reorganization energy, λ.[16] At a metal electrode, when a molecule with positive charge (for example $Co(Cp)_2^+$) is near the metal surface, a negative charge, called the image charge, exists in the metal. When an electron is transferred from the metal to the molecule during the reduction process, the net charge on the molecule becomes zero (for example $Co(Cp)_2$), and the high dielectric constant of the metal enables the image charge to change immediately, requiring virtually no extra energy. Only the reorganization of the solution dipole contributes to the λ_o term, and therefore, the overall λ term. We can express λ_o as:

$$\lambda_o = \frac{(ne)^2}{2}\left(\frac{1}{D_1^{op}} - \frac{1}{D_1^{s}}\right)\left(\frac{1}{a} - \frac{1}{R}\right) \tag{13}$$

where ne is the number of charges transferred from the electrode to the reactant, D_1^{op} is the optical dielectric constant of the solvent, and D_1^{s} is the static dielectric constant of the solvent. The optical and static dielectric constants for metals are close to infinity, and their contributions are omitted in the calculation of λ_o. The radius of the reactant is denoted by a, and R is equal to 2d, where d is the distance from the center of the reactant to the surface of the electrode.[4,5,17] Using Eqs. 11-13, we can calculate a λ_o value of approximately

25kT at a metal electrode, assuming a k_m value of 200 cm-s^{-1} for the $Co(Cp)_2^+$ reduction.[14-16]

An equation similar to Eq. 11 can be used to express the charge transfer rate constant at a semiconductor electrode:

$$k_{sc} = C_{sc} \exp(-\lambda / 4kT) \tag{14}$$

where C_{sc} is a constant related to the probability of reaction, and electronic coupling between the solution and the electrode energy states.

The optical and static dielectric constants are much smaller at semiconductors than metals; the static dielectric constant of Si is only 11.7 relative to the permittivity in vacuum. The optical dielectric constant is highly frequency dependent because of the band structure of the semiconducting material. Therefore, we must incorporate these constants into the equation for λ_o. This is accomplished through modification of the Marcus equations derived for electron transfer rates between two immiscible solvents with different dielectric constants.[7,8]

$$\lambda_o = \frac{(ne)^2}{2}\left[\frac{1}{a}\left(\frac{1}{D_1^{op}} - \frac{1}{D_1^{s}}\right) - \frac{1}{R}\left(\frac{D_2^{op} - D_1^{op}}{D_2^{op} + D_1^{op}} \bullet \frac{1}{D_1^{op}} - \frac{D_2^{s} - D_1^{s}}{D_2^{s} + D_1^{s}} \bullet \frac{1}{D_1^{s}}\right)\right] \tag{15}$$

D_2^{op} and D_2^s represent the optical and static dielectric constants of the contacting phase respectively. Equation 15 converges to Eq. 13 when D_2^{op} and D_2^s are much larger than D_1^{op} and D_1^s as in the case of a metal electrode.

According to Eqs. 13 and 15, the solvent reorganization energy (λ_o) should be higher at a semiconductor electrode than at a metal (because the second term in the brackets in Eq. 15 is smaller than $1/D_1^{op} + 1/D_1^s$). Therefore, the charge transfer rate constant, k_m, is greater than k_{sc} if the preexponential factor for Eqs. 11 and 14 are similar, *i.e.*, the density of filled and empty states are similar for the two materials. Because the low dielectric constants of a semiconductor cause a smaller shielding effect from the image charge compared to a metal, higher energy is required for the solvent reorganization process. This corresponds to a slower heterogeneous reaction rate constant at the semiconductor.

It has been suggested by Smith *et al.* that for semiconductors such as Si, which has a static dielectric constant of 11.7 (much smaller than the dielectric constant of the metal), the reorganization energy (at the Si electrode) would be at least twice the value at a metal electrode. The charge transfer rate constant (k_{sc}), therefore, can be 100 times smaller than

k_m, if the prefactors are the same for the semiconductor and the metal.[8] However, in this theory, only the static dielectric constant of the semiconductor electrode was considered. According to Eq. 15, a change in the dielectric constants from infinity to 11.7 will only influence the static dielectric contribution to λ_o, but will not alter the contribution from the optical dielectric term, and the overall λ_o may not be significantly larger compared to the λ_o at a metal electrode depending on the value of the optical dielectric constant. For example, if we assume that the reaction only occurs at molecules at the surface of the electrode, R=2d=2a, then the ratio of the solvent reorganization energy at Si, $\lambda_{o,Si}$, and at the metal, $\lambda_{o,m}$ according to Eqs. 13 and 15 is:

$$\frac{\lambda_{o,Si}}{\lambda_{o,m}} = \frac{2\left(\frac{1}{D_1^{op}} + \frac{1}{D_1^{s}}\right) - \left(\frac{D_2^{op} - D_1^{op}}{D_2^{op} + D_1^{op}} \bullet \frac{1}{D_1^{op}} + \frac{D_2^{s} - D_1^{s}}{D_2^{s} + D_1^{s}} \bullet \frac{1}{D_1^{s}}\right)}{\left(\frac{1}{D_1^{op}} + \frac{1}{D_1^{s}}\right)} \qquad (16)$$

Using the value of D_1^{op}=1.76, D_1^{s}=32.7 for CH_3OH,[15] D_2^{s}=11.7 for Si,[9] the ratio of $\lambda_{o,Si}$ to $\lambda_{o,m}$ is 1.19 for a D_2^{op} value of 11.7. This value of Si optical dielectric constant is at frequencies in the infrared region (less than 2.4×10^{14} Hz).[18] At higher frequencies, the optical dielectric constant of the Si can be higher than 40, and the corresponding ratio of $\lambda_{o,Si}$ to $\lambda_{o,m}$ is only 1.005. The calculated value of k_{sc} for the reduction of $Co(Cp)_2^+$, using the same prefactor employed for the metal electrode (10^5 cm-s^{-1}), is 58 cm-s^{-1} (for D_2^{op}= 11.7) and 187 cm-s^{-1} (for D_2^{op}= 40) assuming $\lambda_{o,m}$=25kT. This value is less than four times smaller than the charge transfer rate at a metal (200 cm-s^{-1} in this calculation). According to Eqs. 11-16, only when the D_2^{op} value approaches the dielectric constant of a vacuum, 1, is the calculated k_{sc} value about 0.07 cm-s^{-1}.

The above calculations have employed two major assumptions: k_m is 200 cm-s^{-1} and the prefactors for Eqs. 11 and 14 are the same. In the electrochemical literature, the value of k_m has not yet been accurately determined, with numbers between 6 to 200 cm-s^{-1} being reported.[14-16,19] If we use a k_m value of 6 cm-s^{-1} for the above calculations, k_{sc} would be 0.92 cm-s^{-1} for a D_2^{op} of 11.7. This number is still more than an order of magnitude greater than the measured k_{sc} value of approximately 0.02 cm-s^{-1}. The difference is likely to arise from the second assumption. The prefactor term for a semiconductor electrode (C_{sc}) is related to the density of electrons and the density of empty states near its Fermi energy.[6] For a highly doped Si electrode in depletion, C_{sc} can be significantly lower than for a metal (κZ).[20] In my experiments, the Si has a very high dopant density and is in accumulation; the Fermi level of the Si is actually within the conduction band. The density of filled and empty states around the Fermi energy is much higher when the semiconductor is in accumulation than when the semiconductor is in depletion. However, it is not clear if this density of states is comparable to the density of states around the Fermi energy of a metal ($>10^{22}$ cm^{-3}). Our experimental measurements suggest that the dielectric factor alone does not account for all the difference in the charge transfer rate constants between a metal and a Si electrode. Therefore, the prefactor at the semiconductor electrode must be smaller than at a metal. To distinguish the contribution of the semiconductor dielectric constant and the density of electrons on the charge transfer process at the surface, more quantitative experiments and calculations using Fermi-Dirac statistics must be conducted.

The above discussion also suggests that an accurate value for D_2^{op} must be used in the Marcus equation (Eq. 15) to predict the charge transfer rate constant at a semiconductor. Discussions with Professor Marcus have suggested that the D_2^{op} terms used in Eq. 8 may not be applicable for the semiconductor case,[21] because of the strong frequency dependence of the optical dielectric constant of a semiconductor. Further development of the theory is therefore necessary when considering the influence of dielectric constants on the charge transfer rate at a semiconductor/liquid interface.

V. CONCLUSION

Using standard electrochemical techniques, we have directly measured the charge transfer rate constant at a highly doped Si electrode in $Co(Cp)_2^+$-CH_3OH solution. The heterogeneous rate constant measured using CA at the Si electrode is about 0.02 cm-s^{-1}, and reversible at the HME. The slower charge transfer rate at a semiconductor agrees with the theoretical prediction, where both the low dielectric constant and the low density of surface electrons at a semiconductor can reduce the reaction rate at the electrode surface. More calculations and experiments are necessary to determine the differences in the pre-exponential factor involved in the expression for the rate constants for the metal and the semiconductor electrodes.

References:

(1) Lewis, N. S. *Ann. Rev. Phys. Chem.* **1991**, *42*, 543.

(2) Neudeck, G. W.; Pierret, R. *The PN Junction Diode;* II ed.; Addison-Wesley Publishing Company: Reading, 1989; Vol. II.

(3) Marcus, R. A. *Ann. Rev. Phys. Chem.* **1964**, *15*, 155.

(4) Marcus, R. A. *J. Chem. Phys.* **1965**, *43*, 679.

(5) Marcus, R. A. *Electrochimica Acta* **1968**, *13*, 995.

(6) Morrison, S. R. *Electrochemistry at Semiconductor and Oxidized Metal Electrodes*; Plenum: New York, 1980.

(7) Marcus, R. A. *J. Phys. Chem.* **1990**, *94*, 1050.

(8) Smith, B. B.; Koval, C. A. *J. Electroanal. Chem.* **1990**, *277*, 43.

(9) Sze, S. M. *The Physics of Semiconductor Devices;* 2nd ed.; Wiley: New York, 1981.

(10) Gronet, C. M.; Lewis, N. S.; Cogan, G.; Gibbons, J. *Proc. Natl. Acad. Sci., USA* **1983**, *80*, 1152.

(11) Rosenbluth, M. L.; Lewis, N. S. *J. Am. Chem. Soc.* **1986**, *108*, 4689.

(12) Bard, A. J.; Faulkner, L. R. *Electrochemical Methods: Fundamentals and Applications*; John Wiley & Sons: New York, 1980, pp 629.

(13) Assuming that the HME electrode is a perfect sphere with an area of 0.022 cm^2, we can calculate the radius of the electrode as $\approx$0.04 cm, then within 10% accuracy, the linear diffusion approximation is valid within 0.9 s of the experiment.

(14) Penner, R. M.; Heben, M. J.; Longin, T. L.; Lewis, N. S. *Nature* **1990**, *250*, 1118.

(15) Nielson, R. M.; McManis, G. E.; Golovin, M. N.; Weaver, M. J. *J. Phys. Chem.* **1988**, *92*, 3441.

(16) Gennett, T.; Milner, D. F.; Weaver, M. J. *J. Phys. Chem.* **1985**, *89*, 2787.

(17) Marcus, R. A.; Sutin, N. *Biochim. Biophys. Acta* **1985**, *811*, 265.

(18) Li, H. H. *J. Phys. Chem. Ref. Data* **1980**, *9*, 561.

(19) McManis, G. E.; Golovin, M. N.; Weaver, M. J. *J. Phys. Chem.* **1986**, *90*, 6563.

(20) Gerischer, H. In *Physical Chemistry: An Advanced Treatise*; H. Eyring; D. Henderson and W. Yost, Ed.; Academic: New York, 1970; Vol. 9A; pp 463.

(21) Professor R. A. Marcus, personal communication, November 22, 1991.

Chapter 4

Properties of High Purity Si/Liquid Junction Photoelectrochemical Cells Under High Injection Conditions

Abstract: The unique properties of high purity Si/liquid junctions have been investigated under illumination conditions in which the photogenerated majority carrier concentration exceeds the dopant concentration. Under these high injection conditions, negligible electric fields exist at the semiconductor/liquid interface, and carrier motion is driven by diffusion. In these studies, the current-voltage properties of Si in methanol solutions containing various redox couples suggest that high efficiency photoelectrochemical cells can be established through selective collection of carriers at the semiconductor/liquid junction. Charge separation across 100 μm can be achieved through diffusion gradients, with minimum recombination, even in the absence of electric gradients at the semiconductor/liquid interface. The new electrode design in this work has also allowed direct measurements of the quasi-Fermi levels of electrons and holes against the solution potential. Steady-state and transient photovoltage measurements, and theoretical modeling of the carrier transport, generation, and recombination dynamics indicate that the quasi-Fermi levels are flat across the semiconductor sample under high injection conditions. The recombination velocities at the Si/liquid junctions have also been measured, and are shown to vary with the solution potential following the Shockley-Read-Hall theory on recombination.

Part I. Efficient Carrier Separation Across 100 μm Using Diffusion Gradients at Semiconductor/Liquid Junctions

I. INTRODUCTION

A frequently cited advantage of semiconductor/liquid contacts for chemically-based energy conversion is their efficient quantum yield for charge separation resulting from the presence of a strong electric field at the semiconductor/liquid junction.[1-3] In molecular solar energy conversion systems, charge separation is achieved primarily through the use of chemical potential gradients, and back electron transfer processes are often significant unless substantial free energy is sacrificed in the charge separation steps.[4-6] In contrast, charge carriers created by light absorption near a semiconductor/liquid contact are rapidly separated by the interfacial electric field, producing a photocurrent without extensive free energy losses. These separated charge carriers then diffuse through the electrode, and are collected to perform useful work, unless significant recombination occurs in the bulk of the solid. Most efforts to optimize photoelectrochemical cells for solar energy storage have therefore sought to increase the interfacial electric field strength, thus increasing the effect of drift for charge separation in the near-surface (depletion) region of the solid. The Gärtner model for photocurrent collection,[7] and the "dead-layer" model for determining the radiative luminescence yield of injected charge carriers,[8] are analytical examples of photoelectrochemical behavior that embody this strategy. Such an approach has been quite successful to date, and has resulted in numerous stable photoelectrochemical cells exceeding 10% in solar energy conversion efficiency under 1 Sun, Air Mass (AM) 1.5 illumination conditions.[9-15]

However, this approach has limitations, because there are practical constraints on the maximum electric field strength that can be achieved for a given solid/liquid contact, while simultaneously preventing recombination in the bulk of the crystal. The single crystal n-Si/methanol (CH_3OH)-dimethylferrocene ($Me_2Fc^{+/0}$) contact is one well-documented system for which variation in dopant density, and thus variation in electric field strength at the solid/liquid contact, has been explored in detail.[16] In this system, increases in dopant density (N_d) produce increases in the open-circuit photovoltage (V_{oc}) until $N_d > 10^{17}$ cm^{-3}, after which point Auger recombination and other bulk recombination processes result in a net increase in recombination, and thus effect a reduction in V_{oc}. Essentially the dopants act as impurities, so that increases in N_d produce a decrease in the minority carrier lifetime after a critical electric field strength has been exceeded. An alternative approach to charge separation is therefore required if this photovoltage limit is to be exceeded.[17]

In this chapter, an approach of using diffusion gradients to obtain efficient photoelectrochemical charge separation is described. A thin, high-purity, low-dopant density sample of single crystal Si, with an extremely long minority carrier lifetime, is used as a photoelectrode (Fig. 1).[18,19] Under moderate illumination levels, the concentrations of photogenerated electrons and holes exceed the dopant density of the semiconductor, *i.e.*, the majority carrier concentration (electrons) equals the minority carrier concentration, and the photoelectrode is under high injection. The high concentration of delocalized photogenerated charges minimizes the built-in electric field at the semiconductor/liquid interface.[19-21] In order to obtain efficient charge separation in this system, diffusion gradients must be sustained throughout the crystal. This has been accomplished through the formation of ohmic-selective contacts which only collect electrons or holes at the back side of the sample. Due to this kinetic asymmetry, one carrier type is collected at the back contact, while the other carrier is forced to move, by diffusion, towards the solid/liquid contact (Figs. 1c and d). Provided that recombination in the bulk and at the surfaces of the crystal can be minimized, this approach should provide a method to separate charge with high quantum yield while circumventing the photovoltage limitations that are exhibited by devices that operate with electric field gradients to achieve charge separation.

Another advantage of this approach is that the ohmic-selective electrical contacts at the back of the sample provide a convenient monitor of the electrochemical properties of each individual carrier type, while the sample is being illuminated. The measured potentials at each set of point contacts yield information on the apparent electrochemical potentials, or "quasi-Fermi levels," of the carriers in the solid. Such measurements have allowed us to determine simultaneously the positions of the quasi-Fermi levels of electrons and holes relative to the solution potential at the same semiconductor/liquid junction. Although the quasi-Fermi level positions were measured at the back of the semiconductor relative to the solution potential, Part II of this chapter demonstrates that, because of the fast diffusion process and the low bulk and surface recombination velocity of the particular Si/liquid junction studied, quasi-Fermi levels were essentially flat across the semiconductor solid, and their positions measured at the back contacts were the same as at the semiconductor/liquid interface. These results are relevant to the controversy regarding the thermodynamic interpretation of the quasi-Fermi levels in a photoelectrochemical cell.[22-25]

We note that in prior work, molecular photovoltaic devices such as liquid crystal porphyrins and inorganic metal complexes have displayed significant (and sometimes anomalous) photovoltages due to asymmetric charge carrier quenching processes. Such systems have not, however, produced significant quantum yields for charge collection. Thin films of nearly intrinsic semiconductors, such as CdSe, have shown external quantum yields of less than 20%, as have thin films of amorphous hydrogenated Si.[26] The present studies are important to establish whether it is possible to collect charge with high quantum yield while simultaneously storing significant free energy in a photoelectrochemical cell.

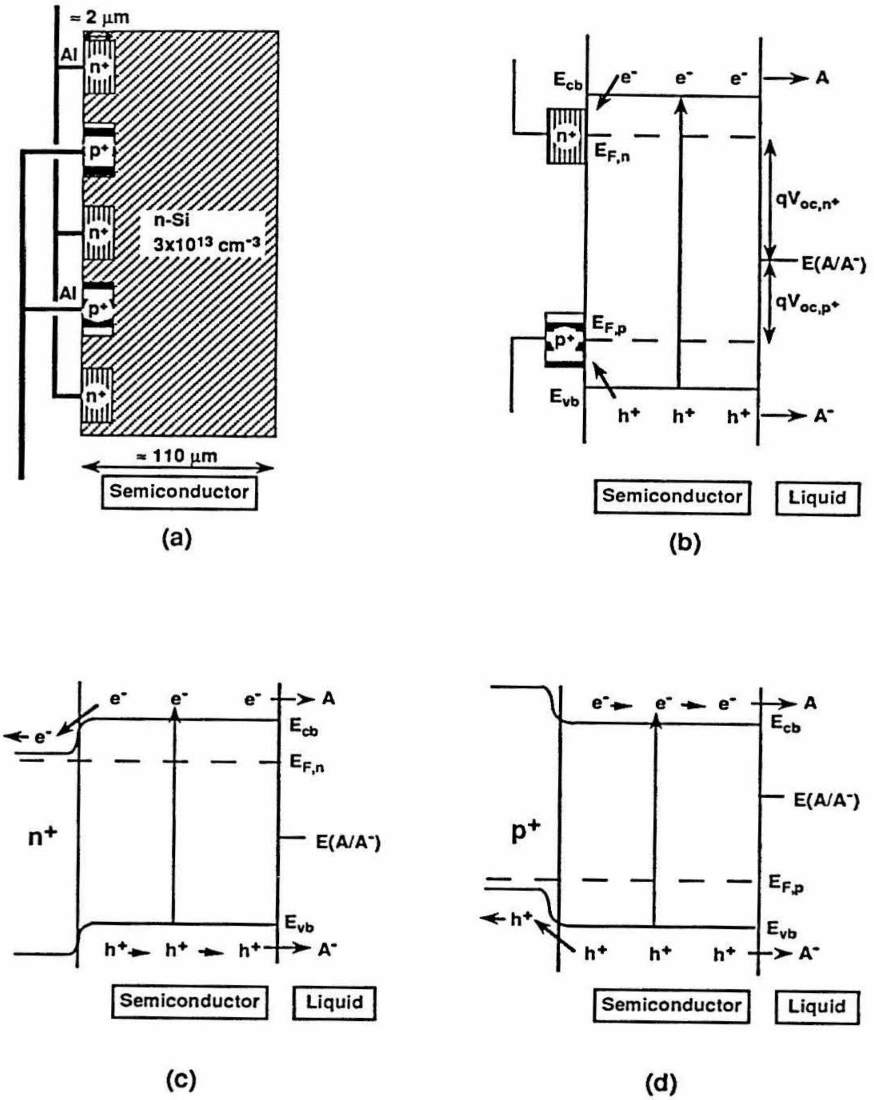

Figure 1. (a) Schematic representation of the high purity Si sample with n^+ and p^+ back contacts. (b) Band diagram of the Si/liquid junction under high injection open-circuited conditions. E_{cb} and E_{vb} represent the conduction band edge and valence band edge of the semiconductor, respectively. $V_{oc,n+}$ and $V_{oc,p+}$ are the open-circuit potentials measured at the n^+ and p^+ contact back points against the solution potential ($E(A/A^-)/q$, q is the elementary charge). The quasi-Fermi levels of electrons and holes are related to the open-circuit potentials by $E_{f,n}=qV_{oc,n+}$, and $E_{f,p}=qV_{oc,p+}$. At the semiconductor/liquid interface, electrons and holes can recombine through reactions with the electron acceptor (A) and donor (A^-) species in the solution. (c) Band diagram of the junction under biased conditions at the n^+ contact points. Electrons are collected from the back of the sample (n^+ region), and holes are collected in the solution. Because of the lack of electric field at the interface for charge separation, electrons can also react with the solution. (d) Band diagram of the junction under biased conditions at the p^+ contact points.

II. EXPERIMENTAL

The Si samples were solid state solar cells provided by SunPower Corp. The float-zone Si substrate was slightly n-doped with a dopant concentration of 3 x 10^{13} cm^{-3}. The lifetime of the sample exceeds 1 ms.[19,27] Highly doped n^+ (8-10 Ω/☐) and p^+ (20 Ω/☐) contact points were fabricated in the back of the sample lithographically, and aluminum contacts were made to the contact points. Each point was approximately 10 x 10 μm in area and 2 μm deep. The n^+ and p^+ points were carefully spaced ≈ 20 μm apart with silicon dioxide passivation layers between the points. This design minimized the leaking current between the n^+ and the p^+ points.[19,28,29] The Si wafer thickness was 120 ± 5 μm, and the total area of the electrode was 1.2 x 1.2 cm^2. The front of the Si was anisotropically etched and coated with a SiO_2 passivation layer and a titanium dioxide layer. The oxide layer minimized the surface recombination of electrons and holes in air, and the anisotropic design and the TiO_2 coating were to minimize the solar reflection.

After receiving the sample, separate electrical wires were soldered onto the Al patches that were connected to the n^+ and p^+ points. The back and edge of the electrode were then sealed in white expoxy (Dexter, Epoxy-patch kit-white) with glass tubing to protect the n^+ and p^+ wires from the solution. The front surface of the electrode had a typical area of 1.1 cm^2. The electrode was soaked in 48% HF solution for 6 minutes to remove to the SiO_2 layer under the TiO_2. The TiO_2 layer was then removed from the Si surface with a cotton swab. The electrode was then etched in a solution of HNO_3:CH_3COOH:HF solution at 15:5:2 volume ratio for 1 minute, followed by a 10s 48% HF etch. XPS studies of the electrode surface confirmed that the TiO_2 layer was completely removed from the surface of the electrode by this treatment. The thickness of the sample was reduced by 8 ± 1 μm as measured with a micrometer. Prior to each electrochemical experiment, the electrode was etched in 48% HF for 20s to remove any thermally-grown oxide.

The photoelectrochemical experiments were performed in a single compartment air-tight Pyrex cell using an ELH-type tungsten-halogen bulb as the illumination source.[17,30] Pt wires and foils were used as the reference and auxiliary electrodes respectively. The current-voltage characteristics of the high purity Si/liquid junction were obtained with the n^+ or the p^+ contacts connected to the lead for the working electrode on the potentiostat (PAR 173 with PAR 175 Programmer). The data was recorded on an Omni-graphic 2000 (Houston Instrument) chart recorder. The open-circuit potential at the other type of contact points (p^+ contacts or n^+ respectively) was monitored against a separate Pt wire that was also immersed in the solution with a Fluke digital multimeter.

The quantum-yield measurements were performed at power levels sufficient to achieve high level injection conditions in the Si sample. At 514.5 and 457.9 nm, the single line outputs of a Coherent Inc. 70-5 Ar^+ laser were used to illuminate the sample while a Coherent Inc. 890 cw Ti:Sapphire laser, pumped by the 5W (all lines) output of the same Ar^+ laser, was used for all other wavelengths. The beam was expanded with 40x Gallilean telescope and then split into a signal beam and a reference beam using a Pyrex slide. A calibrated Si photodiode (United Detector Technology) was used to determine the light intensity of the signal beam. The intensity of the reference beam was continuously monitored with an uncalibrated Si photodiode detector. Photolimiting currents of the sample (under potentiostatic control) were monitored with a Fluke digital multimeter, while simultaneous measurements of the reference beam signal were performed using a similar multimeter.

The redox couples and electrolytes used were prepared according to procedures described previously.[17] The methyl viologen radical ($MV^{+\cdot}$) and cobaltocene ($Co(Cp)_2$) species in the solutions were electrolyzed on a Pt electrode. All solutions were prepared with dry methanol or THF. ACS reagent grade 69% HNO_3 (VWR) and glacial CH_3COOH (Fisher) were used in the etching procedure, and transistar 48% HF solution (Mallinckrodt) was used during the etching process.

III. RESULTS

1. Steady-state current density vs. voltage (J-V) properties of Si/CH_3OH-$Me_2Fc^{+/0}$ contacts:

Figure 2a is the current density (J)-voltage (V) characteristic of a high purity Si electrode in a $Me_2Fc^{+/0}$-CH_3OH solution under a 69 mW-cm^{-2} (≈ AM2 level) illumination intensity of an ELH-type tungsten-halogen lamp, when potentials are applied between the n^+ back contacts and the solution, and the p^+ contacts are left at open-circuit. The J-V characteristic of the high purity Si/liquid junction is similar to the rectifying diode behavior previously observed on conventional highly doped n-Si/$Me_2Fc^{+/0}$-CH_3OH junctions.[17] The efficiency of this junction is 10.5%, which is comparable to the highest efficiency reported to-date on Si/liquid junctions.[13] This result suggests that the carrier recombination rates at the semiconductor/liquid interface are small, even though the photogenerated charges are driven only by diffusion gradients instead of being separated by an electric field at the semiconductor/liquid interface.

Previous studies of conventional semiconductor/liquid junction solar cells have indicated that when n-Si is in contact with a $Me_2Fc^{+/0}$-CH_3OH solution, the open-circuit potential of the junction is limited by the minority carrier (hole) recombination in the bulk of the semiconductor:[13]

$$V_{oc} = \frac{kT}{q} \ln\left(\frac{J_{ph} L_p N_d}{q D_p n_i^2}\right) \tag{1}$$

where k is the Boltzmann constant, T is the temperature at 297 K, q is the elementary charge, J_{ph} is the light limited current, L_p is the hole diffusion length, D_p is the diffusion coefficient of the minority carriers (12 cm^2-s^{-1}),[31,32] and n_i is the intrinsic carrier concentration, n_i=1.45x10^{10} cm^{-3}. For our high purity n-Si electrode with a dopant concentration of 3 x 10^{13} cm^{-3}, the calculated value of V_{oc} would be 430 mV at a light limiting current (J_{sc}) of 22 mA-cm^{-2}, assuming the sample thickness of ≈100 μm as the diffusion length of the high purity sample. The observation of V_{oc,n^+} values significantly in excess of this theoretical upper limit confirms that the specimens were being operated under high level injection conditions. Essentially, the sample is "photodoped," so that N_d measured in the dark is significantly smaller than N_d measured under illumination. It should be noted that this "photo-doping" process creates equal numbers of electrons and holes in the semiconductor; therefore, both electrons and holes are the majority carriers in the high purity Si sample, which is unique to the high purity Si/liquid junctions.

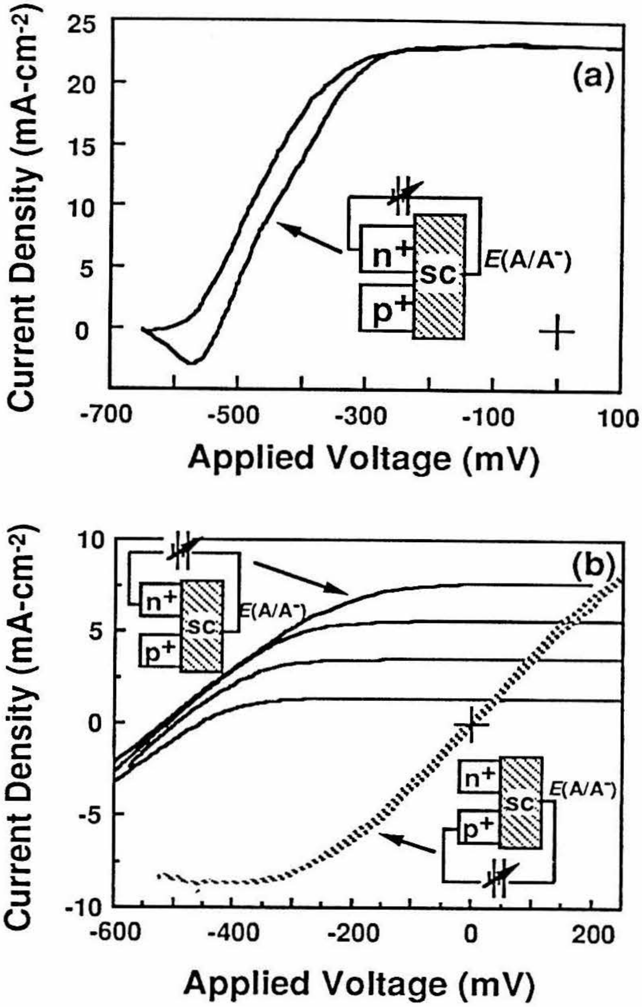

Figure 2. Photocurrent density-voltage (J-V) properties (at 50 mV-s^{-1} scan rate) of Si/Me$_2$Fc$^{+/0}$ junctions. (a) The J-V property of the Si/CH$_3$OH-144 mM Me$_2$Fc-1.5 mM Me$_2$FcBF$_4$-1.0 M LiClO$_4$ (*E*(A/A$^-$)=96 mV vs. SCE) contact, under 69 mW-cm^{-2} of ELH-type W-halogen illumination. The illuminated area of the electrode was 1.17 cm^2. The measurement was performed using a three-electrode potentiostatic arrangement, with n$^+$ contacts as the working electrode, a Pt wire placed in a Luggin capillary containing the redox solution acting as the reference electrode and a Pt foil as the counterelectrode. Such a system has been shown to underestimate the efficiency of actual two-electrode cells under sunlight due to uncompensated ohmic resistance and concentration polarization losses in the potentiostatic configuration.[12] Nevertheless, the efficiency of this photoelectrode was 10.5%, with J_{sc}=22.4 mA-cm^{-2} and V_{oc}=582 mV. (b) The J-V properties of the Si/CH$_3$OH-25 mM Me$_2$Fc-25 mM Me$_2$FcBF$_4$-1.0 M LiClO$_4$ (*E*(A/A$^-$)=203 mV vs. SCE) contact at various illumination levels. The solid lines are the J-V collected when the n$^+$ points were biased vs. the solution. The dashed line is the J-V obtained when the p$^+$ points were biased *vs.* the solution potential. At various light intensities, the J-V behaviors at the p$^+$ contacts are identical.

Figure 2b displays the J-V curves of Si/CH_3OH-$Me_2Fc^{+/0}$ contacts when the n^+ or the p^+ points are biased potentiostatically relative to the solution redox potential, *E*(A/A$^-$), at various light intensities. When the n^+ points are biased, lower J_{sc} values produce lower $V_{oc,n+}$ values, with the plot of $\ln(J_{sc})$ *vs.* $V_{oc,n+}$ providing a diode quality factor of 1.5. J-V curves obtained when the p^+ points are biased relative to the solution exhibit significantly different behavior than the n^+ points. No rectification is observed at the p^+ points, and no significant photovoltage is measured. Under illumination levels that were capable of providing photocurrents from 1 mA-cm^{-2} to 10 mA-cm^{-2} at the n^+ points (solid lines in Fig. 2b), the J-V behaviors at the p^+ points were identical, with the cathodic current being independent of the photolimiting currents. These behaviors are essentially identical to those observed for deliberately doped p-Si samples in contact with CH_3OH-$Me_2Fc^{+/0}$ and could be explained by charge transfer processes at the valence band of the semiconductor.[33] Because the $Me_2Fc^{+/0}$-CH_3OH solution redox potential is very close to the valence band energy of the Si, electrons in the valence band could react with the Me_2Fc species in the solution, which is equivalent to the injection of holes from the solution into the valence band of Si. These holes are then collected at the back p^+ contacts, and the hole flux is not limited by the number of photogenerated carriers. The hole injection process is only possible when negligible electric fields exist at the high purity n-Si/liquid interface. Therefore, J-V behavior at the p^+ contacts also demonstrates that the semiconductor/liquid junction was operated under high injection conditions without significant electric field gradients at the junction.

The spectral response of Si/CH_3OH-$Me_2Fc^{+/0}$ contacts was obtained under high level injection conditions through use of monochromatic laser illumination at several photon energies above the bandgap energy of Si. Table I presents the external quantum yield data as a function of wavelength for a representative Si/$Me_2Fc^{+/0}$ contact. The decline in external quantum yield at short wavelengths is due to solution absorption, not to recombination at the solid/liquid contact. This behavior is similar to that observed for n-Si/CH_3OH-$Me_2Fc^{+/0}$ contacts operated under low level injection.[17] These data indicate that the high quantum yields for charge separation are maintained even under high level injection in the absence of significant electric fields at the solid/liquid contact.

Table I. The carrier collection yield (external quantum yield) measured at a Si/CH_3OH-58 mM Me_2Fc-2 mM Me_2FcBF_4-1.0 M $LiClO_4$ contact and Si/20% CH_3OH-80% THF (by volume)-24 mM $Me_{10}Fc$-17 mM $Me_{10}FcBF_4$-0.54 M $LiClO_4$ contact.

Solution		1020 nm	980 nm	940 nm	880 nm	820 nm	760 nm	514.5 nm	457.9 nm
$Me_2Fc^{+/0}$	low[a]	0.49	0.56	0.71	0.67	0.72	0.80	0.42	0.23
	high[b]			0.83	0.75	0.93	0.74		
$Me_{10}Fc^{+/0}$	n[c]	0.55	0.5	0.91	0.72	0.23	0.11	0.56	0.31
	p[d]	0.30	0.29	0.37	0.19	0.036	0.013	0.066	0.021

The solution potential was 130 mV *vs.* SCE for the $Me_2Fc^{+/0}$ solution, and -7 mV for the $Me_{10}Fc^{+/0}$ solution. The $Me_2Fc^{+/0}$ solution absorbed strongly at 400 to 500 nm and 600 to 750 nm range, and the $Me_{10}Fc^{+/0}$ solution absorbed strongly below 500 nm and between 700 and 850 nm. The low quantum yields at these wavelengths were due to the strong absorption of the solutions. (a) The quantum yield was measured at short-circuit current density levels between 1 mA to 10 mA. (b) The quantum yield was measured at light intensities enough to provide short-circuit current densities higher than 10 mA (typically around 12 mA). (c) The current was measured at the n^+ contact points at 400 mV positive of the solution potential. (d) The current was measured at the p^+ contact points at -400 mV negative of the solution potential. Because of the limits of the solubility of $Me_{10}Fc^{+/0}$ in the CH_3OH-THF solution, the photocurrents were controlled at less than 5 mA, so they would not exceed the mass transport limited current.

2. *Steady-state current density vs. voltage (J-V) properties of Si/CH_3OH-decamethylferrocene ($Me_{10}Fc^{+/0}$) and Si/CH_3OH-$MV^{2+/+\cdot}$ contacts:*

Figures 3 and 4 show the J-V data at n^+ and p^+ points for two other redox couples. These reagents possess more negative redox potentials than $Me_2Fc^{+/0}$, and are therefore expected to result in smaller photovoltages at the n^+-points. In fact, prior to the experiments, it was not clear whether, in the presence of significant concentrations of both forms of the redox couple, substantial charge carrier separation could be obtained (because of the possibility of effective recombination due to faradaic capture of both electrons and holes at the solid/liquid contact).

When the electrical lead was connected to the n^+ points, and these points were biased to potentials positive of V_{oc,n^+}, an anodic photocurrent was observed. When the lead to the n^+ points was disconnected and potential control was established at the p^+ points, with a negative bias relative to V_{oc,p^+}, the photocurrent changed sign, and the sample displayed cathodic photocurrents. The photovoltages at n^+ points for Si/CH_3OH-$Me_{10}Fc^{+/0}$ and Si/CH_3OH-$MV^{2+/+}$ contacts were smaller than those of Si/CH_3OH-$Me_2Fc^{+/0}$ contacts, while V_{oc,p^+} values increased monotonically as $E(A/A^-)$ decreased.

This indicates that recombination is more significant for Si/CH_3OH-$Me_{10}Fc^{+/0}$ and Si/CH_3OH-$MV^{2+/+\cdot}$ contacts than for Si/CH_3OH-$Me_2Fc^{+/0}$ contacts. This is expected from the Shockley-Read-Hall expression, in which recombination centers with energies near mid-gap are more effective at inducing steady-state carrier recombination than centers with energies closer to the band edge positions.

The spectral response characteristics of one of the Si/$Me_{10}Fc^{+/0}$ junctions is summarized in Table I. The external quantum yields are above 70% at wavelengths where solution absorption is weak. These results suggest that carriers can be collected efficiently even when electric field gradients are not present at the semiconductor/liquid interface. A smaller quantum yield is observed at the p^+ contact points, and suggests that the recombination rate is significantly higher as the photogenerated holes are collected from the back contacts. This asymmetry in limiting currents at the n^+ and p^+ back contacts is wavelength dependent, and is not consistent for various electrodes with similar design. It remains unclear if this process is due to poor contact junctions between the p^+ region and the high purity Si, or is the result of slow kinetics in electron transfer at the Si/liquid interface.

The behavior of Si/CH_3OH-$Me_{10}Fc^{+/0}$ and Si/CH_3OH-$MV^{2+/+}$ contacts is not consistent with the presence of significant drift-induced charge separation. Since the back of the sample was separated by $>10^3$ Debye lengths from the solid/liquid contact, the electric field at the solid/liquid interface could not have been affected by the nature of the electrical connections to the points at the back of the specimen. Any drift-induced carrier motion near the solid/liquid contact would therefore have been independent of the contact geometry and bias conditions at the back of the sample. The ability to completely reverse the direction of carrier movement, while maintaining a high quantum yield for charge separation and collection, thus provides strong evidence that diffusion-driven concentration gradients are the dominant charge separation process for these solid/liquid contacts.

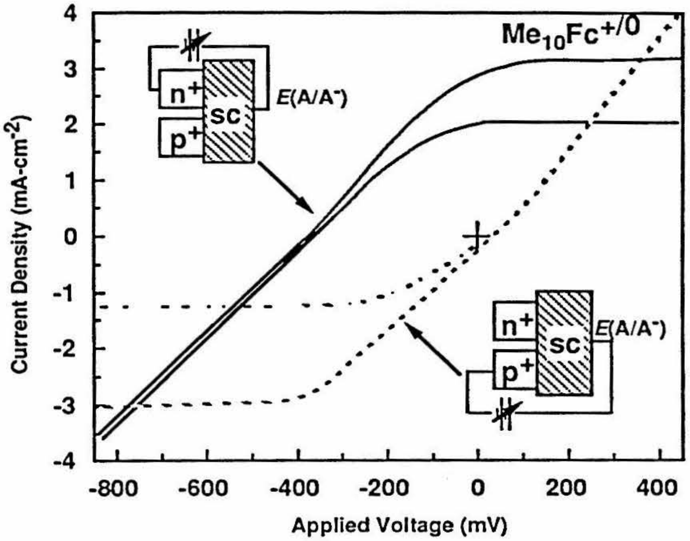

Figure 3. J-V properties of Si/20% CH_3OH-80% THF (by volume)-23 mM $Me_{10}Fc$-14 mM $Me_{10}FcBF_4$-0.55 mM $LiClO_4$ contact. The solution potential was -3 mV *vs.* SCE.

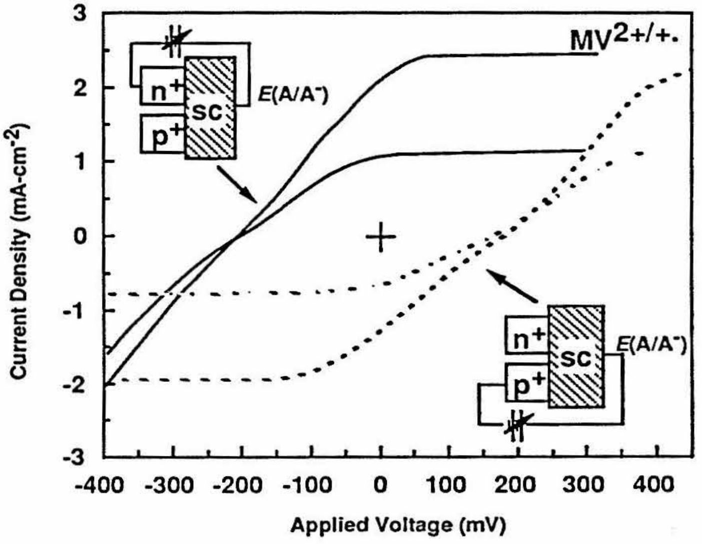

Figure 4. J-V properties of Si/CH_3OH-16 mM $MV^{+\cdot}$-23 mM $MVCl_2$-0.9 M LiCl contact. The solution potential was -419 mV *vs.* SCE.

3. Steady-state current density vs. voltage (J-V) properties of $Si/CH_3OH\text{-}Co(Cp)_2^{+/0}$ *contacts:*

In order to probe whether the V_{oc} values of $Si/Me_2Fc^{+/0}$ contacts are specific to this solid/liquid junction, J-V properties of $Si/CH_3OH\text{-}Co(Cp)_2^{+/0}$ contacts were also investigated. The redox potential of $Co(Cp)_2^{+/0}$ is near the conduction band edge of the Si. J-V characteristics should be opposite of those observed at a $Si/Me_2Fc^{+/0}$ junction. Figure 5 displays the J-V behavior for $Si/CH_3OH\text{-}Co(Cp)_2^{+/0}$ contacts at a variety of light intensities. Collection of electrons at the n^+ points leads to nonrectifying behavior, but collection of holes at the p^+ points leads to large $V_{oc,p+}$ values and significant cathodic photocurrents. This clearly illustrates that, although the direction of carrier collection is controlled by the back contacts, the free energy available from the photoexcited carriers is primarily determined by the properties at the Si/CH_3OH contact.

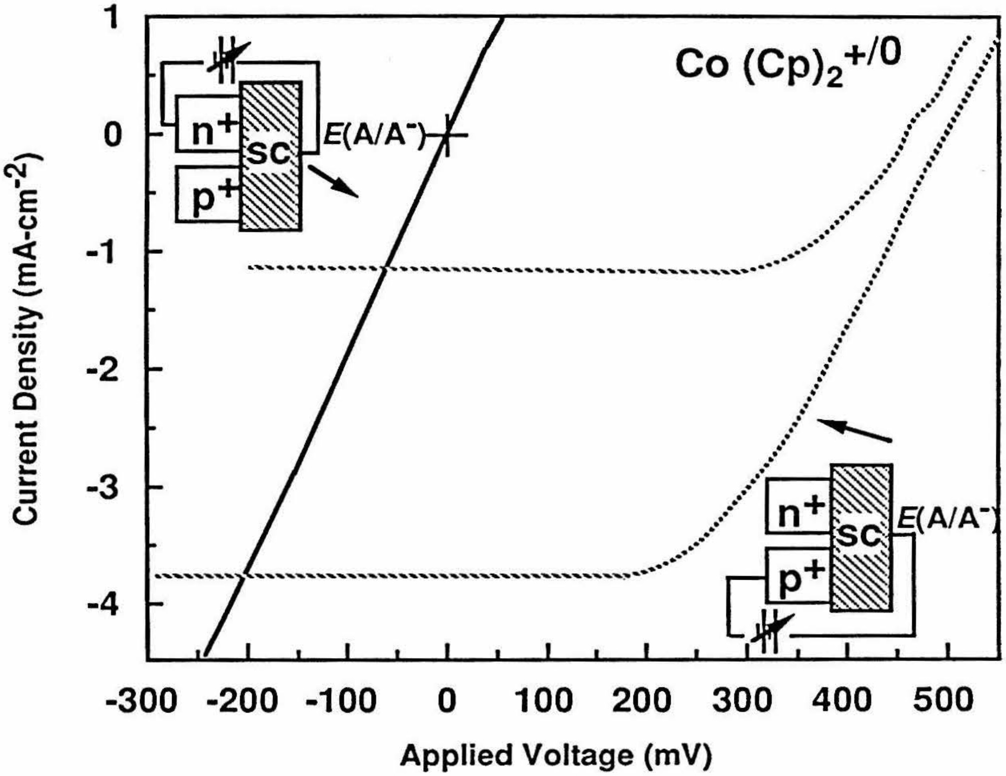

Figure 5. J-V properties of Si/CH_3OH-8.5 mM $Co(Cp)_2$-38 mM $Co(Cp)_2Cl$-1.0 M LiCl contact. The solution potential was -917 mV *vs.* SCE. The solid line is the J-V collected when the n^+ points were biased vs. the solution. The dashed lines are the J-V obtained when the p^+ points were biased *vs.* the solution potential. At various light intensities, the J-V behaviors at the n^+ contacts are identical.

IV. DISCUSSION

The open-circuit potentials measured at the n^+ and p^+ contact points relative to the various solution potentials represent the quasi-Fermi level positions of electrons and holes in these solutions. The quasi-Fermi level position relative to the solution potential is a measure of the kinetics of charge transfer process at the semiconductor/liquid interface.[25] In the $Me_2Fc^{+/0}$ solution, the quasi-Fermi level of holes is at the same potential as the solution potential, indicating rapid hole transfer at the semiconductor/liquid junction. At illumination levels that are capable of providing 3.5 mA/cm^2 of photocurrent, the quasi-Fermi level of electrons is about 526 ± 30 mV negative of the solution electrochemical potential (Fig. 6). The high photovoltage developed for the electrons suggests slow electron transfer from the semiconductor to the solution. Although under the high injection conditions negligible electric fields exist at the semiconductor/liquid interface, and charge separation can not be achieved through drift, the solution selectivity toward specific carriers (holes at the Si/$Me_2Fc^{+/0}$ contact) has achieved efficient charge separation with minim recombination (the specific recombination velocities are evaluated in Part II).

The slow electron transfer and fast hole reaction at the Si/$Me_2Fc^{+/0}$ contact can not be explained by the conventional theory on charge transfers. According to the position of the solution potential in the semiconductor (Fig. 6), the activation energy for the charge transfer process favors the electron transfer from the conduction band to solution over hole transfer from the valence band to solution,[34,35] and therefore higher electron transfer rate is expected. However, recent studies of surface conductivity measurements at low resistance Si/$Me_2Fc^{+/0}$ interfaces have demonstrated that an inversion layer exists at the Si surface.[36] An inversion layer in an n-type semiconductor acts as a highly doped p^+ layer, which blocks the transfer of electrons and allows tunneling of holes. The observation of fast hole transfer rate at the high purity Si/$Me_2Fc^{+/0}$ junction supports the existence of such an inversion layer at the Si surface.

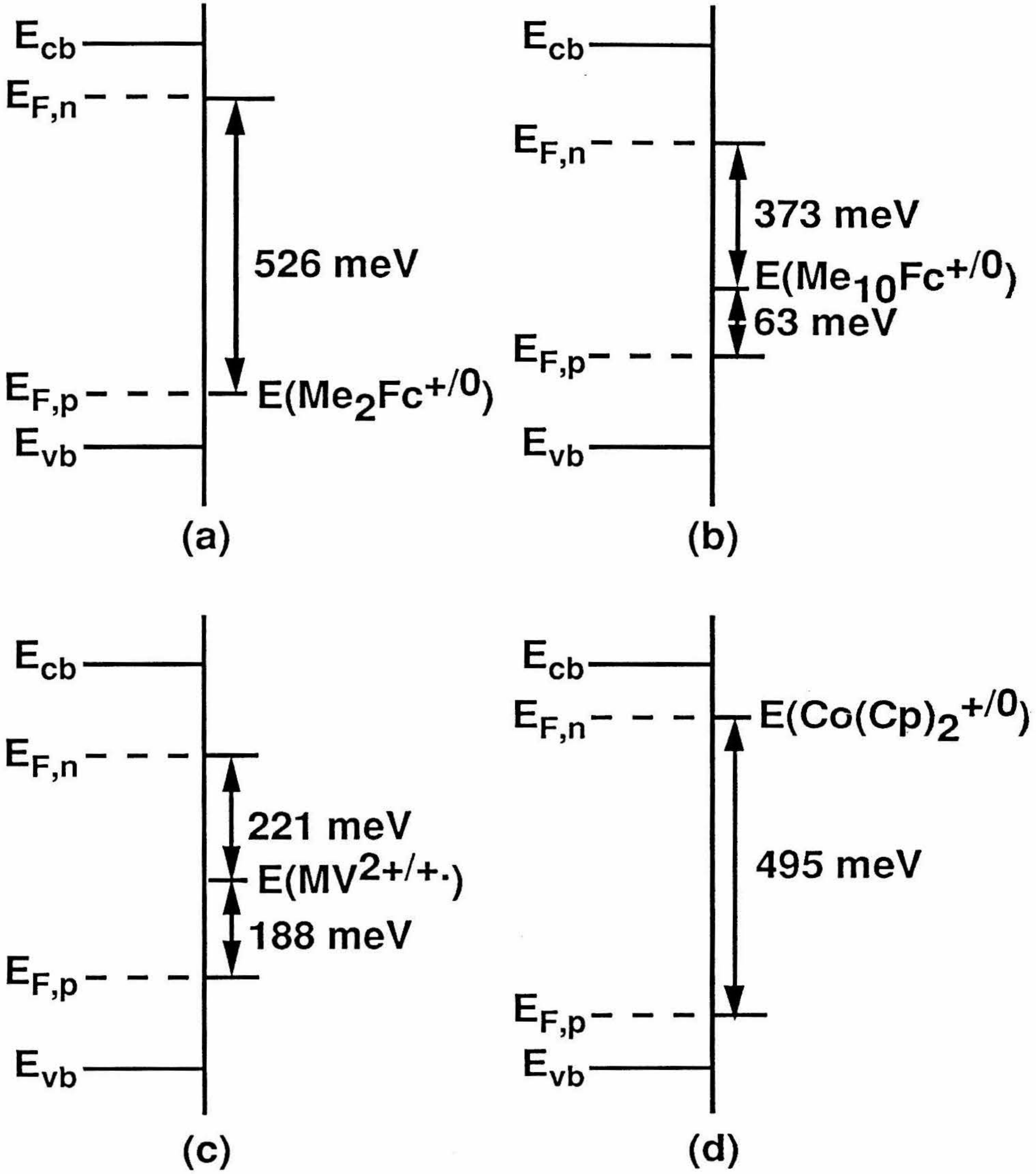

Figure 6. The positions of quasi-Fermi levels of electrons and holes in various solutions, under illumination intensities sufficient to provide 3.5 mA-cm^{-2} of photocurrent.

The quasi-Fermi level positions in the $Co(Cp)_2^{+/0}$ solution are also determined by the charge transfer process occurring at the semiconductor surface (Fig 6). The rapid exchange of electrons at the Si conduction band fixes the quasi-Fermi levels of electrons at the solution potential, and the quasi-Fermi level of holes is 495 ± 30 mV ($J_{sc} \approx 3.5$ mA-cm^{-2}) below the solution potential, *i.e.*, the hole transfer is slow. The slow hole transfer rate at the semiconductor/liquid interface minimizes the recombination of electrons and holes at the semiconductor/liquid interface and provides efficient carrier collection at the p^+ points. In $Me_{10}Fc^{+/0}$ and $MV^{2+/+\cdot}$ solutions, the solution potential lies between the quasi-Fermi levels of electrons and holes. The sum of the quasi-Fermi levels ($V_{pn} = V_{oc,\, p^+} + V_{oc,\, n^+}$), which equals the total free energies stored in the photoelectrochemical cells, is about 436 and 409 mV ($J_{sc} \approx 3.5$ mA-cm^{-2}) in $Me_{10}Fc^{+/0}$ and $MV^{+\cdot/2+}$ solutions, respectively. These numbers are smaller than the sum of the potentials measured in $Me_2Fc^{+/0}$ and $Co(Cp)_2^{+/0}$ solutions (526 and 495 mV) under similar illumination intensities. Therefore, the energy storage process is more efficient at the $Si/Me_2Fc^{+/0}$ and $Si/Co(Cp)_2^{+/0}$ junctions, indicating slower recombination rates at these junctions. This variation in recombination rates as a function of the solution potential fully agrees with the Shockley-Read-Hall theory on recombination, which predicts higher recombination rates for trap energies near the middle of the semiconductor bandgap.[37] In Part II of this chapter, these surface recombination processes are discussed in detail.

V. CONCLUSION

We have demonstrated that a high purity semiconductor/liquid junction can provide high energy conversion efficiency even without an electric field to separate the photogenerated carriers at the semiconductor/liquid interface. Carrier separation is achieved by a diffusion gradient across distances over 100 µm. The flow direction of carriers is entirely determined by the choice of back contacts (n^+ or p^+), and therefore the J-V characteristics obtained from the n^+ or the p^+ contacts are different on the same Si sample in the same solution. We have also demonstrated the first simultaneous measurement, to our knowledge, of the quasi-Fermi levels of the electrons and holes at a semiconductor/liquid junction. Our experimental results support the validity of the quasi-Fermi level theory for semiconductor/liquid junctions. The recombination process at the semiconductor/liquid interface varies with the solution potential according the Shockley-Read-Hall theory on recombination. In the next part, we present experimental evidence and modeling studies suggesting that the quasi-Fermi levels are essentially flat across the sample and minimum electric field gradients exist at the semiconductor/liquid interface.

References:

(1) Finklea, H. O. *Semiconductor Electrodes*; Elsevier: New York, 1988; Vol. 55.

(2) Heller, A. *Acc. Chem. Res.* **1981**, *14*, 154.

(3) Lewis, N. S. *Acc. Chem. Res.* **1990**, *23*, 176.

(4) *Homogeneous and Heterogeneous Photocatalysis*; Pelizzetti, E.; Serpone, N., Ed.; D. Reidel: Dordrecht, 1986; Vol. 174, pp 721.

(5) Ollis, D.; Pelizzetti, E.; Serpone, N. In *Photocatalysis: Fundamentals and Applications*; N. Serpone and E. Pelizzetti, Ed.; John Wiley & Sons: New York, 1989; pp 603.

(6) Fox, M. A. In *Photocatalysis and Environment: Trends and Applications*; M. Schiavello, Ed.; Kluwer Academic Publishers: Dordrecht, 1988; Vol. 237; pp 445.

(7) Gärtner, W. W. *Phys. Rev.* **1959**, *116*, 84.

(8) Burk, Jr., A. A.; Johnson, P. B.; Hobson, W. S.; Ellis, A. B. *J. Appl. Phys.* **1986**, *59*, 1621.

(9) Licht, S.; Peramunage, D. *Nature* **1990**, *345*, 330.

(10) O'Regan, B.; Grätzel, M. *Nature* **1991**, *353*, 737.

(11) Gronet, C. M.; Lewis, N. S. *Nature* **1982**, *300*, 733.

(12) Gibbons, J. F.; Cogan, G. W.; Gronet, C. M.; Lewis, N. S. *Appl. Phys. Lett.* **1984**, *45*, 1095.

(13) Rosenbluth, M. L.; Lieber, C. M.; Lewis, N. S. *Appl. Phys. Lett.* **1984**, *45*, 423.

(14) Tufts, B. J.; Abrahams, I. L.; Santangelo, P. G.; Ryba, G. N.; Casagrande, L. G.; Lewis, N. S. *Nature* **1987**, *326*, 861.

(15) Parkinson, B. *Acc. Chem. Res.* **1984**, *17*, 431.

(16) Lewis, N. S.; Rosenbluth, M. L.; Casagrande, L. G.; Tufts, B. J. In *Homogeneous and Heterogeneous Photocatalysis*; E. Pelizzetti and N. Serpone, Ed.; Reidel: Dordrecht, 1986; Vol. 174; pp 343.

(17) Rosenbluth, M. L.; Lewis, N. S. *J. Am. Chem. Soc.* **1986**, *108*, 4689.

(18) Cuevas, A.; Sinton, R. A.; Midkiff, N. E.; Swanson, R. M. *IEEE Trans. Elect. Devices* **1990**, 6.

(19) Swanson, R. M. *Solar Cells* **1986**, *17*, 85.

(20) Feldberg, S. W.; Evenor, M.; Huppert, D.; Gottesfeld, S. *J. Electroanal. Chem.* **1985**, *185*, 209.

(21) Sze, S. M. *The Physics of Semiconductor Devices;* 2nd ed.; Wiley: New York, 1981.

(22) Memming, R. *Electrochmica Acta.* **1980**, *25*, 77.

(23) Nozik, A. J.; Williams, F. *Nature* **1984**, *312*, 21.

(24) Kumar, A.; Santangelo, P. G.; Lewis, N. S. *J. Phys. Chem.* **1992**, *96*, 834.

(25) Reineke, R.; Memming, R. *J. Phys. Chem.* **1992**, *96*, 1317.

(26) Hodes, G.; Howell, I. D. J.; Peter, L. M. *J. Electrochem. Soc.* **1992**, *139*, 3136.

(27) Verlinden, P. J.; Swanson, R. M.; Sinton, R. A.; Crane, R. A.; Tilford, C.; Perkins, J.; Garrison, K. *23rd IEEE Photovoltaic Specialists Conference, Louisville, KY* **1993**, *May*, 58.

(28) Swanson, R. M.; Beckwith, S. K.; Crane, R. A.; Eades, W. D.; Kwark, Y. H.; Sinton, R. A.; Swirhun, S. E. *IEEE Trans. Electron Devices* **1984**, *ED-31*, 661.

(29) King, R. R.; Sinton, R. A.; Swanson, R. M. *Appl. Phys. Lett.* **1989**, *54*, 1460.

(30) Tufts, B. J.; Abrahams, I. L.; Casagrande, L. G.; Lewis, N. S. *J. Phys. Chem.* **1989**, *93*, 3260.

(31) Thurber, W. R.; Mattis, R. L.; Liu, Y. M.; Filliben, J. J. *J. Electrochem. Soc.* **1980**, *127*, 1807.

(32) Thurber, W. R.; Mattis, R. L.; Liu, Y. M.; Filliben, J. J. *J. Electrochem. Soc.* **1980**, *127*, 2291.

(33) Lieber, C. M.; Gronet, C. M.; Lewis, N. S. *Nature* **1984**, *307*, 533.

(34) Gerischer, H. In *Physical Chemistry: An Advanced Treatise*; H. Eyring; D. Henderson and W. Yost, Ed.; Academic: New York, 1970; Vol. 9A; pp 463.

(35) Morrison, S. R. *Electrochemistry at Semiconductor and Oxidized Metal Electrodes*; Plenum: New York, 1980.

(36) Laibinis, P. E.; Stanton, C. E.; Lewis, N. S. *J. Phys. Chem.* **1994**, *in press*.

(37) Many, A.; Goldstein, Y.; Grover, N. B. *Semiconductor Surfaces*; North-Holland Publishing Co.: New York, 1965, pp 262.

Part II. Measurements and Modeling of the Semiconductor Quasi-Fermi Levels Under High Level Illumination Conditions

I. INTRODUCTION

The preceding section described the use of a novel photoelectrode geometry to achieve efficient carrier separation through diffusion-driven concentration gradients. In this configuration, the implanted n^+ and p^+ point contacts at the back of the Si samples have allowed simultaneous measurements of the apparent electrochemical potentials (quasi-Fermi levels) for electrons and holes in a semiconductor photoelectrode. These measurements, performed under various steady-state illumination conditions, have yielded valuable insight into the behavior of the theoretically important quasi-Fermi level positions. Experimental data have been collected on the behavior of the electron ($\mathbf{E}_{f,n}$) and hole ($\mathbf{E}_{f,p}$) quasi-Fermi levels for four redox couples (with redox potentials spanning over one Volt), whose electrical junction characteristics ranged from rectifying to ohmic. These data are in excellent agreement with the predictions of theoretical models for quasi-Fermi levels under steady-state conditions.[1,2]

One important quantitative issue involved in interpreting these experimental data is the degree to which, under high injection conditions, the quasi-Fermi level positions measured at the back point contacts of the sample approximate the positions of the quasi-Fermi levels at the semiconductor/liquid interface. These latter values are the ones of direct theoretical interest, and are those required to describe the interfacial charge carrier kinetics at solid/liquid contacts. Although, to our knowledge, no previous direct experimental data exists on the quasi-Fermi level values at semiconductor/liquid interfaces,[3,4] the desired quantities could, in principle, be determined through strategies that exploit near-surface conductance data.[5] However, the surface conductance approach would require fabrication of a rather complex lithographic structure (to measure both electron and hole concentrations simultaneously), and would introduce other contact and recombination regions into the device design that must be considered during a full analysis of the system.

An alternative approach, described herein, is to develop a functional model of the relevant kinetic processes for the semiconductor/liquid contact of interest. Knowledge of carrier transport, generation, and recombination in the photoelectrode would provide a description of the electron and hole concentration profiles ($n(x,t)$ and $p(x,t)$, respectively) as a function of time (t) and distance (x) from the solid/liquid contact. According to the definitions of quasi-Fermi levels,[6] such a description of the carrier concentration profiles would allow explicit computation of the difference in quasi-Fermi level positions between the front (x=0) and back (x=d) surfaces under various experimental conditions:

$$\mathbf{E}_{f,n}(0,t) - \mathbf{E}_{f,n}(d,t) = \frac{kT}{q}\ln\left[\frac{n(d,t)}{n(0,t)}\right] \tag{1}$$

$$\mathbf{E}_{f,p}(0,t) - \mathbf{E}_{f,p}(d,t) = \frac{kT}{q}\ln\left[\frac{p(0,t)}{p(d,t)}\right] \tag{2}$$

In these equations, k is the Boltzmann constant, T is the temperature, q is the elementary charge and d is the sample thickness. The purpose of this work was to develop, and experimentally validate, such a model for the operating conditions of the photoelectrode samples discussed in Part I (the preceding paper) of this series.

Several approaches were pursued to achieve the goals presented above. Real-time measurements of the photovoltage rise and decay at the back of the sample were performed in response to a variety of spatial and temporal carrier generation impulses (Fig. 1). The functional form of the rising portion of the photovoltage signal is sensitive to charge transport processes,[7,8] and therefore could validate experimentally the hypothesis that charge transport in these samples under high injection is primarily driven by diffusion, as opposed to drift. The decay of the photovoltage signal back to its equilibrium value yields additional information concerning the surface recombination velocity, S_f, of the various Si/CH_3OH-redox couple contacts. These data provide a needed boundary condition for modeling the carrier concentration dynamics, and allow quantification of the difference between the quasi-Fermi levels at the back and front surfaces of the samples at all times of experimental interest. Analytical modeling has also been performed to compute the gradients in the quasi-Fermi levels for samples operated under steady-state, open-circuit, high injection conditions. This analysis did not require any information from the transient experiments or modeling thereof, but served to validate quantitatively the values determined from the transient experiments and to lend confidence to the full description of the carrier dynamics in this system.

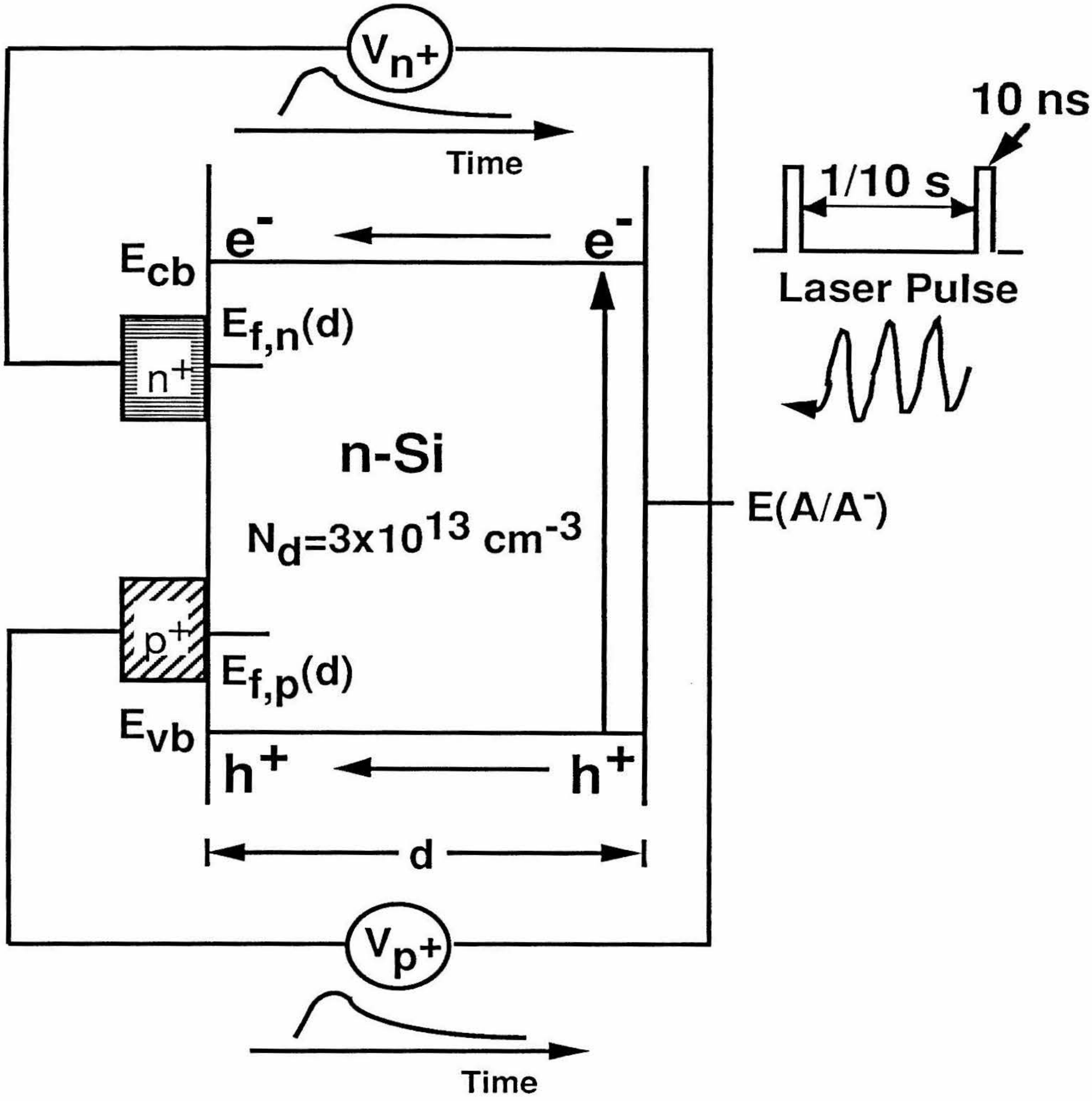

Figure 1. A schematic representation of the real-time photovoltage rise and decay measurements at a high purity Si/liquid junction. E_{cb} and E_{vb} represent the conduction band edge and valence band edge of the semiconductor, respectively. E(A/A$^-$) is the solution electrochemical potential. The wavelength of the laser pulse can be adjusted to provide the desired carrier generation profiles in the semiconductor. The photovoltages measured at the n^+ and p^+ contact points directly reflect the quasi-Fermi level positions of electrons and holes at the back of the sample, $E_{f,n}(d)=qV_{n+}$ and $E_{f,p}(d)=qV_{p+}$. The rise and decay of the quasi-Fermi levels are functions of the carrier transport, generation and recombination processes.

II. EXPERIMENTAL

The sample and solution preparation procedures are the same as those described in Part I of this chapter.

The transient photovoltage measurements were performed using three channels of a Tektronix 11A34 amplifier (300 MHz bandwidth) in a Textronix DSA600 digital oscilloscope. Channels 1 and 2 were connected to the p^+ and n^+ point contacts, respectively. Channel 3 was connected to a Pt wire that was immersed in the solution which served as the reference electrode. The point contacts were effectively open-circuited from other contacts by imposing 1 MΩ input impedances onto channels 1 and 2, with the reference Pt wire grounded by selecting a 50 Ω input impedance for channel 3. Signals were simultaneously acquired at all three channels, and collected as [(channel 1 - channel 3) - (channel 2 - channel 3)] with signal averaging, before being transferred by GPIB interface to a PC for storage.

Illumination was provided by a Quanta-Ray DCR Nd:YAG laser, with a pulse width at approximately 10 ns FWHM for both the fundamental (1064 nm) and frequency doubled (532 nm) outputs. The laser beam was expanded to illuminate the entire electrode area (≈ 1.1 cm^2), and the beam intensity was varied using either the Q-switch delay control and/or neutral density filters. Approximate beam powers were measured using a joule meter that had been masked to expose an area equal to that of the electrode.

The BASIC program used in the digital simulation was a modified version of the finite-difference program originally written by N. S. Lewis. The original program has been described in detail by Ryba.[9] Carrier concentrations as a function of time and distance were stored in separate data files. A DOS compatible Macintosh Quadra 610 was used to run the simulation.

III. RESULTS

1. Time-Resolved Photovoltage Studies: Measurement and Simulation of the Time-Dependent Carrier Concentration Profiles at Si/CH_3OH-$Me_2Fc^{+/0}$ Contacts:

Figures 2a and 2b depict the transient photovoltage signals that were observed after injection of charge into a Si photoelectrode in contact with CH_3OH-$Me_2Fc^{+/0}$. The light source was a 532 nm, 10 ns Nd:YAG laser pulse. The difference in photovoltages measured between the n^+ and p^+ contact points relative to the solution potential (V_{n^+} and V_{p^+} respectively), $V_{pn} = V_{p^+} - V_{n^+}$, is plotted against time. According to the definitions of quasi-Fermi levels,[6] the value of $V_{pn}(t)$ is proportional to the product of the electron and hole concentrations at the back surface of the sample (n(d,t) and p(d,t) respectively):[10]

$$n(d,t)p(d,t) = n_i^2 \exp\left[\frac{qV_{pn}(t)}{kT}\right] \tag{3}$$

where n_i is the intrinsic carrier concentration. Under high injection conditions, n(d,t) = p(d,t), yielding the following expression:

$$n(d,t) = p(d,t) = n_i \exp\left[\frac{qV_{pn}(t)}{2kT}\right] \tag{4}$$

Thus, using Eq. 4, the transient photovoltage data of Figs. 2a and 2b could be readily converted into the desired time-dependent carrier concentrations at the back of the sample (Figs. 2c and 2d).

The functional form of the concentration rise data contained information on the carrier transport dynamics, while the signal decay time allowed calculation of the surface recombination velocity, S_f. As shown in Fig. 2c, the carrier concentration reached an approximately constant value after 2 μs, demonstrating that recombination occurred at a slower rate than carrier diffusion. In other words, the photogenerated carries first diffused throughout the sample thickness, d, before being depleted appreciably through recombination. The carrier concentration, p (p=n under the high injection condition), becomes independent of distance in the sample. Under such conditions, the carrier concentration decay time can be related to the surface recombination velocity (S_f) by reference to the behavior of the fundamental filament decay mode:[11,12]

$$-\frac{dp(t)}{dt} = \frac{p(t)}{\tau_f} = p(t)\frac{S_f}{d} \tag{5}$$

$$\ln(p(t)) = \ln(p_o) - \frac{S_f}{d}t \tag{6}$$

where τ_f is the carrier decay time constant known as the filament lifetime, and p_o is the carrier concentration after the initial rise following carrier injection at the front surface. The slope of a semi-log plot of p *vs.* t (p(t)=p(d,t) and can be calculated from V_{pn} using Eq. 4) should yield S_f, if the sample thickness (d) is known.

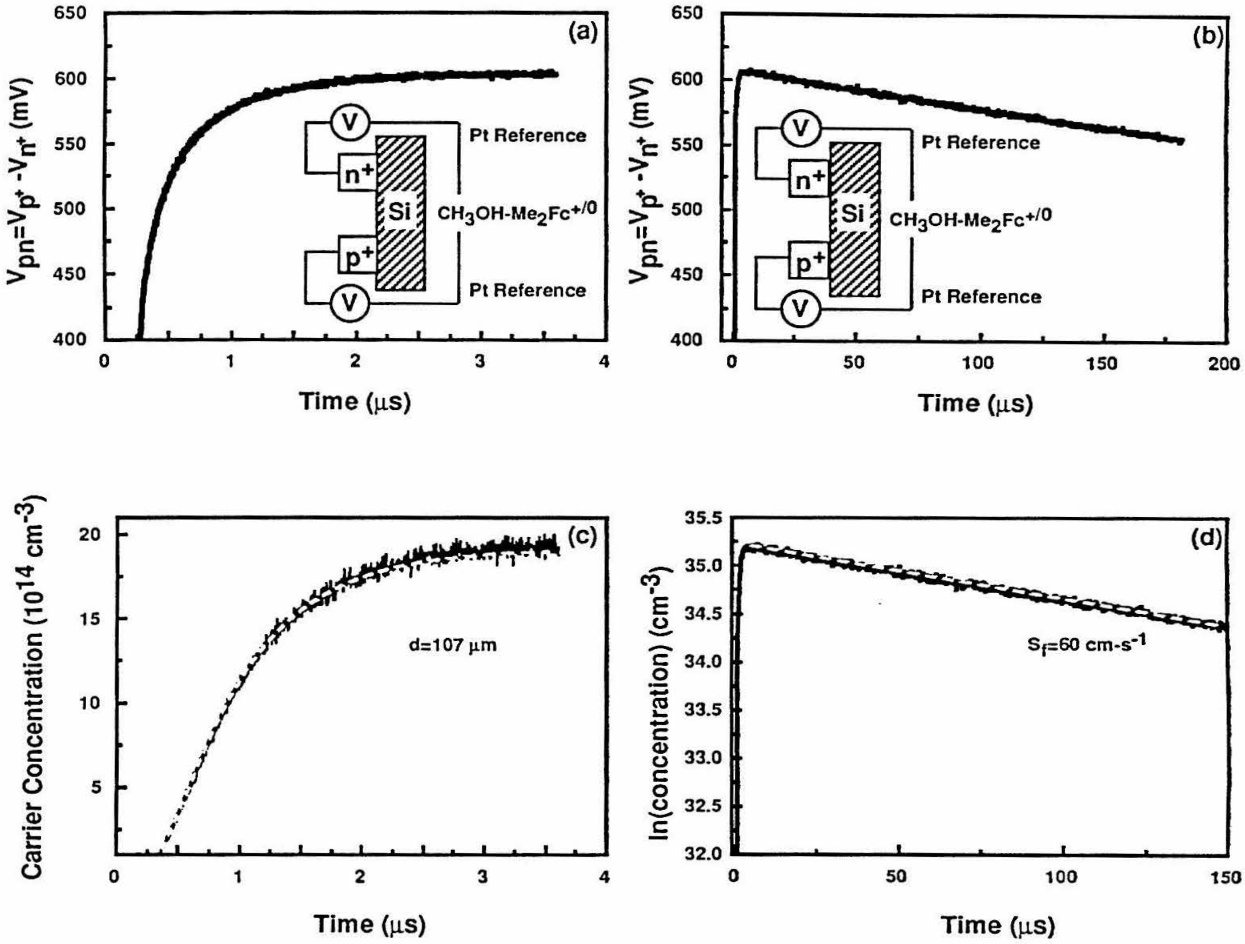

Figure 2. Photovoltage rise and decay (V_{pn}) measured at the Si/CH$_3$OH-3.9 mM Me$_2$Fc-0.6 mM Me$_2$FcBF$_4$-1.0 M LiClO$_4$ contact under 532 nm pulsed laser illumination ($\approx 2 \times 10^{-5}$ J-cm^{-2}). The solid line in (c) represents the rise signal of the carrier concentration at the back of the sample calculated from the V_{pn} values presented in (a) using Eq. 4. The dashed line is the fit generated from the diffusional model at Eqs. 7-11. The thickness of the sample, d, obtained from the fit was 107 μm. The value of I_o' was 2.05 x10^{13} cm^{-2}. In (d), a semi-log plot of the carrier concentration *vs.* time is presented (solid line). The dashed line represents the linear fit to the decay portion of the concentration profile. The slope of this line corresponded to a surface recombination velocity of 60 cm-s^{-1} (Eq. 6).

Because the bulk lifetime of these samples was > 1 ms,[13] and because the photovoltage decay time constant (τ_f) for these same structures exceeded 250 μs in air when the front surface of the sample was protected with a passivation layer to minimize surface recombination, all decays observed for semiconductor/liquid junctions (after removal of the front surface passivation layer with a chemical etch) with τ_f<250 μs were reliably ascribed to front surface recombination/charge transfer processes at the solid/liquid contact. Analysis of the carrier concentration decay data (such as Fig. 2d) at various illumination levels using Eq. 6 yielded $S_f \approx (1.0 \pm 0.4) \times 10^2$ cm-s^{-1} ($\tau_f \approx 1.0 \times 10^2$ μs) for the Si/CH_3OH-$Me_2Fc^{+/0}$ contact. This value is in good agreement with the value of S_f=40 cm-s^{-1} determined previously for this system using rf and microwave conductivity decay methods.[14]

The low measured surface recombination rate and relatively large τ_f suggested that the carrier transport dynamics could be modeled during the 4 μs signal rise time by assuming negligible recombination in this regime (Fig. 2c). If the carrier transport process is dominated by diffusion, carriers generated by an initial illumination pulse at the Si front surface would diffuse towards the back of the semiconductor as given by Eq. 7:

$$\frac{\partial p(x,t)}{\partial t} = D\frac{\partial^2 p(x,t)}{\partial x^2} \tag{7}$$

Here, p(x,t) represents the photogenerated carrier concentration (under high injection conditions, p(x,t)=n(x,t)) and D is the ambipolar diffusion coefficient of electrons and holes in Si (D=18 cm^2-s^{-1}).[13,15-17]

Because the 10 ns laser pulse used in our experiments was much shorter than the time scale of interest (>1 μs), a delta function could be used to model the initial photogeneration process as a function of time:

$$p(x,t) = \begin{cases} f(x) \text{ at } t = 0 \\ 0 \text{ at } t > 0 \end{cases} \tag{8}$$

where f(x) is the distance dependent carrier profile immediately after the absorption of light. Solving Eq. 7 with the initial condition of Eq. 8 yields following equation:[18]

$$p(x,t) = \frac{1}{d}\int_0^d f(x')dx' + \frac{2}{d}\sum_{i=1}^{\infty} \exp(-\frac{i^2\pi^2 Dt}{d^2})\cos\frac{i\pi x}{d}\int_0^d f(x')\cos\frac{i\pi x'}{d}dx' \tag{9}$$
[19]

The absorption coefficient of Si for 532 nm illumination is about 8240 cm^{-1},[20] indicating that almost all of the photogenerated carriers were created within 1 μm of the semiconductor surface. Since the overall sample thickness was >100 μm, the initial carrier distribution function (f(x)) could be treated as a delta function with respect to distance:

$$f(x) = \begin{cases} f(0) \text{ at } x = 0 \\ 0 \text{ at } x > 0 \end{cases} \tag{10}$$

where x=0 is the semiconductor/liquid interface. Using Eqs. 9 and 10, a simplified expression for the carrier concentration at the back contacts is then obtained.

$$p(d,t) = \frac{I_o'}{d} + \frac{2I_o'}{d}\sum_{i=1}^{\infty}(-1)^i \exp(-\frac{i^2\pi^2 Dt}{d^2}) \tag{11}$$

where I_o' (cm^{-2}) is the total number of carriers generated by the laser pulse at the semiconductor surface, and I_o'/d, therefore, represents the number of photogenerated carriers averaged over the entire semiconductor sample.

This analytical solution was used to fit the carrier concentration rise profiles in Fig. 2c. As solution absorption and sample reflectivity precluded an accurate calculation of the actual number of photons absorbed by the Si, the value of I_o' was calculated from the maximum carrier concentration reached after 3 μs, $p(d,t>3\ \mu s) \approx p(d,\infty) = I_o'/d$ (zero carrier recombination is assumed in Eqs. 7-11). The only adjustable parameter used in the fitting procedure was the sample thickness, d. The d value of 107 μm obtained from the fit agreed well with the calculated sample thickness of 113±5 μm resulting from the etchant-induced removal of 7 μm from the 120±5 μm thick sample (see Part I for detailed description of the etching process). The excellent fit of Eq. 11 to the carrier concentration rise profile (Fig. 2c) demonstrated that, under high injection conditions, negligible electric fields existed at the semiconductor/liquid interface and diffusion was the predominate carrier transport process in the semiconductor. Furthermore, the quality of the fit justified the assumption, used in Eqs. 7-11, that recombination occurs at a much slower rate than diffusion and could be neglected in the initial carrier concentration rise at the back of the sample.

Photovoltage data were also obtained under high injection conditions using 1064 nm illumination. Because the absorption coefficient of Si at 1064 nm is only about 10.5 cm^{-1},[20] carriers were generated nearly uniformly within the 107 μm thick semiconductor. Under these excitation conditions, the rise time of the concentration profile was much shorter (Fig. 3a) and was limited by the laser pulse width. However, the carrier decay time (Fig. 3b) and the calculated S_f value were the same as those obtained using 532 nm illumination. This observation further supports the hypothesis that the carrier recombination occurred on a time scale much longer than that of the initial diffusion process.

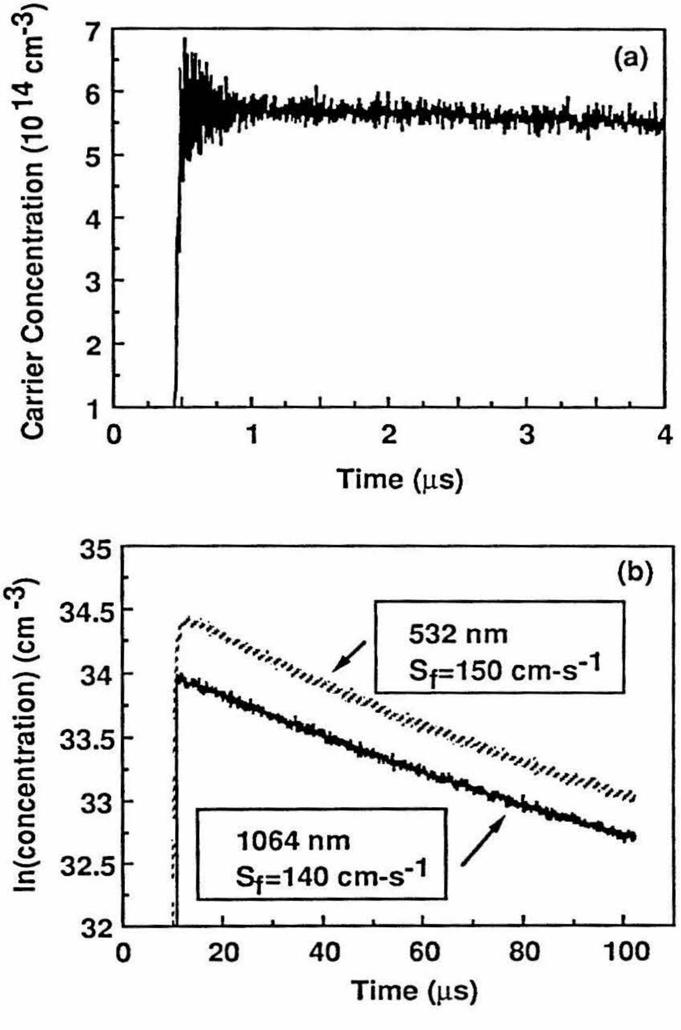

Figure 3. Measurements of the carrier concentration rise (a) and decay (b) (calculated from V_{pn}) at a Si/CH_3OH-25 mM Me_2Fc-25 mM Me_2FcBF_4-1.0 M $LiClO_4$ junction under 1064 nm pulsed laser illumination ($\approx 3\times10^{-7}$ J-cm^{-2}). For comparison, the decay signal obtained at the same semiconductor/liquid junction under 532nm illumination ($\approx 2\times10^{-6}$ J-cm^{-2}) is also presented (dashed line). The corresponding S_f values were obtained from linear fits to the decay portions of these data (Eq. 6).

A more complete description of the photovoltage transient signal, including both the rise and decay kinetics, required incorporation of transport and generation as well as recombination processes. To achieve this, the following diffusion equations were solved using digital simulation procedures.[9]

$$\frac{\partial n(x,t)}{\partial t} = D\frac{\partial^2 n(x,t)}{\partial x^2} \tag{12}$$

$$\frac{\partial p(x,t)}{\partial t} = D\frac{\partial^2 p(x,t)}{\partial x^2} \tag{13}$$

In the simulation, the light pulse was treated as a delta function with respect to time (Eq. 8), but the actual penetration depth was used in calculating the initial carrier distribution profile. Since the front surface recombination dominated the recombination process in the semiconductor/liquid junction, the back surface recombination velocity was assumed to be zero, *i.e.*, $S(0,t)=S_f$, and $S(d,t)=0$.

The digital simulation incorporated generation, diffusion and surface recombination in modeling the carrier concentration rise and decay, and therefore described the carrier dynamics more accurately than the analytical solutions mentioned above. Input variables such as D, d, the photon penetration depth and the injection level were known independently, so S_f, which dominated the form of the decay (*vide supra*), was the only adjustable parameter in the modeling. For a given value of S_f, the simulation directly yielded the carrier concentration profiles as a function of time. The dashed curves in Figs. 4a and b indicated that the agreement between theory and experiment for $Si/Me_2Fc^{+/0}$ contacts with $S_f=60$ cm-s^{-1} was outstanding over the entire time range. The agreement between this S_f value and the S_f obtained from Fig. 2d supported the earlier assignment of the concentration decay for the $Si/Me_2Fc^{+/0}$ contact to the fundamental filament decay mode.

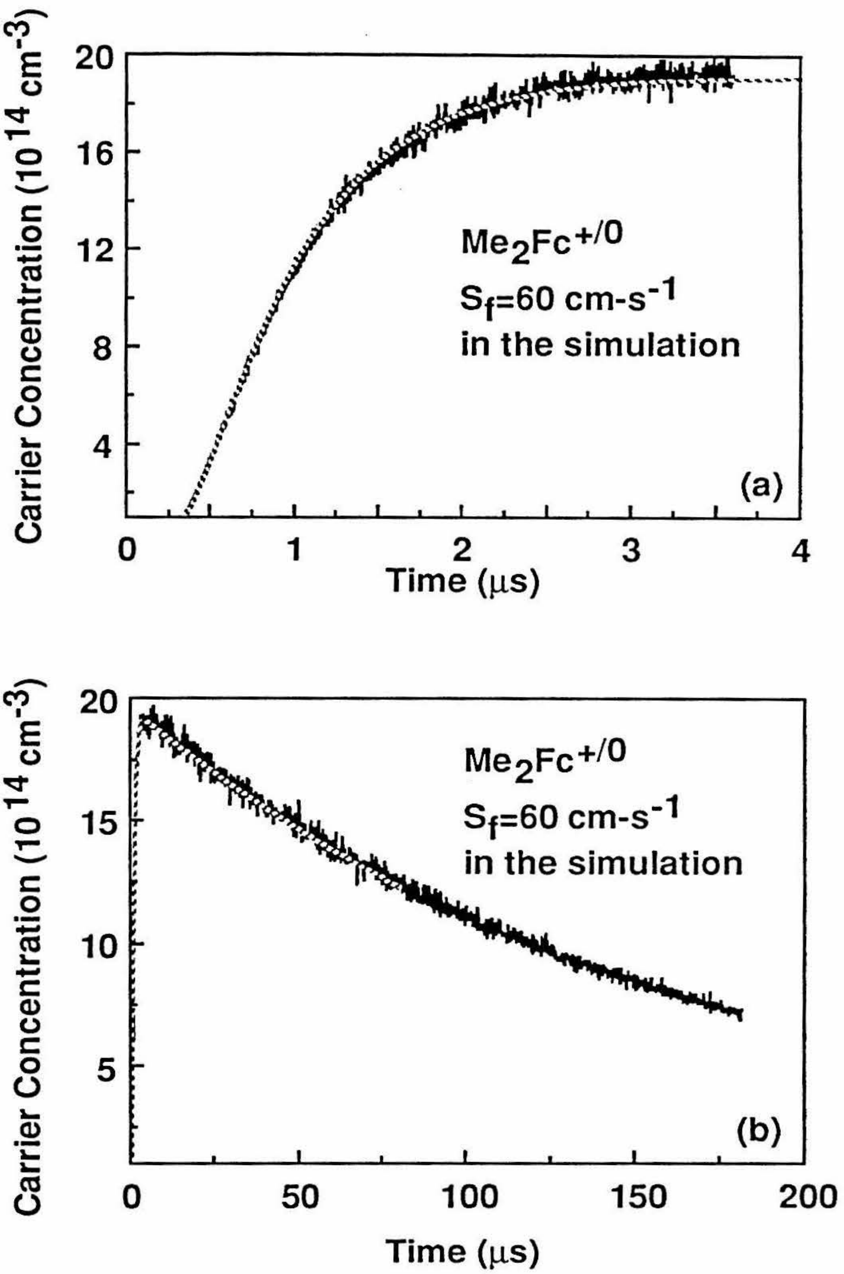

Figure 4. Digital simulation fits (dashed lines) to the carrier rise and decay data calculated from the V_{pn} measurements presented in Figs. 2a and b. The following parameters were used to generate the simulation results: intrinsic carrier concentration of 1.45×10^{10} cm^{-3}, dopant concentration of 3×10^{13} cm^{-3}, injection level of 2.1×10^{13} cm^{-2} (assuming a delta function laser pulse), photon penetration depth of 1.2 μm, ambipolar diffusion coefficient of 18 cm^2-s^{-1}, sample thickness of 107 μm, and the surface recombination velocity of 60 cm-s^{-1}.

Figure 5 illustrates the effect of varying S_f on the simulated time dependent carrier concentrations. For our sample thickness of $\approx$110 µm, the simulated transients were sensitive to changes in S_f for $500<S_f<5000$ cm-s^{-1}. However, at $S_f = 100$ cm-s^{-1}, the digital simulation and analytical solution (Eq. 11) using $S_f=0$ agreed to within the precision of the simulation (<5%) over the carrier concentration rise time (Fig. 5a). This agreement further justified the assumption, used in Eqs. 7-11, that diffusion occurred on a much faster time scale than front surface recombination at Si/CH_3OH-$Me_2Fc^{+/0}$ contacts. As the front surface recombination velocity was increased, the signal rise and decay at the back contacts become a combination of the diffusion and recombination processes. Figure 5b is the semi-log plot of the digitally simulated carrier concentration decays for S_f values of 100, 500, 1000 and 5000 cm-s^{-1}. The numbers indicated in the figure (in rectangular boxes) were the S_f values obtained from the slope of the linear fit to the concentration decays. When S_f was 100 cm-s^{-1}, the S_f value calculated using Eq. 6 differed by less than 2% from the actual S_f value used in the digital simulation. The deviation between the calculated S_f and the actual S_f used in the simulation increased to 10% for the S_f value of 1000 cm-s^{-1}, and was over 40% when the S_f value used in the simulation is 5000 cm-s^{-1}. These errors in the S_f values calculated using the analytical expression for carrier decay (Eqs. 5 and 6) indicate that, as the recombination rate exceeds 1000 cm-s^{-1}, the assumption that recombination occurs at a slower rate than diffusion becomes invalid.

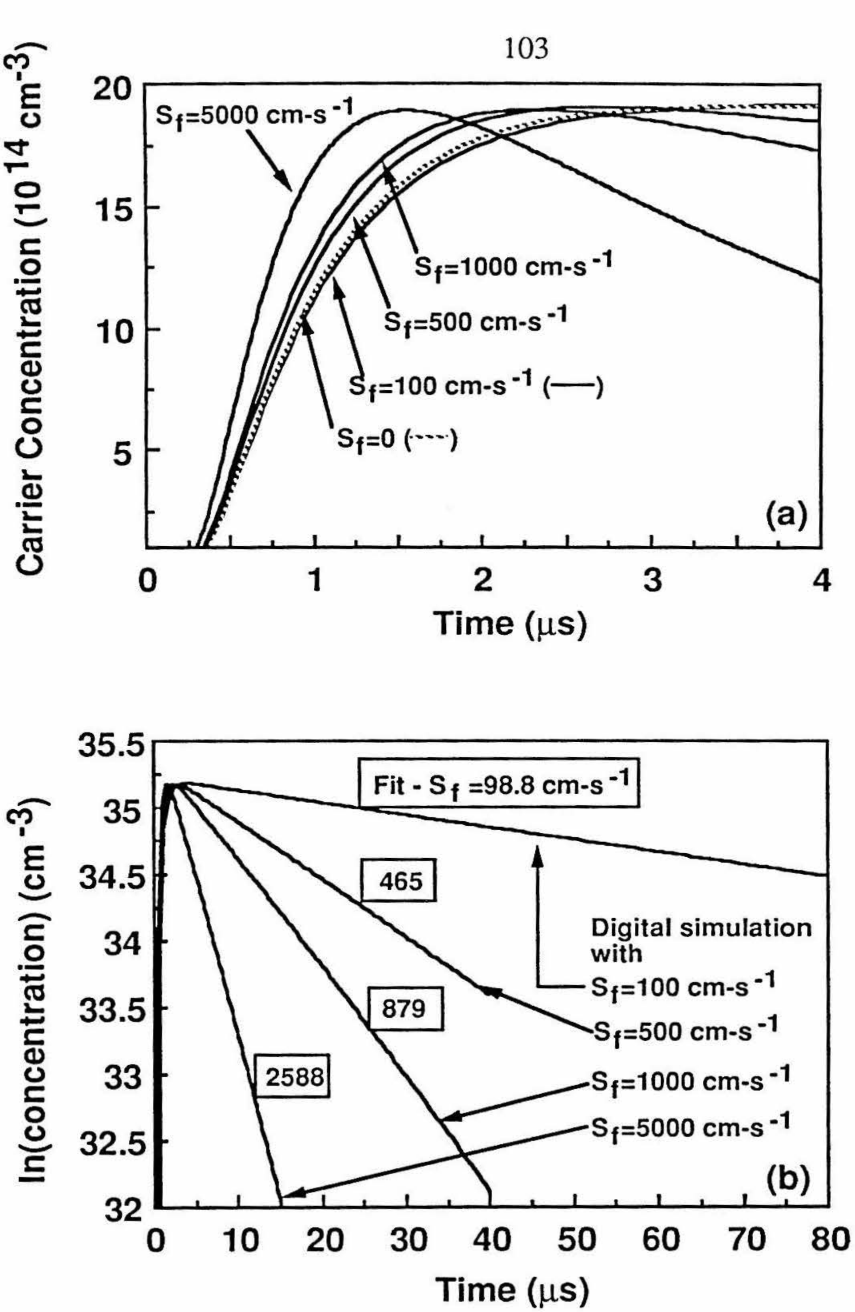

Figure 5. Digital simulation of the carrier concentration rise and decay at various surface recombination velocities. The injection level has been adjusted for various S_f values to the same maximum carrier concentration level: 2.15x10^{13} cm^{-2} for the S_f of 100 cm-s^{-1}, 2.47 cm^{-2} for the S_f of 500 cm-s^{-1}, 2.82 and 5.45 x10^{13} cm^{-2} for the S_f values of 1000 and 5000 cm-s^{-1} respectively. All other parameters used in the simulation were the same as the ones used in the simulation of Fig. 4. The dashed line in (a) was calculated from Eq. 11, by assuming zero surface recombination. The numbers presented in the rectangular boxes in (b) were S_f values calculated (using Eq. 6) from the slope of the linear fit to the decay portion of the corresponding curves.

Having validated the photovoltage modeling, carrier concentration profiles were then computed as a function of distance (x) at various times after the initial excitation pulse. Because S_f was determined from fits to the experimental data, there were no adjustable parameters in this aspect of the modeling. Figure 6 depicts the hole concentration profile after several time intervals following the initial excitation pulse, and Fig. 7 depicts the corresponding quasi-Fermi level position of holes ($\mathbf{E}_{f,p}$) relative to the intrinsic level ($\mathbf{E}_i$).[6]

$$\mathbf{E}_{f,p}(x,t) - \mathbf{E}_i = kT\ln[p(x,t)/n_i] \tag{12}$$

For the S_f value of 100 cm-s^{-1}, the difference between $\mathbf{E}_{f,p}(d,t)$ and $\mathbf{E}_{f,n}(0,t)$ at t=32 μs after excitation was less than 1 meV. Even at S_f value of 1000 cm-s^{-1}, $\mathbf{E}_{f,p}(d,t)$ - $\mathbf{E}_{f,p}(0,t)$ was less than 10 meV, *i.e.*, <1kT, 16 μs after the excitation. Thus, the experimentally measured values at the back of the sample yielded excellent approximations to the desired quasi-Fermi levels at the solid/liquid contact. Table I depicts the absolute errors between $\mathbf{E}_{f,p}(d,t)$ and $\mathbf{E}_{f,p}(0,t)$ obtained from the modeling at the given S_f values. These values can be used to correct the experimentally determined $\mathbf{E}_{f,p}(d)$ values to the desired $\mathbf{E}_{f,p}(0)$ values if a precision <1kT in determination of the surface quasi-Fermi level values is required. Under the high injection conditions, the electron concentration is the same as the hole concentration, so the gradient in $\mathbf{E}_{f,n}$ can also be corrected accordingly.

Table I. Digital simulation of the quasi-Fermi level differences between the back of the semiconductor sample and the semiconductor/liquid interface ($\mathbf{E}_{f,p}(d,t)$-$\mathbf{E}_{f,p}(0,t)$) at various S_f values.

	t=1.6 μs[a]	t=3.2 μs[a]	t=16 μs[a]	t=32 μs[a]
S_f=100 cm-s^{-1}	-8.0 meV[b]	<0.1 meV	0.8 meV	0.7 meV
S_f=500 cm-s^{-1}	-5.2 meV[b]	2.9 meV	3.6 meV	3.7 meV
S_f=1000 cm-s^{-1}	-1.8 meV[b]	6.3 meV	7.1 meV	7.6 meV
S_f=5000 cm-s^{-1}	19.4 meV	26.5 meV	33.5 meV	----

The values of the parameters used in the simulation were the same as those used in Fig. 5. (a) All data were obtained at the end of the time interval (t) during the simulation process. (b) The negative value implied that $\mathbf{E}_{f,p}(0,t)$ at the semiconductor/liquid interface was more positive than the hole quasi-Fermi level at the back surface, $\mathbf{E}_{f,p}(0,t)$>$\mathbf{E}_{f,p}(d,t)$.

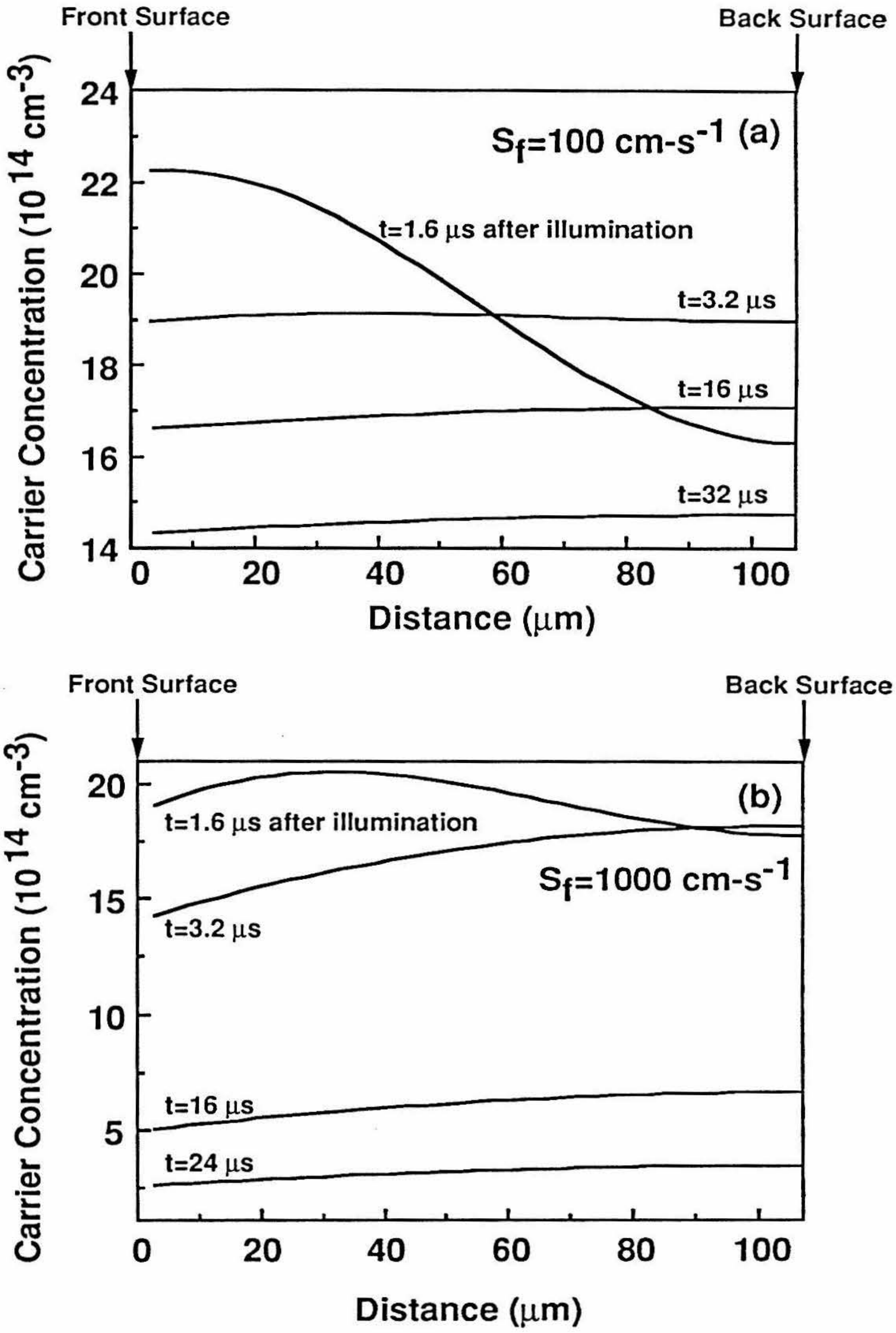

Figure 6. Digital simulation of the carrier concentration *vs.* distance after various time intervals following the illumination at the Si electrode, with a 532 nm pulsed laser. All parameters used in the simulation were the same as those used in Fig. 5.

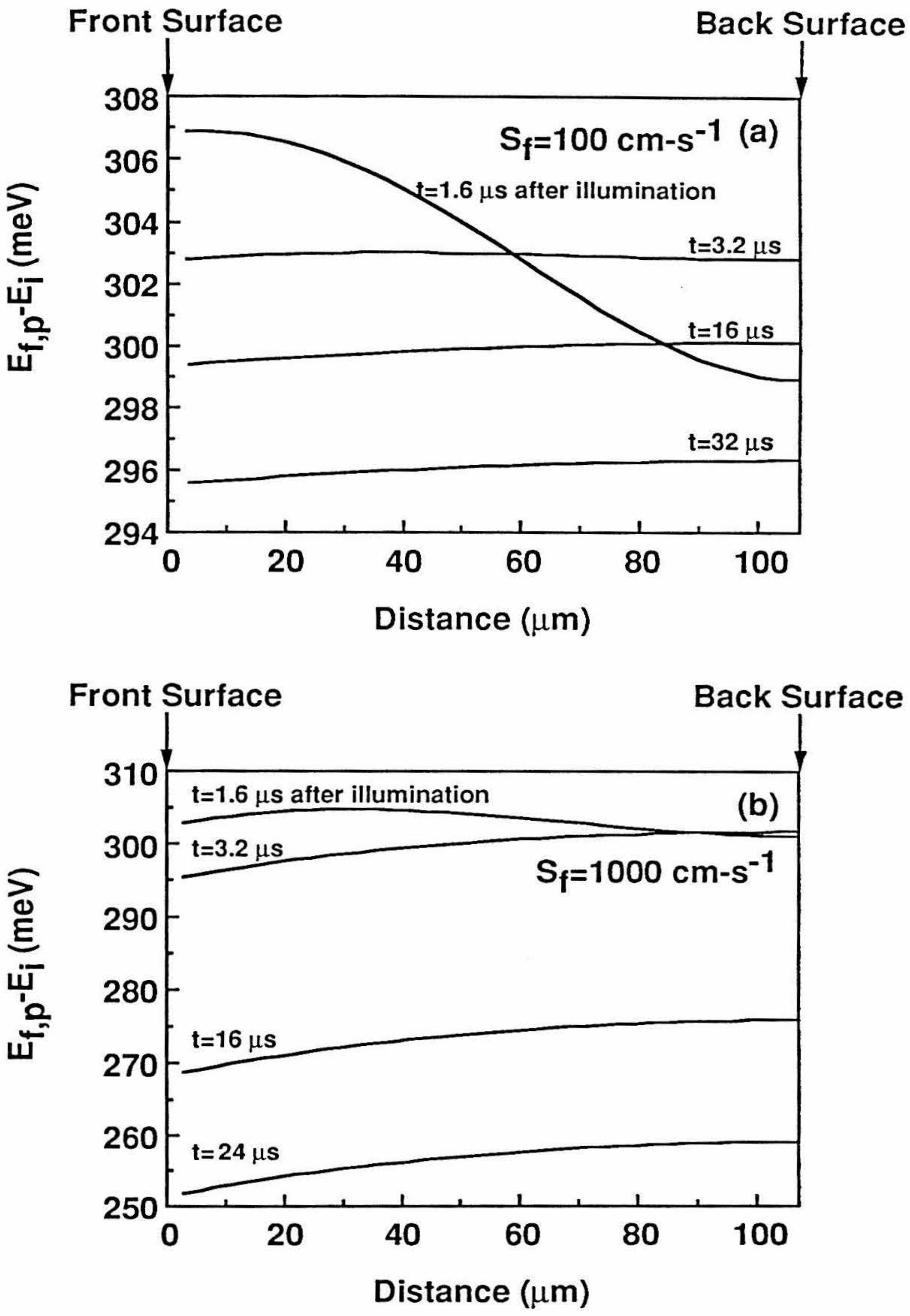

Figure 7. Digital simulation of the quasi-Fermi level distance profile after various time intervals following the illumination at the Si electrode with a 532 nm pulsed laser. All parameters used in the simulation were the same as those used in Fig. 5. The quasi-Fermi levels were calculated from the carrier concentrations of Fig. 6 using Eq. 12.

2. *Time-Resolved Photovoltage Measurements of Si/CH_3OH-THF-$Me_{10}Fc^{+/0}$, Si/CH_3OH-$MV^{2+/+\cdot}$, and Si/CH_3OH-$Co(Cp)_2^{+/0}$ Contacts:*

Transient photovoltage data were also collected for three other redox couples: $Me_{10}Fc^{+/0}$, $MV^{2+/+\cdot}$, and $Co(Cp)_2^{+/0}$. Such data are valuable for several reasons: a) they validated the transport model described above for other solid/liquid contacts; b) they allowed a quantitative evaluation of the surface recombination velocity for Si/CH_3OH junctions in the presence of various other redox couples, and c) they provided values for the gradients of the quasi-Fermi level to ensure that the values of $\mathbf{E}_{f,n}(d)$ and $\mathbf{E}_{f,p}(d)$ measured provided valid estimates of the desired $\mathbf{E}_{f,n}(0)$ and $\mathbf{E}_{f,p}(0)$ energies at the semiconductor/liquid interfaces.

The transient photovoltage decays (converted into carrier concentration decays) for Si/$Me_{10}Fc^{+/0}$ and Si/$MV^{2+/+\cdot}$ are shown in Figs. 8 and 9. The digital simulations of these data are also included in the figures. The value of S_f was 1000±300 cm-s^{-1} for the Si/$Me_{10}Fc^{+/0}$ junction at various light intensities, and was 800±200 in the $MV^{2+/+\cdot}$ solutions. These S_f values are in accord with the lower V_{oc} values observed in steady-state J-V measurements of Si/liquid contacts in these electrolytes (Part I), and larger inferred surface recombination velocities, as compared to the low S_f value (≈100 cm-s^{-1}) and high V_{oc} displayed by the Si/CH_3OH-$Me_2Fc^{+/0}$ system. They are also in accord with expectations based on the Shockley-Read-Hall recombination theory, as discussed further in section IV.

Even with these higher S_f values, measurement of $\mathbf{E}_{f,p}$ (or $\mathbf{E}_{f,n}$) at x=d (back surface) yielded little error in $\mathbf{E}_{f,p}(0)$ (or $\mathbf{E}_{f,n}(0)$) after very short time periods. Reference to Table I showed that for S_f=1000 cm-s^{-1}, the potential difference was only 7.6 mV across the semiconductor 32 μs after the illumination. These results suggested that the quasi-Fermi levels of carriers were essentially flat in the Si samples used in our experiments, and consequently, the quasi-Fermi levels measured at the back contacts were accurate descriptions of the quasi-Fermi positions at the semiconductor/liquid interfaces.

The only anomalous decay dynamics were those of Si/CH_3OH-$Co(Cp)_2^{+/0}$ contacts. The photovoltage decay data, converted into carrier concentrations (Fig. 10), consisted of two primary components. A best fit yielded S_f=750 cm-s^{-1} for t<10 μs, and S_f=275 cm-s^{-1} for t>20 μs. The origin of the fast component in the decays remains unclear at this time. The slower surface recombination rate observed at longer times is consistent with the overall high V_{oc} values exhibited by these contacts (Part I).

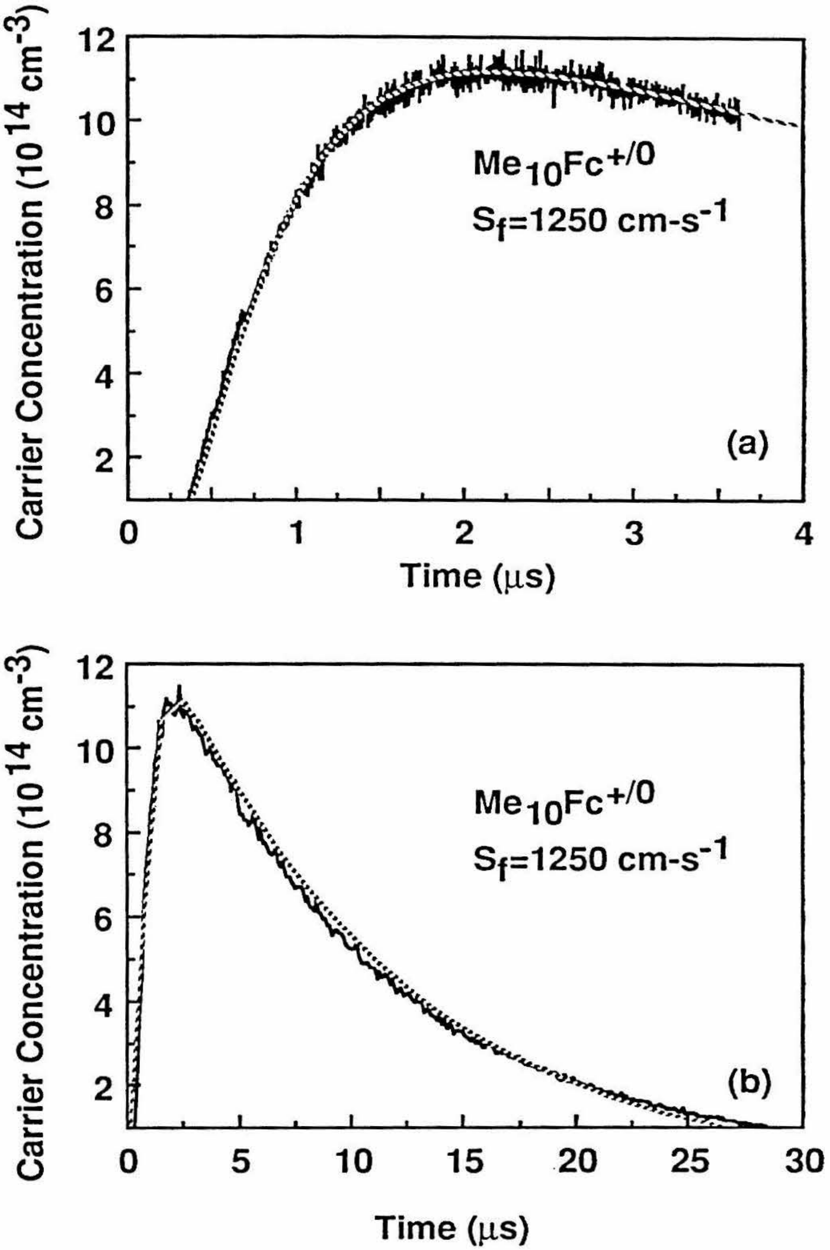

Figure 8. Measurements (solid lines) and simulation fits (dashed lines) of the carrier concentration rise and decay (calculated from V_{pn}) at a Si/20% CH_3OH-80% THF (by volume)-23 mM $Me_{10}Fc$-14 mM $Me_{10}FcBF_4$-0.55 M $LiClO_4$ junction under 532 nm pulsed laser illumination ($\approx 3\times10^{-5}$ J). The injection level used in the simulation was 1.76×10^{13} cm^{-2}, and the value of the surface recombination velocity was 1250 cm-s^{-1}. All other parameters were the same as those in Fig. 4.

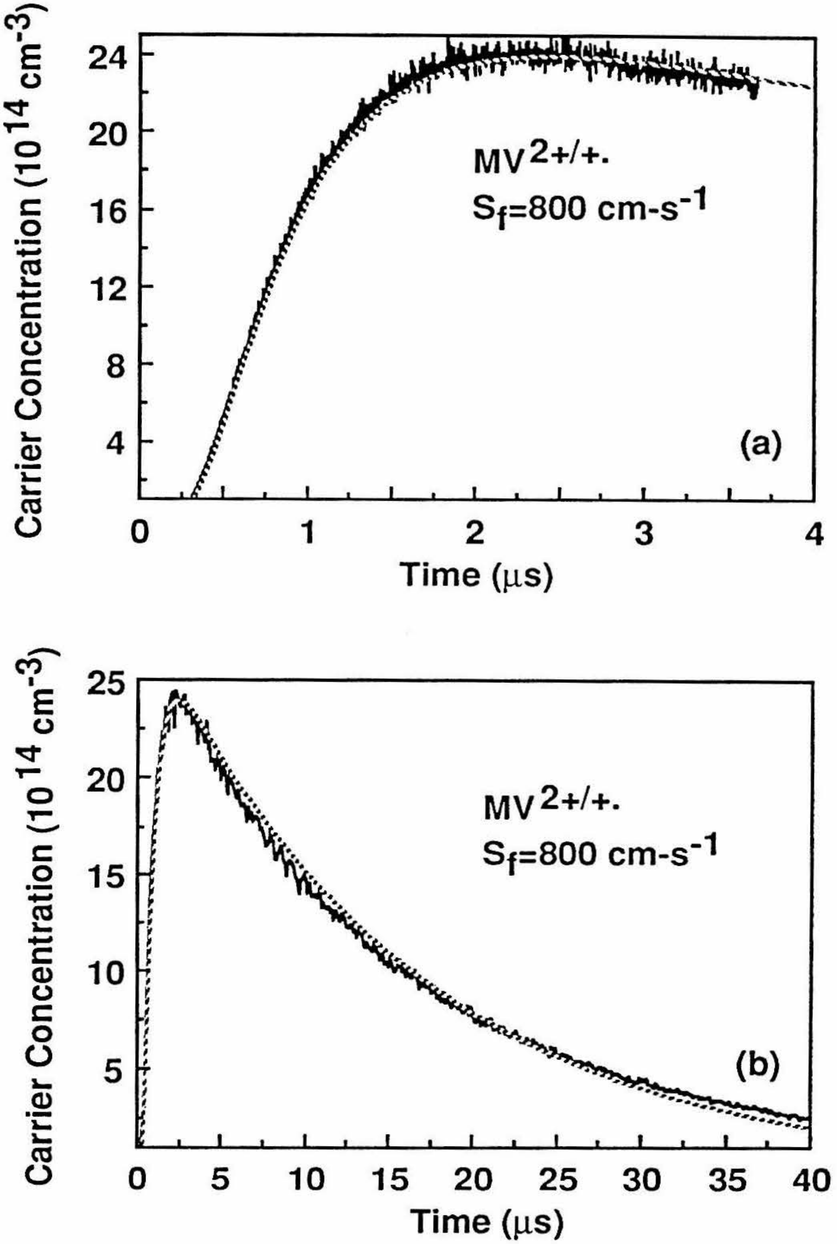

Figure 9. Measurements (solid lines) and simulation fits (dashed lines) of the carrier concentration rise and decay (calculated from V_{pn}) at a Si/CH_3OH-16 mM $MV^{+\cdot}$-23 mM $MVCl_2$-1.1 M LiCl junction under 532 nm pulsed laser illumination ($\approx 7 \times 10^{-4}$ J). The injection level used in the simulation was 3.38×10^{13} cm^{-2}, and the value of the surface recombination velocity was 800 cm-s^{-1}. All other parameters were the same as those in Fig. 4.

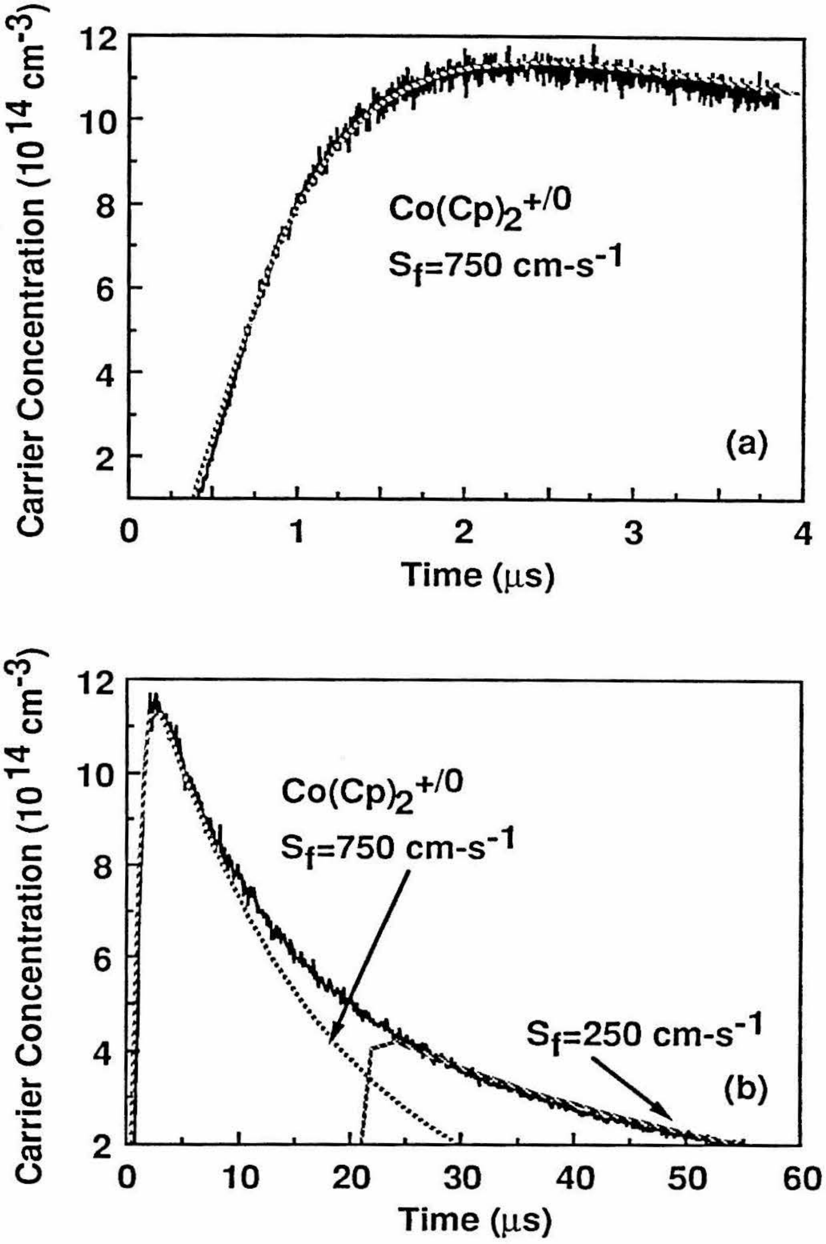

Figure 10. Measurements (solid lines) and simulation fits (dashed lines) of the carrier concentration rise and decay (calculated from V_{pn}) at a Si/CH_3OH-8.5 mM $Co(Cp)_2$-38 mM $Co(Cp)_2Cl$-1.0 M LiCl junction under 532 nm pulsed laser illumination. The injection level used in the simulation was 1.56×10^{13} cm^{-2}, and the value of the surface recombination velocity was 750 cm-s^{-1}. In (b), the slower decay component at longer time was also fitted with the digital simulation, using S_f value of 250 cm-s^{-1}.

3. Modeling of the Steady-State Carrier Concentration vs. Distance Profiles for Si/CH_3OH Liquid Contacts:

It was also of interest to analyze the steady-state photovoltage data for the various Si/CH_3OH contacts. A validated treatment of the transport dynamics in the steady-state situation would allow evaluation of the quasi-Fermi level gradients without reference to any of the transient data described above. A critical test of the entire model would therefore be provided by the agreement (or lack thereof) between these two independent methods for determining S_f and $E_{f,p}(d,t)-E_{f,p}(0,t)$.

At steady-state, the carrier concentrations n(x,t) and p(x,t) are given by the standard relationship between transport by diffusion, recombination and generation:[21]

$$D\frac{d^2p(x)}{dx^2}-\frac{p(x)}{\tau_b}+I_o\alpha\exp(-\alpha x)=0 \tag{13}$$

where p(x) is the hole concentration at distance x, τ_b is the bulk carrier lifetime at x, I_o is the flux of photons absorbed at the semiconductor front surface (photons-$cm^{-2}s^{-1}$) and α is the absorption coefficient (cm^{-1}) of Si at a particular wavelength of illumination. Again, under high injection conditions, n(x)=p(x) and equations analogous to Eqs. 13-19 can be used to calculate the electron concentration.

Because the V_{pn} (i.e., $V_{oc,p+}$-$V_{oc,n+}$) values for identical Si samples, that contained highly passivated front contacts to minimize the surface recombination process in air, were larger than any of the $V_{oc,p+}$-$V_{oc,n+}$ values observed for the Si/CH_3OH contacts studied herein, recombination at the semiconductor/liquid junction could be identified as the dominant carrier recombination process. Therefore, the back surface recombination velocity was neglected. With the front surface recombination velocity as S_f, the following boundary conditions existed:

$$\left.\frac{dp(x)}{dx}\right|_{x=d}=0 \tag{14}$$

$$\left.\frac{dp(x)}{dx}\right|_{x=0}=\frac{S_f}{D}p(0) \tag{15}$$

Equation 13 can be simplified by assuming that the bulk recombination rate, τ_b, was independent of distance (the high purity Si sample had τ_b>1 ms). Therefore,

$$p(x)=C_0\exp(-\alpha x)+C_1\exp\left(\frac{x}{L}\right)+C_2\exp\left(-\frac{x}{L}\right) \tag{16}$$

$$C_0 = \frac{I_o \alpha}{1/\tau_b - D\alpha^2} \tag{17}$$

$$C_1 = \frac{\alpha \exp(-\alpha d) - \frac{\alpha + S_f/D}{1/L + S_f/D} \times \frac{\exp(-d/L)}{L}}{\frac{\exp(d/L)}{L} - \frac{\exp(-d/L)}{L} \times \frac{1/L - S_f/D}{1/L + S_f/D}} \times C_0 \tag{18}$$

$$C_2 = \frac{1/L - S_f/D}{1/L + S_f/D} \times C_1 - \frac{\alpha + S_f/D}{1/L + S_f/D} \times C_0 \tag{19}$$

where L is the diffusion length of the carriers, $L=(D\tau_b)^{1/2}$.

The value of p(d) could be calculated from V_{pn} using Eq. 4 measured under the steady-state, high injection conditions. Since I_o, D, d, α were known, using a bulk lifetime τ_b of 1 ms,[13] Eq. 16-20 could be solved for the unique value of S_f that was required to produce the measured values of V_{pn}. This modeling thus directly yielded values for the carrier concentration profiles as a function of distance throughout the sample. From Eq. 12, the distance profile of the hole quasi-Fermi level, $\mathbf{E}_{f,p}(x)$, could be calculated. This calculation provided a quantitative value for the difference between the quasi-Fermi level positions at the back and front of the sample for each carrier type.

Table II displays the values of S_f that were obtained from this steady-state, high injection modeling procedure. As expected, contacts with the largest V_{oc} values produced the smallest surface recombination velocities. The S_f values were, in general, in excellent agreement with the values determined from the transient photovoltage decay measurements (vide supra), lending further support to the hypothesis that charge carrier motion was predominantly driven by diffusion in these high injection samples.

For Si/CH_3OH-$Me_2Fc^{+/0}$ and Si/CH_3OH-$CoCp_2^{+/0}$ contacts, which displayed the highest V_{pn} values, and therefore had the lowest surface recombination velocities, the maximum error in $\mathbf{E}_{f,p}(d)$ - $\mathbf{E}_{f,p}(0)$ (and in $\mathbf{E}_{f,n}(d)$ - $\mathbf{E}_{f,n}(0)$) was <2 meV for a photon penetration depth of 100 μm, *i.e.*, <<1kT. This small gradient in the quasi-Fermi level was a consequence of the relatively thin samples, combined with the high carrier diffusion coefficient, long bulk carrier lifetime (>1 ms), and small surface recombination velocities (<200 $cm\text{-}s^{-1}$) that are characteristic of Si/$Me_2Fc^{+/0}$ and Si/$Co(Cp)_2^{+/0}$ contacts. For Si/$MV^{2+/+}$ and Si/$Me_{10}Fc^{+/0}$ contacts, S_f was somewhat larger. However, even for these contacts the maximum difference in the quasi-Fermi level positions between the back and front of the sample was 5 meV. This simulation showed that the measured values were close approximations of the values at the front surface, and also provided analytical means for precisely correcting the experimentally determined values to obtain **$E_{f,p}$**(0,t) and **$E_{f,n}$**(0,t) for all the systems of interest (Table II).

Table II. Steady-state calculation of the front surface recombination rate, S_f, in solutions with various redox couples.

	$Me_2Fc^{+/0}$[a]	$Me_{10}Fc^{+/0}$[b]	$MV^{2+/+\cdot}$[c]	$Co(Cp)_2^{+/0}$[d]
V_{pn}-mV (J_{ph}-mA-cm^{-2})[e]	517 (3.15)	419 (3.99)	391 (2.30)	485 (3.39)
S_f (cm-s^{-1})[f]	50	800	900	120
$E_{f,p}$(d)-$E_{f,p}$(0) (eV)[g]	-0.1	<0.1	<0.1	-0.1
$E_{f,p}$(d)-$E_{f,p}$(0) (eV)[h]	0.3	4.5	4.9	0.7

(a) Obtained in a 11 mM Me_2Fc-16 mM Me_2FcBF_4-1.0M $LiClO_4$-CH_3OH solution. (b) In a 23 mM $Me_{10}Fc$-14 mM $Me_{10}FcBF_4$-0.5M $LiClO_4$-20% CH_3OH-80% THF (by volume) solution. (c) In a 17 mM $MV^{+\cdot}$-23 mM $MVCl_2$-1.1M LiCl-CH_3OH solution. (d) In a 45 mM $Co(Cp)_2$-2 mM $Co(Cp)_2^+$-0.9 M LiCl-CH_3OH solution. (e) The differences in open-circuit potentials measured at the p^+ and n^+ contact points, $V_{pn}=V_{oc,p^+}-V_{oc,n^+}$, at the short-circuit current levels reported in the parentheses. (f) The surface recombination velocity calculated using Eqs. 16-19. The number of photons absorbed by the semiconductor, I_o, was obtained from the J_{ph} values provided assuming 100% internal carrier collection efficiency at short-circuit, $I_o=J_{ph}/(q(1-\exp(-\alpha d)$, where d is the thickness of the sample, d=107 μm in this simulation. (g) The difference in the quasi-Fermi level of holes between the back surface and the front surface at a photon penetration depth of 1 μm ($\alpha=1\times10^4$ cm^{-1}). (h) Same as g but at a photon penetration depth of 100 μm ($\alpha=1\times10^2$ cm^{-1}).

This steady-state carrier modeling was also useful in predicting the behavior of V_{pn} as a function of the illumination wavelength. Figure 11 shows the carrier concentration profiles and quasi-Fermi level positions that were calculated for high and low energy monochromatic illuminations (1 μm and 100 μm penetration depths). Under fixed S_f and illumination levels, $E_{f,p}$(d) is not a strong function of wavelength. The largest difference in **$E_{f,p}$**(d) between using a penetration depth of 1 μm and 100 μm is less than 6 meV (S_f=1000 cm-s^{-1}).

This prediction was verified experimentally for Si/$Me_2Fc^{+/0}$ and Si/$Me_{10}Fc^{+/0}$ contacts, for which V_{pn} was measured as a function of wavelength at a constant carrier injection level (Table III). The values for V_{pn} were independent of wavelength within the error of the measurements (± 4 mV). Thus, because the values of **$E_{f,n}$** and **$E_{f,p}$** were not strong functions of wavelength, **$E_{f,n}$** and **$E_{f,p}$** values determined under polychromatic illumination were representative of the quasi-Fermi level positions for this specific injection level at the various Si/CH_3OH-redox couple interfaces.

Table III. V_{pn} values as a function of wavelengths for Si in contact with a 58 mM Me_2Fc-2 mM Me_2FcBF_4-1.0 M $LiClO_4$-CH_3OH solution or a 24 mM $Me_{10}Fc$-17 mM $Me_{10}FcBF_4$-0.54M $LiClO_4$-20% CH_3OH-80% THF (by volume) solution.

	457 nm	514 nm	760 nm	820 nm	880 nm	940 nm	980 nm	1020 nm
$Me_{10}Fc^{+/0a}$	336	----	337	338	----	336	333	----
$Me_{10}Fc^{+/0b}$	----	374	----	----	377	376	373	376
$Me_2Fc^{+/0c}$	539	537	----	----	540	----	536	540

(a) Measured at J_{sc}=0.21 mA-cm^{-2}. (b) Measured at J_{sc}=0.81 mA-cm^{-2}. (c) Measured at J_{sc}=1.7 mA-cm^{-2}.

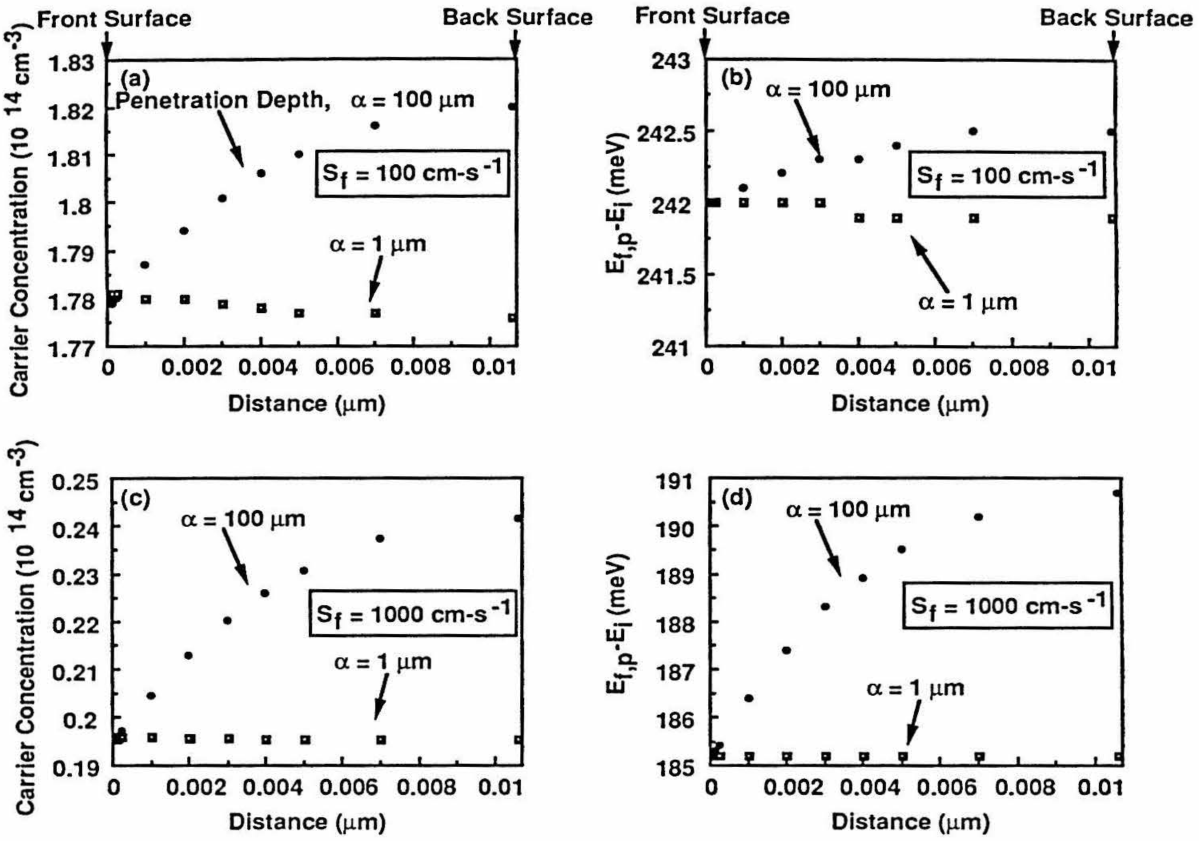

Figure 11. Steady-state carrier concentration and quasi-Fermi level profiles under illumination with photon penetration depths of 1 μm and 100 μm.

IV. DISCUSSION

The results presented above clearly indicate that a diffusional model of charge carrier separation and movement satisfactorily describes the real-time and steady-state photovoltage properties of Si/CH_3OH contacts under high injection conditions. This behavior fully supports the analysis of the steady-state J-V properties presented in Part I, and validates the approximation that the quasi-Fermi levels determined at the back of these samples were good approximations to the values near the solid/liquid contact.

In this work, photovoltage rise and decay data were exploited to investigate the charge carrier dynamics. For conventional photoelectrodes under low level injection conditions, the photovoltage exhibits an extremely rapid rise time which is usually limited by the bandwidth of the measuring instrumentation. This limitation occurs because the photovoltage under low level injection is produced predominantly by charge separation across the depletion region, driven by drift, which occurs in <1 ps.[7,8] In the absence of a significant interfacial electric field to separate charge, however, diffusion processes are required for effective charge movement. This mode of transport should result in a relatively slow rise time of the photovoltage, with a functional form predictable by standard diffusional models. The time scales of the measurements of the transient photovoltage rise, as well as the functional form of these signals, clearly indicated the validity of these postulates for the studies discussed above.

The experimental and theoretical description of this photoelectrode system has also allowed rigorous estimation of the gradient in quasi-Fermi levels from the back to the front of the sample. In most cases, errors of <<kT, and as small as <1 meV, resulted from the use of values at the back of the sample. Note that by assuming all of the recombination occurred at the front surface of the sample, these gradients are *larger* than ones that would be computed assuming that some of the carrier recombination proceeded in the bulk of the sample and/or at the back contacts. This assumption of front surface-dominated recombination was justified in all but possibly one case. For Si/ $Me_2Fc^{+/0}$ contacts, the measured S_f value (100±40 cm-s^{-1}) was very similar to the S_f value (50±10 cm-s^{-1}) measured on the sample in air, with the front surface of the sample passivated to minimize front surface recombination. Thus, a rigorous correction can be made for the quasi-Fermi level gradients in all systems studied except for the $Me_2Fc^{+/0}$ contact. In the Si/CH_3OH-$Me_2Fc^{+/0}$ system, where S_f is so small that recombination at the back contact may contribute to the total observed recombination dynamics, a rigorous estimate of the quasi-Fermi level gradients indicates that these gradients are less than 1 meV (Tables I and II).

They may possibly be smaller than this limiting value, depending on the precise value of S_f at the back surface of the sample.

The data and modeling also have yielded values for the recombination rates at the semiconductor/liquid contact as a function of the redox couple electrochemical potential, $E(A/A^-)$. The values of S_f are smaller in solutions with $E(A/A^-)$ near the conduction band edge, E_{cb}, or the valence band edge, E_{vb}, of the semiconductor, than those with $E(A/A^-)$ in the middle of the band gap. These recombination data are in agreement with the predictions of the Shockley-Read-Hall model for recombination, which suggests that recombination is more favored when the trap energy is near the middle of the semiconductor band gap.[12]

According to the model, both electrons and holes are required to undergo recombination under high injection conditions, so the measured S_f value represents the slower of the two carrier capture dynamics:[12]

$$S_f = \left(\frac{1}{k_n} + \frac{1}{k_p}\right)^{-1} \tag{20}$$

where k_n is the electron capture velocity in cm-s^{-1} and k_p is the hole capture velocity. If electrons and holes recombine through oxidation and reduction reactions with the solution redox couples, k_n and k_p could be related to the electron and hole reaction rate constants at a semiconductor (k_{et} and k_{ht} respectively) by: $k_n = k_{et}[A]$, and $k_p = k_{ht}[A^-]$, where $[A]$ and $[A^-]$ are the concentration of electron acceptors and donors in the solution respectively. According to the Marcus/Gerischer model for charge transfer, the value of k_{et} is related to the activation energies for electron transfer from the conduction band by:[22,23]

$$k_{et} \propto \exp\left[-(\lambda + \mathbf{E}_{cb} - \mathbf{E}^{o'}(A/A^-))^2/(4kT\lambda)\right] \tag{21}$$

where λ is the reorganization energy, and $E^{o'}(A/A^-)$ is the formal electrochemical potential of the solution. Similarly, k_{ht} is related to the activation energy for hole transfer from the valence band by:

$$k_{ht} \propto \exp\left[-(\lambda + \mathbf{E}^{o'}(A/A^-) - \mathbf{E}_{vb})^2/(4kT\lambda)\right] \tag{x}$$

Although all of the self-exchange rate constants are similar for the donors/acceptors used in this work, indicating the reorganization energies, λ, are also similar for the redox couples used,[24] the Marcus/Gerischer model does predict a different functional form for the energy-dependence of k_{et} and k_{ht} on the solution energy, $E^{o'}(A/A^-)$. As the solution potential approaches the conduction band, the activation energy for electron transfer (E_{cb}-$E^{o'}(A/A^-)$) is small, and the electron reaction is slow; the activation energy for the hole transfer process ($\mathbf{E}^{o'}(A/A^-)$-$\mathbf{E}_{vb}$) is large, and the hole reaction is fast. Therefore, the surface recombination term is limited by the small electron reaction rate, k_{et}. Similarly, as the solution potential approaches the valence band, the hole transfer rate, k_{ht}, is small, and the electron transfer rate k_{et} is large. The surface recombination rate is limited by the slow electron reaction with the solution. According to this model, recombination is favored for both the electrons and holes when the solution potential is near the middle of the semiconductor band gap. Our experimental observations confirm this prediction.

Another striking feature of the photovoltage decay analysis is the relatively small surface recombination velocities that have been obtained for all the redox couples investigated in this study. These relatively low values have been obtained even though significant concentrations of both forms of the redox reagent were present in solution, and could therefore act simultaneously as electron and hole trapping sites. These low surface recombination velocities underscore the rather slow interfacial charge transfer dynamics of photogenerated charge carriers with these outer-sphere redox couples, regardless of the energetic for charge carrier capture. Such low surface recombination rates are essential for high photoelectrochemical efficiencies under high injection conditions, because otherwise the photogenerated carriers would be consumed nonproductively through recombination at the solid/liquid interface and would not lead to current flow through the external circuit. These low S_f values also are essential in preventing significant gradients of the quasi-Fermi levels in the sample (Fig. 6 and Table I), so that measurements at the back of the specimen yield the desired information on the carrier concentrations at the solid/liquid contact. Our data indicate that low S_f behavior appears to be a general property of the Si/CH_3OH interface with outer sphere redox couples, and is not specifically confined to the Si/CH_3OH-$Me_2Fc^{+/0}$ system, for which low charge transfer velocities were previously documented. The maximum surface recombination velocity obtained in our solutions is less than 1500 cm-s^{-1}, which provides the upper limit estimate of a charge transfer rate of 10^{-16} cm^4-s^{-1} (assuming a 10 mM electron donor or acceptor concentration). This value agrees with the theoretical predictions for charge transfer at semiconductor/liquid junctions.[23]

V. Conclusion:

We have demonstrated that quasi-Fermi levels of carriers can be measured directly at our semiconductor sample. The quasi-Fermi level profiles as a function of the distance into the semiconductor have been examined in detail. Analysis of the real-time photovoltage rise and decay measurements using analytical models and digital simulation confirms that, under high injection conditions, carrier movements in the semiconductor are driven by diffusion, and the quasi-Fermi levels of electrons and holes remain essentially flat across the semiconductor. Results from the steady-state modeling agree with transient measurements. The surface recombination velocities in various solutions have been calculated from the transient and steady-state measurements. The fastest recombination rate is less than 1500 cm-s^{-1}, and agrees with the predictions of the semiconductor/liquid junction charge transfer theories. The recombination rates are higher for solutions with redox potentials near the middle of the semiconductor band gap than those with potentials close to the conduction or valence band edge. This result fully agrees with the Shockley-Read-Hall theory on recombination.

References:

(1) Gerischer, H. In *Physical Chemistry: An Advanced Treatise*; H. Eyring; D. Henderson and W. Yost, Ed.; Academic: New York, 1970; Vol. 9A; pp 463.

(2) Fonash, S. J. *Solar Cell Device Physics*; Academic: New York, 1981.

(3) Meissner, D.; Memming, R. *Electrochimica Acta* **1992**, *37*, 779.

(4) Reineke, R.; Memming, R. *J. Phys. Chem.* **1992**, *96*, 1317.

(5) Laibinis, P. E.; Stanton, C. E.; Lewis, N. S. *J. Phys. Chem.* **1994**, *in press*.

(6) Sze, S. M. *The Physics of Semiconductor Devices;* 2nd ed.; Wiley: New York, 1981.

(7) Willig, F. *Ber. Bunsenges. Phys. Chem.* **1988**, *92*, 1312.

(8) Willig, F.; Bitterling, K.; Charlé, K.-P.; Decker, F. *Ber. Bunsenges. Phys. Chem.* **1984**, *88*, 374.

(9) Ryba, G. N. Ph.D. Thesis, California Institute of Technology, 1992.

(10) Neudeck, G. W.; Pierret, R. *The PN Junction Diode;* II ed.; Addison-Wesley Publishing Company: Reading, 1989; Vol. II.

(11) Shockley, W. *Electrons and Holes in Semiconductors*; D. Van Norstrand Company: New York, 1950, pp 320.

(12) Many, A.; Goldstein, Y.; Grover, N. B. *Semiconductor Surfaces*; North-Holland Publishing Co.: New York, 1965, pp 262.

(13) Swanson, R. M. *Solar Cells* **1986**, *17*, 85.

(14) Forbes, M. D. E.; Lewis, N. S. *J. Am. Chem. Soc.* **1990**, *112*, 3682.

(15) Carrier-carrier scattering increases as a function of carrier concentration and reduces the mobility and therefore the diffusion coefficients of electrons and holes. In our simulation, such variations could be neglected to within 5% for carrier concentrations between 5×10^{13} and 10^{16} cm^{-3}.

(16) Thurber, W. R.; Mattis, R. L.; Liu, Y. M.; Filliben, J. J. *J. Electrochem. Soc.* **1980**, *127*, 2291.

(17) Thurber, W. R.; Mattis, R. L.; Liu, Y. M.; Filliben, J. J. *J. Electrochem. Soc.* **1980**, *127*, 1807.

(18) Carslaw, H. S.; Jaeger, J. C. *Conduction of Heat in Solids;* 2nd ed.; Oxford University Press: London, 1959, pp 101.

(19) The symbol x' represents the distance term used in the integration between 0 to d.

(20) *Optical Functions of Intrinsic Si*; Aspnes, D. E., Ed.; INSPEC: London, 1988.

(21) Blakemore, J. S. *Semiconductor Statistics*; Dover Publications, Inc.: New York, 1987.

(22) Morrison, S. R. *Electrochemistry at Semiconductor and Oxidized Metal Electrodes*; Plenum: New York, 1980.

(23) Lewis, N. S. *Ann. Rev. Phys. Chem.* **1991**, *42*, 543.

(24) McManis, G. E.; Nielson, R. M.; Gochev, A.; Weaver, M. J. *J. Am. Chem. Soc.* **1989**, *111*, 5533.